SRI International

Final Technical Report • August 2003

OVERLOAD EFFECTS ON FATIGUE FRACTURE SURFACES

Prepared by:

Dr. Takao Kobayashi, Senior Staff Scientist
Dr. Jeffrey W. Simons, Sr. Computational Engineer
Dr. Donald A. Shockey, Director
Center for Fracture Physics
Materials Research Laboratory
Physical Sciences Division

Prepared for:

USAF/AFMC
Air Force Research Laboratory
2310 8th Street, Building 167
Wright-Patterson AFB, OH 45433-7801

Attention: Dr. Jay Jira

Contract No. MDA972-01-C-0044
SRI Project No. P11305

Approved:

Angel Sanjurjo, Director
Materials Research Laboratory

20030910 101

333 Ravenswood Avenue • Menlo Park, CA. 94025-3493 • 650.859.2000

REPORT DOCUMENTATION PAGE

Form Approved
OMB NO. 0704-0188

Public Reporting burden for this collection of information is estimated to average 1 hour per response, including the time for reviewing instructions, searching existing data sources, gathering and maintaining the data needed, and completing and reviewing the collection of information. Send comment regarding this burden estimates or any other aspect of this collection of information, including suggestions for reducing this burden, to Washington Headquarters Services, Directorate for information Operations and Reports, 1215 Jefferson Davis Highway, Suite 1204, Arlington, VA 22202-4302, and to the Office of Management and Budget, Paperwork Reduction Project (0704-0188,) Washington, DC 20503.

1. AGENCY USE ONLY (Leave Blank)

2. REPORT DATE

3. REPORT TYPE AND DATES COVERED
Final Technical Report November 30, 2002

4. TITLE AND SUBTITLE
OVERLOAD EFFECTS ON FATIGUE FRACTURE SURFACES

5. FUNDING NUMBERS
MDA972-01-C-0044

6. AUTHOR(S)
Takao Kobayashi, Jeffrey W. Simons, and Donald A. Shockey

7. PERFORMING ORGANIZATION NAME(S) AND ADDRESS(ES)
SRI International
333 Ravenswood Avenue
Menlo Park, CA 94025

8. PERFORMING ORGANIZATION REPORT NUMBER
P11305

9. SPONSORING / MONITORING AGENCY NAME(S) AND ADDRESS(ES)
Dr. Jay Jira
USAF/AFMC
Air Force Research Laboratory
2310 8th Street, Building 167
Wright-Patterson AFB, OH 45433-7801

10. SPONSORING / MONITORING AGENCY REPORT NUMBER

11. SUPPLEMENTARY NOTES
The views, opinions and/or findings contained in this report are those of the author(s) and should not be construed as an official Department of the Army position, policy or decision, unless so designated by other documentation.

12 a. DISTRIBUTION / AVAILABILITY STATEMENT
Approved for public release; distribution unlimited.

12 b. DISTRIBUTION CODE

1. ABSTRACT (Maximum 200 words)

The effects of overloads on fatigue fracture surfaces of titanium and nickel alloys were investigated with advanced fractographic techniques. Fracture surface topographies were mapped quantitatively by confocal microscopy and analyzed by comparing conjugate topographs (the FRASTA technique) to measure the deformation at locations of overload. Insight into plastic zone development was obtained from computational simulations of fatigue tests with the LSDYNA3D code.

FRASTA detected the remnants of plastic blunting on Ti alloy fracture surfaces (even though the deformation was not perceptible with an SEM) and indicated the bluntness as the amount of deviation from a FRASTA-generated fracture progression curve. Under certain conditions of stress ratio, the deviation related to the magnitude of the overload. Results for other stress ratios and IN100 nickel alloy tested at 650°C were less clear. Nevertheless, a procedure for detecting the occurrence of overloads from failed parts has been demonstrated. Moreover, if these initial findings can be confirmed, expanded, and related to cyclic load spectra, then fatigue retardation models, and hence, lifetime prediction capability can be improved.

2. SUBJECT TERMS
Fatigue Crack Growth, Overload, IN100, Titanium Alloy, Fractography, FRASTA, Retardation

15. NUMBER OF PAGES

16. PRICE CODE

17. SECURITY CLASSIFICATION OF REPORT	18. SECURITY CLASSIFICATION ON THIS PAGE	19. SECURITY CLASSIFICATION OF ABSTRACT	20. LIMITATION OF ABSTRACT
UNCLASSIFIED	*UNCLASSIFIED*	*UNCLASSIFIED*	*UL*

NSN 7540-01-280-5500

Standard Form 298 (Rev.2-89)
Prescribed by ANSI Std. 239-18
298-102

TABLE OF CONTENTS

REPORT DOCUMENTATION PAGE i
TABLE OF CONTENTS ii
LIST OF FIGURES iv
LIST OF TABLES x
EXECUTIVE SUMMARY xi
1. INTRODUCTION 1
2. OBJECTIVES AND APPROACH 3
   2.1 Fatigue Fracture Surface Generation, Characterization and Analysis 3
3. RESULTS FOR TITANIUM ALLOIY Ti-6 Al-2SN-4Zr-6MO 7
   3.1 Stress ratio, R = 0.05 7
   3.2 Stress ratio, R = 0.50 8
   3.3 Summary of findings for titanium alloy 10
4. RESULTS FOR IN1 – NICKEL-BASE ALLOYS 11
   4.1 Stress ratio, R = 0.05 and 20 Hz 11
   4.2 Stress ratio, R = 0.05 and 0.1667 12
   4.3 Stress ratio, R = 0.50 and 20 Hz 13
   4.4 Stress ratio, R = 0.50 and 0.1667 Hz 14
   4.5 Maximum deviation vs K_{max} for all load conditions 15
   4.6 Assessment of overload magnitude from the deviation 17
   4.7 Summary of findings for IN100 18
5. FINITE ELEMENTS ANALYSIS OF CRACK TIP UNDER FATIGUE CYCLING WITH OVERLOADS 19
6. DISCUSSION 25

REFERENCES 28

APPENDICES
I. TOPOGRAPHIC DATA FROM FRACTURE SURFACES NEAR OVERLOAD SITES AND RESULTS OF ANALYSIS AI-1

1. Titanium Alloy (Ti-6Al-2Sn-4Zr-6Mo) Properties and Test Conditions AI-2
2. Fracture Surface Analysis Results AI-5

II IN100 NICKEL-BASE ALLOY AII-1

1. Nickel Based Super Alloy (IN100) Properties and Test Conditions AII-1
2. Fracture Surface Analysis Results AII-6

III. FRACTOGRAPHIC EXAMINATION OF HIGH-CYCLIC FATIGUE SPECIMEN AIII-1

SUMMARY AIII-1
SPECIMENS AIII-1
TOPOGRAPHY CHARACTERIZATION AIII-1
FAST FOURIER ANALYSIS AIII-3
FRACTURE SURFACE OBSERVATIONS AIII-5
STRESS INTENSITY CONSIDERATIONS AIII-5
CONCLUSIONS AIII-8

APPENDICES REFERENCES AIII-9

LIST OF FIGURES

Figure

1. Contrast and gray-scale elevation images of the area where an overload was applied.
2. A series of FAPPs showing movement of crack front.
3. Fracture progression curve for one of the overload areas generated by the FRASTA technique.
4. Deviation profile of the fractured area progression curve induced by the deformation in the vicinity of the crack tip due to overload.
5. Deviation profiles produced by different magnitude overloads with R = 0.05.
6. Deviation profiles produced by different magnitude overloads with R = 0.50.
7. Summary of maximum deviation observed for all cases of overload in two specimens of Ti-6Al-2Sn-4Zr-6Mo.
8. Deviation profiles of the areas of overload during fatigue loading with R = 0.05 and frequency of 20 Hz.
9. Deviation profiles of the areas of overload during fatigue loading with R = 0.05 and frequency of 0.1667 Hz.
10. Deviation profiles of the areas of overload during fatigue loading with R = 0.50 and frequency of 20 Hz.
11. Deviation profiles of the areas of overload during fatigue loading with R=0.50 and frequency of 0.1667 Hz.
12. Maximum deviation as a function of K_{max} for four different baseline fatigue loadings in IN100 specimens.
13. Estimated K_{max} from maximum deviation as a function of K_{max} for four different baseline fatigue loadings in IN100 specimens.
14. Estimated K_{max} as a function of applied K_{max} for four different loading conditions in IN100 specimens.
15. Finite element model of a compact tension specimen.
16. Fine mesh around the crack tip.
17. Cyclic loading history.
18. Power law model for Ti-6Al-2Sn-4Zr-6Mo.
19. Calculated crack tip opening displacement and plastic zone.
20. Calculated stress field around the crack tip.
21. Crack face opening displacement as a function of number of cycles calculated by the finite element method.

AI-1 Crack length vs. number of cycles for two specimens that experienced several single-cycle overloads.

AI-2 Contrast and gray-scale elevation images of fracture surface area surrounding overload site

AI-3. Fractured area projection plots (FAPPs) indicating the progression of the crack front.

AI-4 Increase in fractured area with increased spacing of the conjugate topographs.

AI-5 Deformation profile of the crack front in the vicinity of overload application.

AI-6 Contrast and gray-scale elevation images of fracture surface area surrounding overload site.

AI-7 Fractured area projection plots (FAPPs) indicating the progression of the crack front.

AI-8 Increase in fractured area with increased spacing of the conjugate topographs.

AI-9 Deformation profile of the crack front in the vicinity of overload application.

AI-10 Contrast and gray-scale elevation images of fracture surface area surrounding overload site.

AI-11. Fractured area projection plots (FAPPs) indicating the progression of the crack front.

AI-12 Increase in fractured area with increased spacing of the conjugate topographs.

AI-13 Deformation profile of the crack front in the vicinity of overload application.

AI-14 Contrast and gray-scale elevation images of fracture surface area surrounding overload site.

AI-15 Fractured area projection plots (FAPPs) indicating the progression of the crack front.

AI-16 Increase in fractured area with increased spacing of the conjugate topographs.

AI-17 Deformation profile of the crack front in the vicinity of overload application.

AI-18 Contrast and gray-scale elevation images of fracture surface area surrounding overload site.

AI-19 Fractured area projection plots (FAPPs) indicating the progression of the crack front.

AI-20 Increase in fractured area with increased spacing of the conjugate topographs.

AI-21 Deformation profile of the crack front in the vicinity of overload application.

AI-22 Contrast and gray-scale elevation images of fracture surface area surrounding overload site.

AI-23 Fractured area projection plots (FAPPs) indicating the progression of the crack front.

AI-24 Increase in fractured area with increased spacing of the conjugate topographs.

AI-25 Deformation profile of the crack front in the vicinity of overload application.

AI-26 Contrast and gray-scale elevation images of fracture surface area surrounding overload site.

AI-27 Fractured area projection plots (FAPPs) indicating the progression of the crack front.

AI-28 Increase in fractured area with increased spacing of the conjugate topographs.

AI-29 Deformation profile of the crack front in the vicinity of overload application.

AI-30 Contrast and gray-scale elevation images of fracture surface area surrounding overload site.

AI-31 Fractured area projection plots (FAPPs) indicating the progression of the crack front

AI-32 Increase in fractured area with increased spacing of the conjugate topographs

AI-33 Deformation profile of the crack front in the vicinity of overload application.

AI-34 Contrast and gray-scale elevation images of fracture surface area surrounding overload site.

AI-35 Fractured area projection plots (FAPPs) indicating the progression of the crack front.

AI-36 Increase in fractured area with increased spacing of the conjugate topographs.

AI-37 Deformation profile of the crack front in the vicinity of overload application.

AII-1 Crack length versus number of cycles for IN100 specimen 82-213 showing the effects of overload on crack growth behavior.

AII-2 Crack length versus number of cycles for IN100 specimen 82-213 showing the effects of overload on crack growth behavior.

AII-3 Contrast and gray-scale elevation images of fracture surface area surrounding 37.5 MPa√m overload site in baseline fatigue loading with R=0.05 and freq=20 Hz.

AII-4 Fractured area projection plots (FAPPs) indicating the progress of the crack front.

AII-5 Increase in fractured area with increased spacing of the conjugate topographs.

AII-6 Deformation profile of the crack front in the vicinity of 37.5 MPa√M overload site in baseline fatigue loading with R=0.05 and freq=20 Hz.

AII-7 Contrast and gray-scale elevation images of fracture surface area surrounding 45.0 MPa√m overload site in baseline fatigue loading with R=0.05 freq=20 Hz.

AII-8 Fractured area projection plots (FAPPs) indicating the progression of the crack front.

AII-9 Increase in fractured area with increased spacing of the conjugate topographs.

AII-10 Deformation profile of the crack front in the vicinity of 45.0 MPa√m overload site in baseline fatigue loading with R=0.05 and freq=20 Hz.

AII-11 Contrast and gray-scale elevation images of fracture surface area surrounding the 52.5 MPa√m overload site in baseline fatigue loading with R=0.05 and freq=20 Hz.

AII-12 Fractured area projection plots (FAPPs) indicating the progression of the crack front.

AII-13 Increase in fractured area with increased spacing of the conjugate topographs.

AII-14 Deformation profile of the crack front in the vicinity of 52.5 MPa√m overload site in baseline fatigue loading with R=0.05 and freq=20 Hz.

AII-15 Contrast and gray-scale elevation images of fracture surface area surrounding 37.5 MPa√m overload site in baseline fatigue loading with R=0.05 and freq=0.1667 Hz.

AII-16 Fractured area projection plots (FAPPs) indicating the progression of the crack front.

AII-17 Increase in fractured area with increased spacing of the conjugate topographs.

AII-18 Deformation profile of the crack front in the vicinity of 37.5 MPa√m overload site in baseline fatigue loading with R=0.05 and freq=0.1667 Hz.

AII-19 Contrast and gray-scale elevation images of fracture surface area surrounding the 45.0 MPa√m overload site in baseline fatigue loading with R=0.05 and freq=0.1667 Hz.

AII-20 Fractured area projection plots (FAPPs) indicating the progression of the crack front.

AII-21 Increase in fractured area with increased spacing of the conjugate topographs.

AII-22 Deformation profile of the crack front in the vicinity of the 45.0 MPa√m overload site in baseline fatigue loading with R=0.05 and freq=0.1667 Hz.

AII-23 Contrast and gray-scale elevation images of fracture surface area surrounding the seven cycles of 52.5 MPa√m overload site in baseline fatigue loading with R=0.05 and freq=0.1667 Hz.

AII-24 Fractured area projection plots (FAPPs) indicating the progression of the crack front

AII-25 Increase in fractured area with increased spacing of the conjugate topographs.

AII-26 Deformation profile of the crack front in the vicinity of the seven cycles 52.5 MPa√m overload site in baseline fatigue loading with R=0.05 and freq=0.1667 Hz.

AII-27 contrast and gray-scale elevation images of single 52.5 MPa √m overload in R=0.05 and freq=0.1667 Hz baseline fatigue region.

AII-28 Fractured area projection plots (FAPPs) indicating the progression of the crack front.

AII-29 Increase in fractured area with increased spacing of the conjugate topographs.

AII-30 Deformation profiles of the crack front in the vicinity of 52.5 MPa√m overload in the baseline fatigue loading of R=0.05 and 0.1667 Hz.

AII-31 Contrast and gray-scale elevation images of single 37.5 MPa √m overload in R=0.50 and freq=20 Hz baseline fatigue region.

AII-32 Fractured area projection plots (FAPPs) indicating the progression of the crack front.

AII-33 Increase in fractured area with increased spacing of the conjugate topographs.

AII-34 Deformation profile of the crack front in the vicinity of 37.5 MPa√m overload in the base fatigue loading of R=0.50 and 20 Hz.

AII-35 Contrast and gray-scale elevation images of single 45.0 MPa √m overload in R=0.50 and freq=20 Hz baseline.

AII-36 Fractured area projection plots (FAPPs) indicating the progression of the crack front.

AII-37 Increase in fractured area with increased spacing of the conjugate topographs.

AII-38 Deformation profile of the crack front in the vicinity of 45.0 MPa√m overload in the base fatigue loading of R=0.50 and 20 Hz.

AII-39 Contrast and gray-scale elevation images of single 52.5 MPa √m overload in R=0.50 and freq=20 Hz baseline fatigue region.

AII-40 Fractured area projection plots (FAPPs) indicating the progression of the crack front.

AII-41 Increase in fractured area with increased spacing of the conjugate topographs.

AII-42 Deformation profile of the crack front in the vicinity of 52.5 MPa√m overload in the base fatigue loading of R=0.50 and 20 Hz.

AII-43 Contrast and gray-scale elevation images of single 37.5 MPa √m overload in R=0.50 and freq=0.1667 Hz baseline fatigue region.

AII-44 Fractured area projection plots (FAPPs) indicating the progression of the crack front.

AII-45 Increase in fractured area with increased spacing of the conjugate topograph.

AII-46 Deformation profile of the crack front in the vicinity of 37.5 MPa√m overload in the base fatigue loading of R=0.50 and 0.1667 Hz.

AII-47 Contrast and gray-scale elevation images of single 45.0 MPa √m overload in R=0.50 and freq=0.1667 Hz baseline fatigue region.

AII-48 Fractured area projection plots (FAPPs) indicating the progression of the crack front.

AII-49 Increase in fractured area with increased spacing of the conjugate topographs.

AII-50 Deformation profiles of the crack front in the vicinity of 45.0 MPa√m overload in the baseline fatigue loading of R=0.50 and 0.1667 Hz.

AII-51 Contrast and gray-scale elevation images of single 52.5 MPa √m overload in R=0.50 and freq=0.1667 Hz baseline fatigue region.

AII-52 Fractured area projection plots (FAPPs) indicating the progression of the crack front.

AII-53 Increase in fractured area with increased spacing of the conjugate topographs.

AII-54 Deformation profiles of the crack front in the vicinity of 52.5 MPa√m overload in the baseline fatigue loading of R=0.50 and 0.1667 Hz.

AIII-1 Macro SEM photographs of four tensile fatigue specimens.

AIII-2 Examples of contrast and gray-scale elevation images at different locations from the exterior surface of the specimen. In the elevation images white areas are high in elevation and dark areas low. (Test condition R=0.1)

AIII-3 EPSD curves for the first nine areas from the exterior surface for R=0.10 test.

AIII-4 $(EPSD)^{1/2}$ as a function of crack depth for specimens tested at different R-values.

AIII-5 $(EPSD)^{1/2}$ as a function of stress intensity range (ΔK) for specimens tested at different R-values.

AIII-6 Stress intensity range (ΔK) at which the $(EPSD)^{1/2}$ value started to increase linearly for different stress ratios.

AIII-7 Slope of the curves of $(EPSD)^{1/2}$ versus δK as a function of R.

LIST OF TABLES

Table

1. Calculated plastic zone sizes in titanium alloy under plane strain conditions
2. Material properties for titanium Ti-6Al-2Sn-4Zr-6Mo
AI-1. Mechanical properties of Ti-6Al-2Sn-4Zr-6Mo at room temperature
AI-2 Test conditions for Ti-alloy specimen no. 97-100 (R= 0.05).
AI-3 Test conditions for TI-alloy specimen no. 97-101 (R = 0.50)
AII-1 Mechanical properties of IN100
AII-2 Test conditions for IN100 specimen no. 82-213 (R = 0.05)
AII-3 Test conditions for IN100 specimen no. 82-216 (R = 0.50)
AII-4 Calculated plastic zone sizes under plane strain condition
AIII-1 Specimen geometry and fatigue loading conditions

EXECUTIVE SUMMARY

Fatigue of aircraft components is a major DoD problem, resulting in large annual costs and sporadic fleet groundings. The problem could be reduced if fatigue crack growth could be more reliably predicted. More accurate predictions require that effects of overload be accounted for in the continuum fracture mechanics models used to design components and predict their mission life. The work reported here attempted to improve these models by providing understanding and measurements of the deformation produced by an overload at a fatigue crack front.

Current understanding links overload effects with changes in the plastic zone at the crack tip. These changes are difficult to observe directly, so they are characterized by empirical parameters deduced from test data. We sought to observe, measure, and analyze these changes by taking a new approach—measuring and analyzing topological features on fatigue failure surfaces where overloads were applied.

Fatigue failure surfaces of titanium and nickel alloys were produced under well-controlled load conditions by workers at the AFRL. Fatigue cracks were grown through compact tension specimens at constant baseline stress intensities, stress ratios, and frequencies. Overloads of several magnitudes were applied after several mm of crack growth so that effects of individual overloads were clearly separable from later overloads. The failed specimens were provided to SRI for characterization and analysis.

The topographies of fracture surface areas around overloads were quantified by scanning laser confocal optics microscopy. Topographs of conjugate fracture surfaces were juxtaposed and positioned relative to each other to simulate the configuration of the crack faces during the fatigue tests. Crack growth was simulated by displacing the conjugate topographs. The progress of a fatigue crack is shown in fractured area projection plots (Figure 2, for example) or in cross section plots (Figure 3).

The disruptive effect of an overload on the otherwise steady fracture progression curve (Figure 3) is obtained by computing crack length (relative FAPP area) as a function of conjugate surface separation. In the region outside the overload this curve is linear; near the overload site the curve deviates from linearity. In analyzing fatigue cracking under conditions without overload, conjugate surface separation can be related directly to the number of cycles and the deviation from the linear relation. This indicates how much the crack has slowed, the size of the stretch zone, and the extent of the region of influence for the overload. Although we used the same procedure for analyzing specimens with overload, it became clear that more understanding was needed to relate the conjugate surface separation to the number of cycles.

For the titanium alloy (Ti-6Al-2Sn-4Zr-6Mo) tested at a baseline Kmax of 15 MPa$\sqrt{m}$, the peak deviations increased monotonically with overload magnitude at R = 0.05; however, no relation was indicated at R = 0.5. The crack tip stretch zone increased from about 0.24 to 0.52 μm and the extent of influence increased from about 1 to 1.5 mm as overload magnitude increased from 18.75 MPa$\sqrt{m}$ to 22.5 MPa$\sqrt{m}$. For the nickel based

superalloy (IN100) at 650 and tested at a baseline Kmax of 30 MPa√m, the crack tip stretch zone increased from about 0.6 to 1.8 μm and the extent of influence increased from about 0.5 to 1.0 mm as overload magnitude increased from 37.5 MPa√m to 52.5 MPa√m. For both materials the zone of influence extended behind the crack front, and the peak deformation occurred after the overload location. The IN100 material also exhibited an effect of frequency.

To better understand the development of the plastic zone at the crack tip, we performed detailed finite element analyses for a single case of fatigue of titanium with Kmax of 15 MPa√m and R of 0.5. The region around the crack tip was examined at very high resolution. We performed cyclic analyses including overload and crack growth. The analysis provides an explanation for the retardation effect of overload: in cycles following the overload the stress state around the crack tip is significantly less tensile than before the overload.

In summary, fatigue overloads produce a distinctive deformation signature that can be detected by quantitative fractography (although not reliably by SEM examination). This profile identifies the occurrence of overloads. We analyzed the surfaces in terms of crack length vs. conjugate surface separation and quantified the effects of overload in terms of deviation from linear. Under certain conditions of stress ratio, the amount of deviation relates to the magnitude of the overload. More work is needed to understand the relationship between conjugate surface separation and number of cycles. Detailed finite element analysis would help gain this understanding. If these initial findings can be confirmed, expanded, and related to cyclic load spectra, then fatigue retardation models, and hence, lifetime prediction capability can be improved.

1. INTRODUCTION

Fatigue of critical components of fighters and rotorcraft is an enormous DoD problem. For example, the cracks that form and grow in fighter turbine blades and helicopters under vibrational loads and sporadic overloads during service have caused many Class A incidents (loss of aircraft or life) in the Air Force and Army fleets. These fatigue failures result in costly redesigns and retrofits, and huge inspection and maintenance costs. In addition, fatigue failures cause the fleet to be grounded periodically for days to weeks, leaving the Air Force and Army in an unacceptable posture of unreadiness.

The fatigue problem could be reduced if fatigue crack growth behavior could be predicted more reliably. Inspection intervals could be set with more confidence, conservatism could be taken out of component design, and aircraft could be repaired or retired before a Class A incident is imminent. However, the damage tolerant philosophy used to manage aircraft component integrity requires an improved mathematical model for fatigue damage evolution.

The empirical Paris law, which relates crack growth rate to the stress intensity range, ΔK, provides reliable lifetime estimates under steady-state cyclic load conditions [1]. Unfortunately, the law is not generally applicable in the field, because overloads and underloads are ubiquitous during service and greatly affect crack growth rate. Retardation was a prominent topic of discussion at the recent International Conference on Fatigue Damage, where Dr. Paris himself underscored the need to understand and model the phenomenon [2].

Since the work of Willenborg [3] and Wheeler [4] in the early 70's, many investigators have addressed the fatigue overload phenomenon. Sadananda and Vasudevan and their colleagues [5] have reviewed the literature on fatigue overload, summarized the central observations, and reviewed the mechanisms and models of fatigue retardation. But despite the existence of theory-based models, many models in use today are based on empiricism [6].

Since fatigue crack growth is governed by plastic deformation occurring at the crack tip, answers must be sought by examining the crack tip plastic zone. Conventional techniques have not yielded the understanding or data on overload effects needed for model development. Moreover, the interactions of overlapping plastic zones from closely spaced overloads are nonlinear, therefore complicating the task.

The work reported here attempted to address this problem from a new perspective, namely quantitative fractography. We used a confocal optics procedure to rapidly map the topographies of failure surfaces produced under cyclic load conditions with predetermined overloads. Then we applied the FRASTA technique [7,8] to position the conjugate topographs in the configuration of the fracture surfaces during fatigue crack growth. The deformation at the crack tip and the crack front advance that occurred during application of an overload were indicated in planar and cross section views of the crack front. The additional topograph displacement required for the crack front to

penetrate the overload area was measured and may serve as the basis of a retardation model.

The retardation model was inserted into the LSDYNA3D [9] and FRANC2D.6 [10] finite element codes. The experiments performed in this work were simulated with the model, and the predicted and measured crack tip blunting were compared. Animated videos of fatigue crack growth through titanium and nickel alloys show the retardation at overloads of various magnitudes.

2. OBJECTIVES AND APPROACH

Our objective was to understand the details of deformation and fracture processes in the vicinity of a fatigue crack tip at positions where an overload was applied. The results are expected to improve models of crack growth retardation and, hence, enable more accurate life predictions of aircraft components. A second objective was to evaluate the effect of stress ratio on fracture surface topography in high cycle fatigue specimens. Our approach for both objectives was to analyze fracture surface topographies, reconstruct the crack growth process with the FRASTA technique, relate indicated crack front deformation characteristics to crack growth history and load conditions, and to analyze these results with finite element computations.

2.1 Fatigue Fracture Surface Generation, Characterization, and Analysis

Fracture surfaces were provided by AFRL personnel, who performed a series of fatigue tests on compact tension specimens fabricated from Ti-6Al-2Sn-4Zr-6Mo and IN100 plates. During each test, single cycle overloads of different magnitudes were applied after a certain amount of crack growth. Details of the tests are presented in the Appendices.

The topographies of fracture surface areas around overloads were quantified by scanning laser confocal optics microscopy. Topographs of conjugate fracture surfaces were juxtaposed and positioned relative to each other to simulate the configuration of the crack faces during the fatigue tests. Crack growth was simulated by displacing the conjugate topographs. The progress of a fatigue crack is shown in fracture area projection plots or in cross section plots.

For each specimen a series of fractured area projection plots (FAPPs) was produced and superimposed on the scanning laser microscope contrast image of fracture surfaces. These FAPP-superimposed photographs illustrate critical details of the crack front movement in the plastic zone. The cross-sectional plots (XSPs) show changes in the crack tip opening displacement and opening angles. The fracture progression curve (FPC), i.e. the increase in fractured area as a function of conjugate surface spacing, delineates the effect of overload and underload as a degree of deviation from a linear line. The procedure is known as FRASTA (Fracture Surface Topography Analysis) and is described in detail in References 7 and 8.

The disruptive effect of an overload on the otherwise steady crack growth rate is shown in fracture progression plots obtained by computing crack length (relative FAPP areas) and converting topograph displacement to plastic opening displacement. Deviation from the linear steady state relation indicates the size of the stretch zone, how much the crack has slowed, and the linear extent of the overload influence.

We applied the FRASTA technique to all areas of the fracture surfaces where an overload was applied. The procedure is illustrated on a fracture surface area of a titanium alloy specimen in which a single cycle overload was applied during the baseline fatigue loading.

Figure 1 shows the contrast and gray-scale elevation images of the fracture surface.

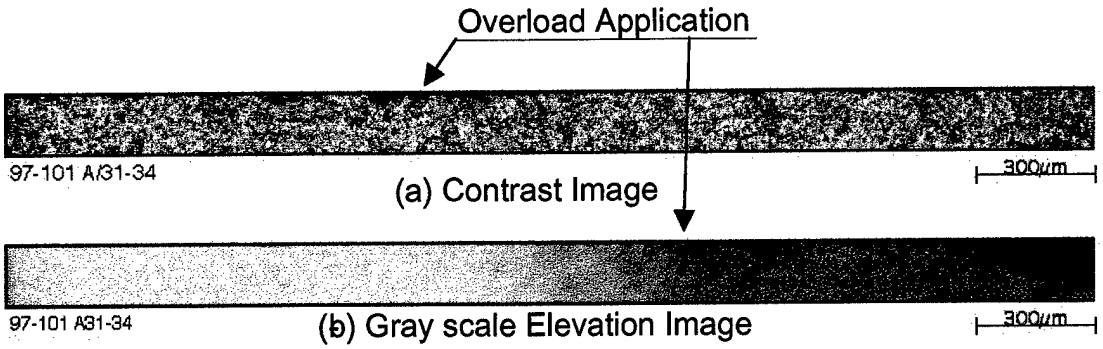

Figure 1. Contrast and gray-scale elevation images of the area where an overload was applied.

Using the conjugate elevation data files in the FRASTA program, the fracture process was reconstructed, and the resulting series of FAPPs is shown in Figure 2.

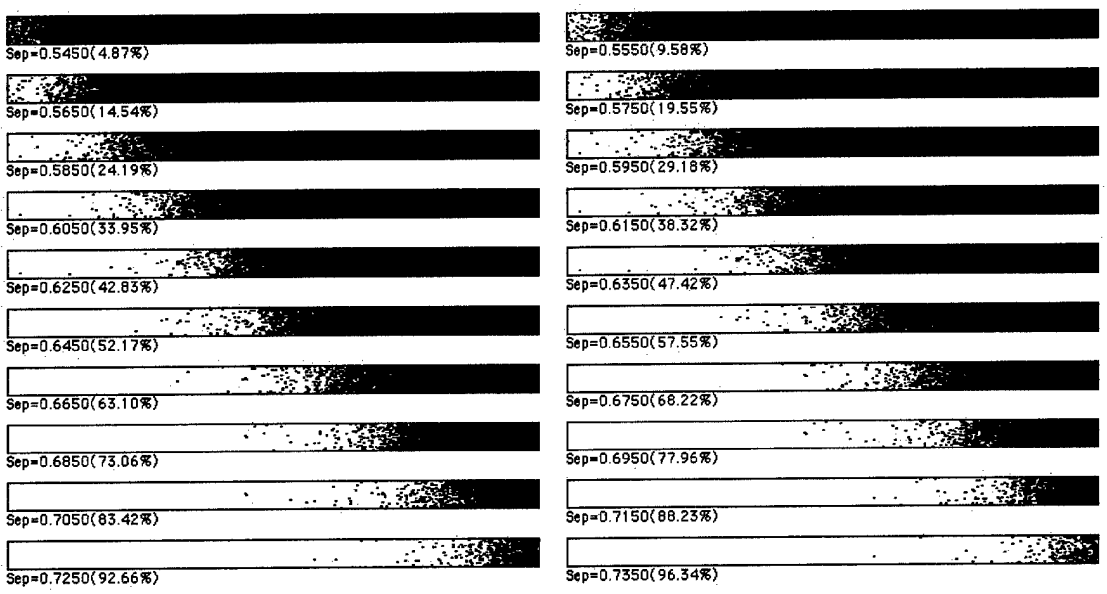

Figure 2. A series of FAPPs showing movement of crack front.

In these plots the white areas are where the topographs are separated and therefore represent cracked area. Black areas are where the topographs overlap and hence represent uncracked area. The boundary between black and white represents the crack front. Note that the crack front is not well defined as a sharp line. This is caused by neglect of elastic deformations when the conjugate topograph matching is done, and by minute errors in the elevation data at each pixel point on the surface. The confocal microscope determines the elevation at each pixel point of the surface with the possible error of ±0.2 % of the total range of elevation characterization. This means that the topographs determined by the confocal microscope are not single continuous surfaces,

but rather thin fuzzy layers. When one examines a topograph by itself, the fuzziness is not noticeable; however, when the conjugate surfaces are juxtaposed and the gaps between them are computed, the errors in the corresponding pixels are amplified, resulting in a fuzzy crack front.

Average crack front movement can be obtained by computing the cracked area as a percent of total area in each FAPP and plotting the result as a function of conjugate surface spacing. The result is shown in Figure 3.

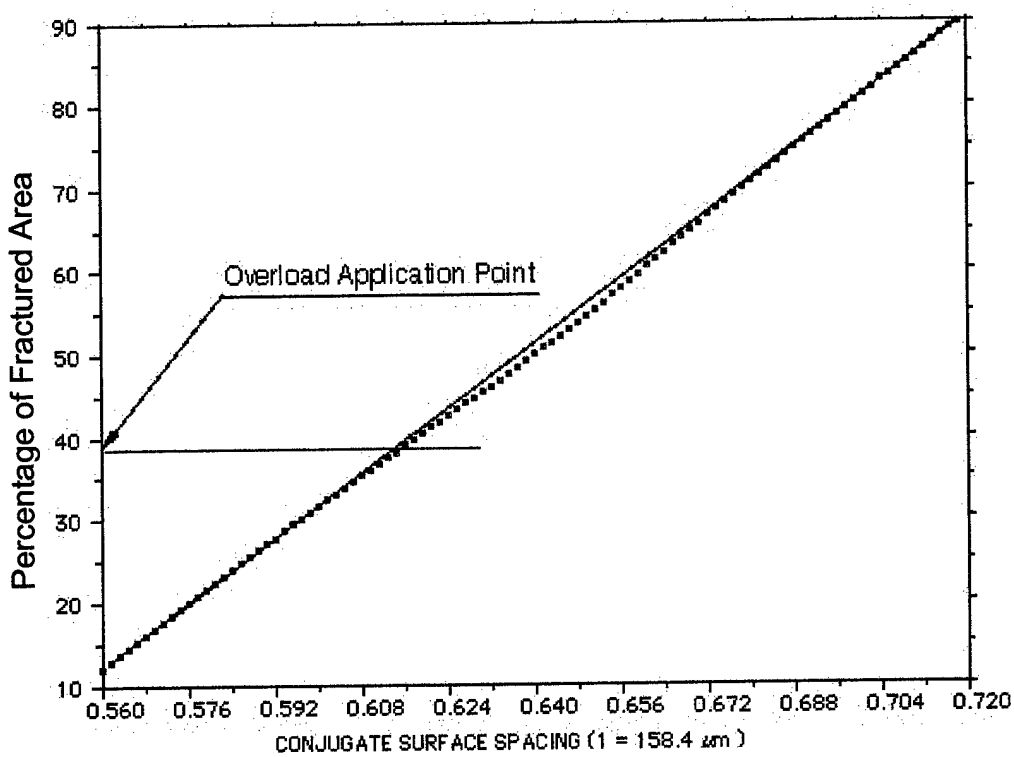

Figure 3. Fracture progression curve for one of the overload areas generated by the FRASTA technique

Assuming that the crack growth rate is steady-state before and after the region of influence of the overload, we expect the ends of the curve in Figure 3 to lie along a straight line. For the section of the fracture surface shown in Figure 3, up to about 35 % of the fractured area, the curve is linear; however, near the location of overload application, the curve deviates from linearity.

The deviation shows that additional conjugate surface separation is needed to advance the crack in the vicinity of the overload area. This finding is consistent with there being more plastic strain in the region around the overload. If the conjugate surface separation is related to the number of cycles, then the deviation shown in Figure 3 indicates a slowdown in crack propagation rate. Although for steady-state fatigue crack growth the conjugate surface separation is directly related to the number of cycles, the relationship is more complicated when overloads are applied. We present the following results in terms of the deviation from linear, but recognize that determining the effect of overload on

crack growth rate first requires a better understanding of how conjugate surface separation relates to the number of cycles.

The curve also indicates the extent of the influence of the overload. Deviation begins before the overload location and reaches a maximum after the location. Further, the profile of the deviation is gradual rather than sharp; suggesting that this particular overload did not arrest the crack, but probably only slowed it.

To determine more clearly the degree of deviation caused by the overload and enable comparison with other overloads, we converted the data to crack front position in micrometers from the edge of the observation window vs. conjugate surface separation in micrometers. Then the difference between the actual curve value and the reference line was used to determine the magnitude of deviation. The result is shown in Figure 4.

We will use the analysis methods described above to investigate the effects of overload.

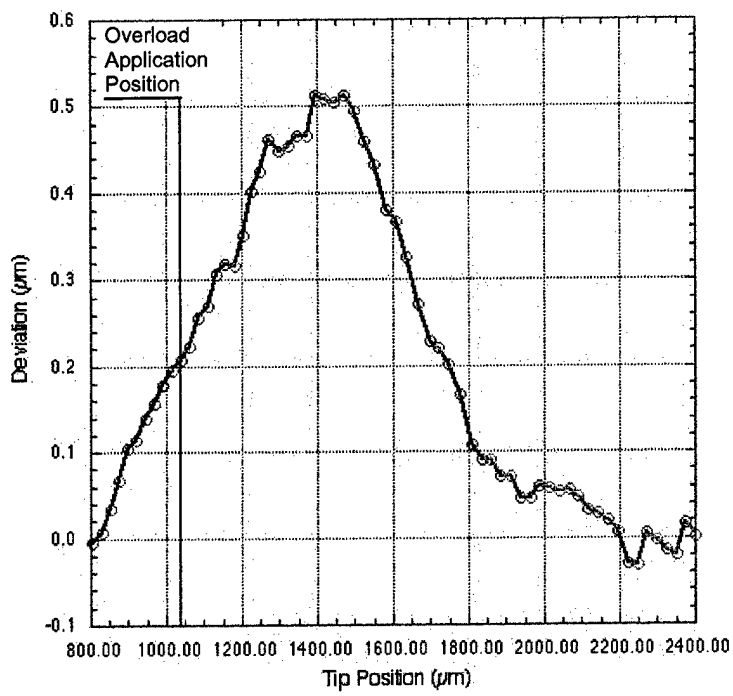

Figure 4. Deviation profile of the fractured area progression curve induced by the deformation in the vicinity of the crack tip due to overload.

3. RESULTS FOR TITANIUM ALLOY Ti-6Al-2Sn-4Zr-6Mo

We used the procedure described above to analyze the areas of the fracture surfaces of the two Ti alloy specimens around where overloads were applied. The two Ti-6Al-2Sn-4Zr-6Mo alloy specimens 97-100 and 97-101 were tested at stress ratios, R = 0.05 and R = 0.50 and two frequencies, 20 Hz and 0.1667 Hz. The shape and peak height of the deviation profiles show the effects of overload magnitude, stress ratio, and frequency. The details of the analyses for each overload area are presented in Appendix I. The results are summarized here.

3.1 Stress ratio, R = 0.05

Figure 5 summarizes the results for overloads at R=0.05. The positions of the deviation profiles were adjusted so that the overload application point was at the zero tip position.

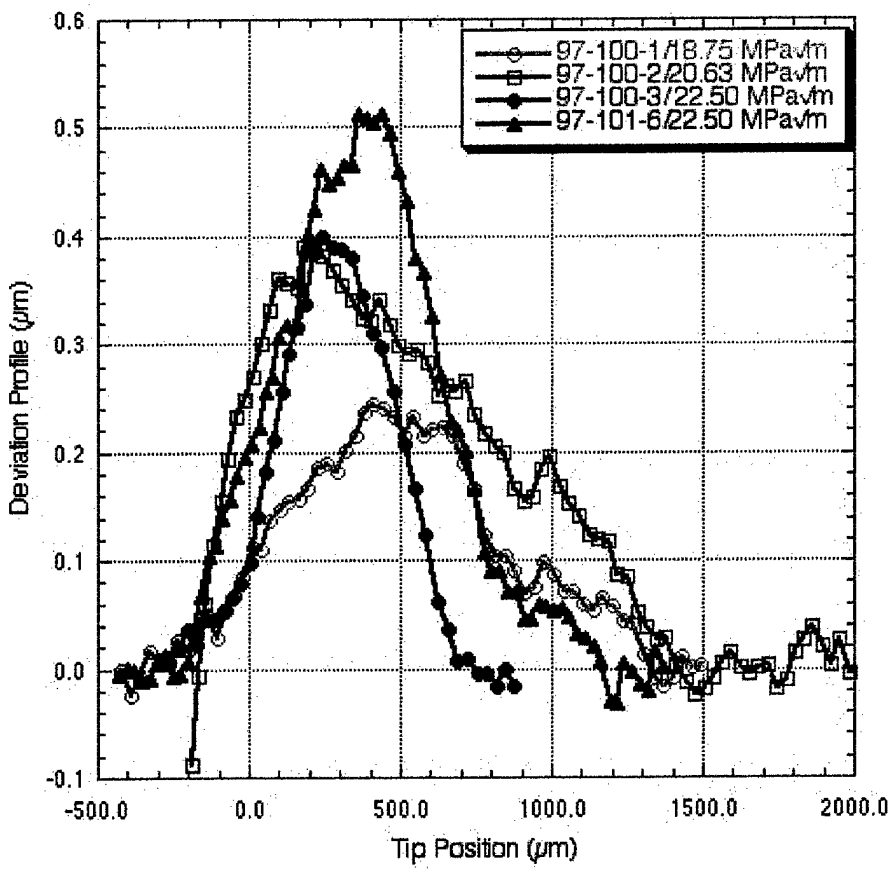

Figure 5. Deviation profiles produced by different magnitude overloads with R = 0.05.

Despite some scatter, the profiles show that:

1. Deviation starts before the actual overload application point.
2. Peak deviation occurs after the application point.
3. Deviation extends up to about 1 mm.

3.2 Stress ratio, R = 0.50

Figure 6 summarizes the results for overloads at R=0.50. The positions of the deviation profiles were adjusted so that the overload application point was at the zero tip position.

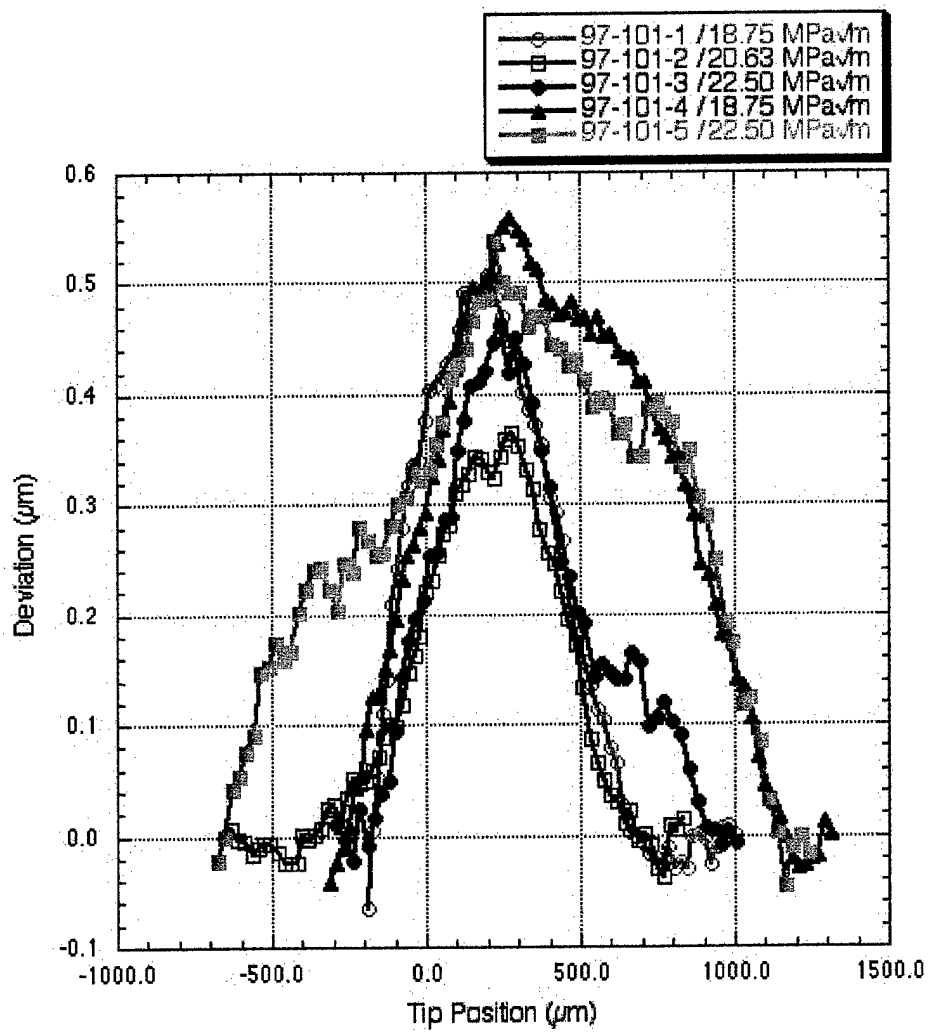

Figure 6. Deviation profiles produced by different magnitude overloads with R = 0.50.

The behavior is similar to that in Figure 5; however, the peak deviation increases monotonically with K_{max} for R = 0.05, but not for the R = 0.5 specimen, as shown in Figure 7. This difference may result from differences in crack closure—the K_{min} effect.

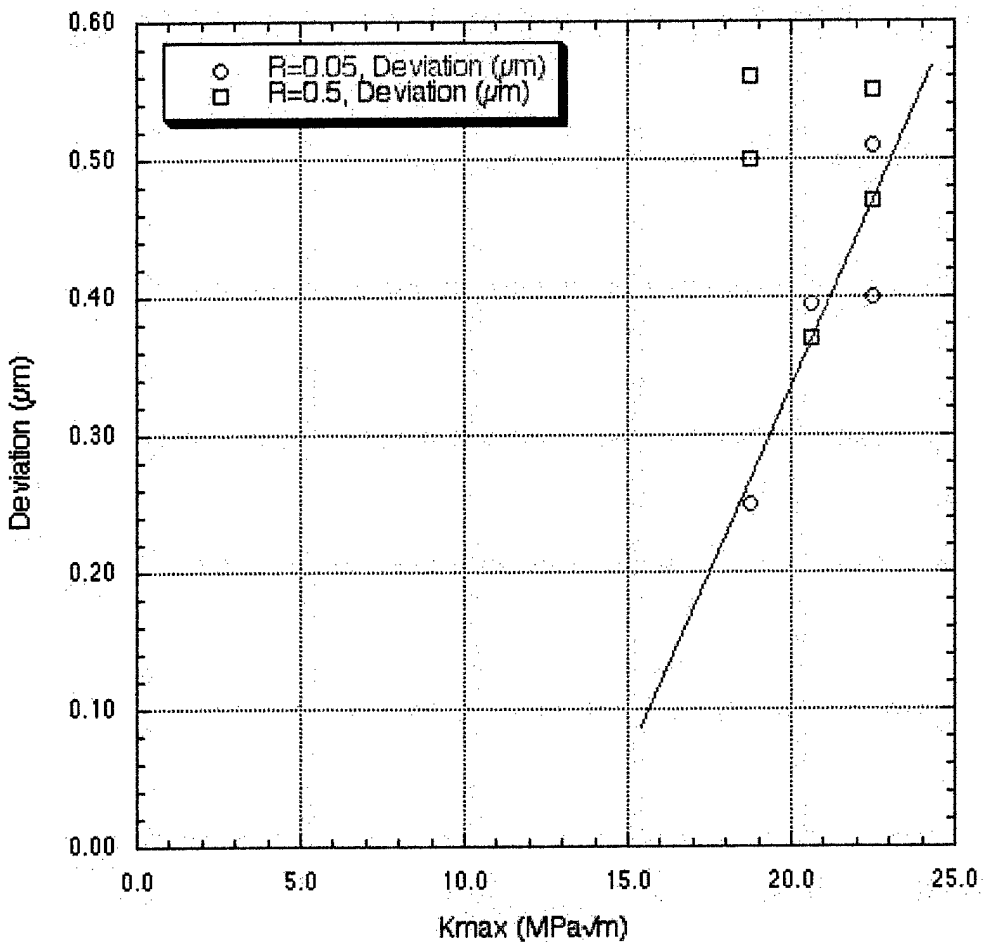

Figure 7. Summary of maximum deviation observed for all cases of overload in two specimens of Ti-6Al-2Sn-4Zr-6Mo.

The curves in Figures 5 and 6 have magnitudes of only 0.3 to 0.5 μm and hence are difficult to measure accurately. Overloads greater than 50% of the baseline stress intensity would perhaps produce more measurable deviations and less scatter. Noteworthy is the spread of the deviation about the location where the overload was applied. The deviation behind the crack front is likely due to the blunting, which effectively advances the crack. The deviation ahead of the crack front, however, extends 700 to 1500 μm into the material—about 50 times the plastic zone radius as calculated from fracture mechanics formula by substituting the properties shown in Table 1 into the equation:

$$r_p = \left(\frac{1}{6\pi}\right)\left(\frac{K}{\sigma_y}\right)^2 \quad (1)$$

where K is the applied stress intensity and σ_y is the yield strength. The results are tabulated in table 1.

TABLE 1. CALCULATED PLASTIC ZONE SIZES IN TITANIUM ALLOY UNDER PLANE STRAIN CONDITIONS

Applied Stress Intensity (MPa√m)	Radius of Plastic Zone (Plane Strain) (μm)
15.0	8.90
18.75	13.91
20.63	16.84
22.50	20.03

This discrepancy is not consistent with existing treatments of crack growth retardation, which predict that growth rates return to normal after the plastic zone is traversed [3,4]. The method used here, that produced these results, should be examined for its value in elucidating details of crack advance in overload-affected zones.

3.3 Summary of findings for titanium alloy

1. Overloads caused a deviation in the curve of fractured area vs. conjugate surface separation. Thus, FRASTA can be used to detect the existence of overloads in service components.
2. The perturbation in the deviation curve was not sharp (most of the deviation curves were nearly symmetrical), suggesting that the imposed overloads had no drastic effect on crack behavior (retardation or arrest).
3. An overload produces deformation before and after the crack tip position where the overload was applied. Maximum deviation occurs about 300 to 500 μm in front of the crack tip.
4. The deviation extended over about 1 mm of crack length, suggesting the length of overload influence.
5. Maximum values related to K_{max} in the case of R=0.05, but not in the case of R=0.50.

4. RESULTS FOR IN100 NICKEL-BASE ALLOY

In a companion project for the Air Force and DARPA, we examined a compact tension specimen of IN100 that had been tested under similar fatigue overload conditions. We present here the results of a second IN100 specimen and compare the findings with those from the companion project.

Two compact tension specimens, Specimen Nos. 82-213 and 82-216, were fatigue tested at 650°C at two frequencies, 20 Hz and 0.1667 Hz, in each sample. The Kmax value of the baseline fatigue loading was maintained at 30 MPa√m, but the Kmin differed for the two specimens. The test records are shown in Tables AII-1 and AII-2. Table AII-4 gives the calculated plastic zone radii under plane strain conditions.

Unlike the Ti-6Al-2Sn-4Zr-6Mo alloy specimens that did not show distinct effects of overload on the crack growth behavior, the IN100 specimens show significant effects (see Figure AI-1 in Appendix I and Figures AII-2 and AII-3 in Appendix II). Slower crack growth, and in some cases prolonged arrest, resulted from the overload application.

The load history of Specimen No. 82-216 is more complex than for Specimen No. 82-213, because the baseline loading had to be increased in order to reinitiate the crack after the 52.5 MPa√m overloads--40 MPa√m in the 20Hz section and 35 MPa√m in the 0.1667 section. Furthermore, an overload of 45 MPa√m at a crack length of 28.46 mm was applied after an overnight pause at the minimum load (15MPa√m), a prolonged static loading that may influence the deformation at the crack tip.

The seven continuous cycle overload in Specimen 82-213 provides an opportunity to compare multiple overloads with single overloads.

We examined all areas of the fracture surfaces where overloads were applied. Deviation profiles were obtained and are presented below in terms of stress ratio and frequency.

4.1 Stress ratio, R=0.05 and 20 Hz

Three magnitudes of overload were applied; the deviation profiles are presented in Figure 8. The deviation profile curves were shifted so that the overload application point was adjusted to the zero tip position in the graph. The figure shows the characteristic shape of deviation profiles. The deviation starts before the overload point, and the maximum occurs about 100 μm after the overload point. The deviation profiles have a skewed bell shape, starting before the overload point and showing that material behind as well as in advance of the crack front plastically deforms and contributes to crack tip blunting. The figure also shows that deviation magnitude increases with overload magnitude.

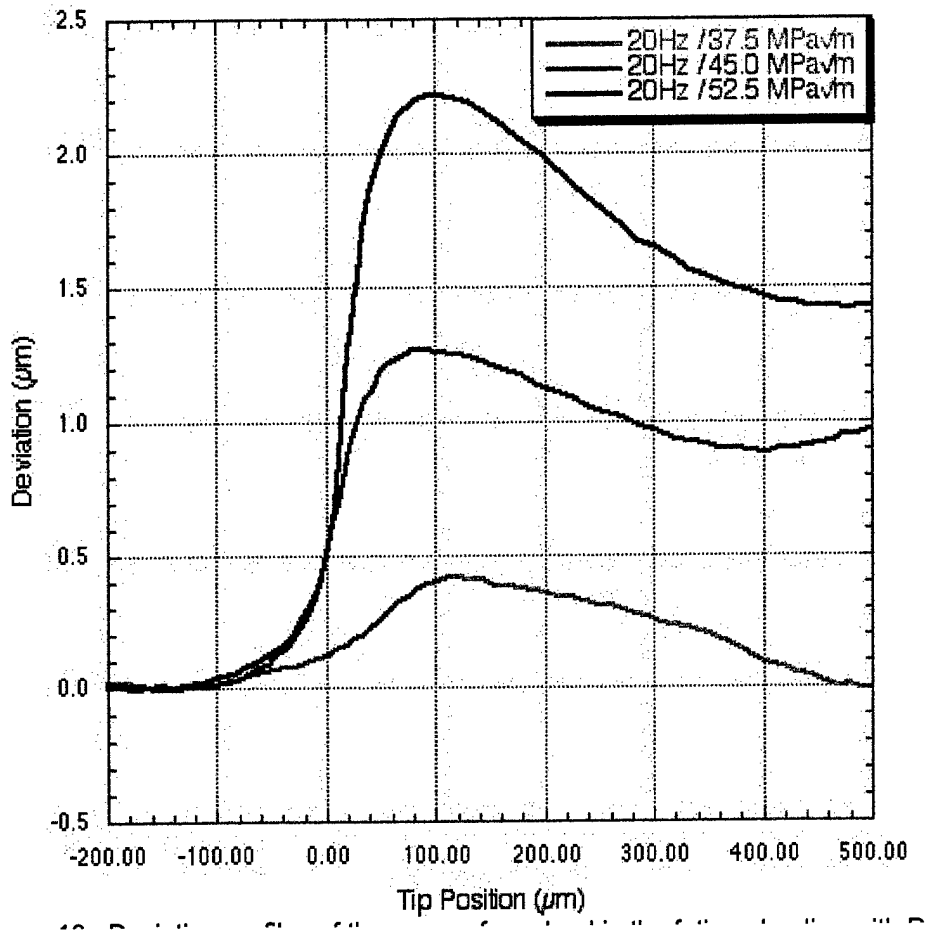

Figure 8. Deviation profiles of the areas of overload during fatigue loading with R=0.05 and frequency of 20 Hz.

4.2 Stress ratio, R=0.05 and 0.1667 Hz

Three magnitudes of single cycle overload were applied in the areas of baseline fatigue loading of R= 0.05 and frequency of 0.1667 Hz. In addition, seven cycles of 52.5 MPa√m were applied in the same baseline fatigue loading. The deviation profiles of the overload areas are presented in Figure 9. The level of deviation profile curves is proportional to the magnitude of overloads. Multiple overloads increase the deviation and also expand the influence range. The expansion of the affected zone may result from slight crack extension during multiple high overloads. This additive nature of multiple overloads is evident.

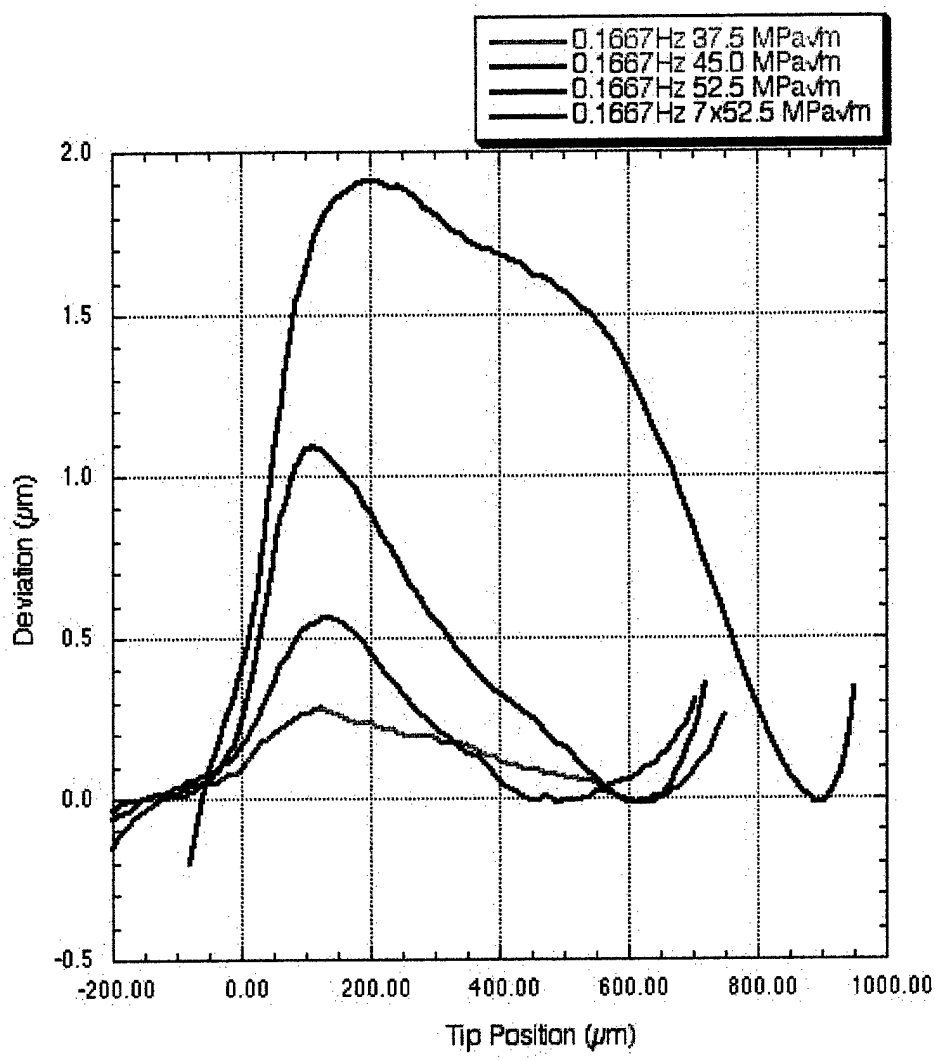

Figure 9. Deviation profiles of the areas of overload during fatigue loading with R=0.05 and frequency of 0.1667 Hz.

4.3 Stress ratio, R=0.50 and 20 Hz

Three magnitudes of single cycle overload were applied in the areas of the baseline fatigue loading with R=0.50 and 20 Hz. The deviation profiles of the overload areas are shown in Figure 10.

The deviation profiles for the cases of R=0.50 differ significantly from those at R = 0.05. The proportionality of the level of deviation profiles to the magnitude of the overloads is lost, and the deviation profiles of 37.5 MPa√m and 45.0 MPa√m overloads are lower. The deviation level increases abruptly at an overload magnitude of 52.5 MPa√m.

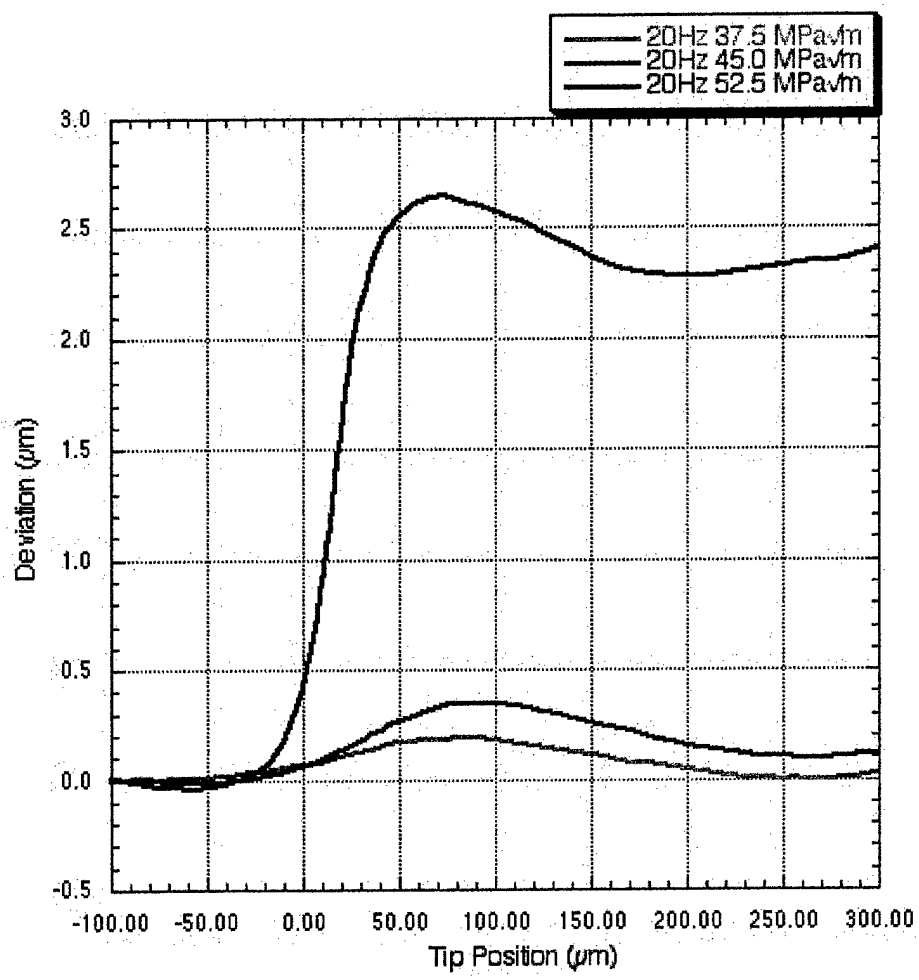

Figure 10. Deviation profiles of the areas of overload during fatigue loading with R=0.50 and frequency of 20 Hz.

4.4 Stress ratio, R=0.50 and 0.1667 Hz

Three different magnitudes of overload were applied in the areas of baseline fatigue loading of R=0.50 and 0.1667 Hz frequency. The deviation profiles were calculated and plotted in Figure 11. No deviation resulted from the 37.5 MPa√m overload, but the deviation increased sharply between the overload magnitudes of 45.0 MPa√m and 52.5 MPa√m.

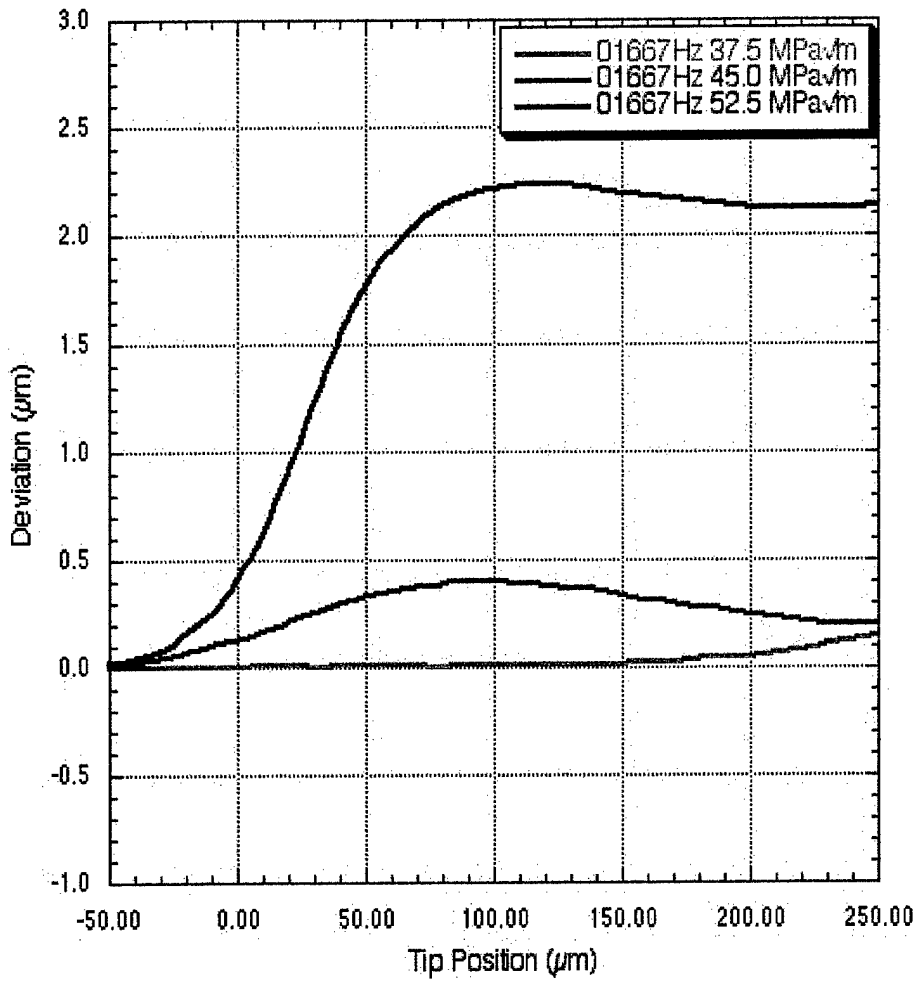

Figure 11. Deviation profiles of the areas of overload during fatigue loading with R=0.50 and frequency of 0.1667 Hz.

4.5 Maximum Deviation vs K_{max} for all load conditions

We examined the three sets of overload magnitudes in the four different baseline fatigued areas (two different R-values and two different frequencies). In order to see the effect of not only the overload magnitude, but also the stress ratios and frequencies on the deformation around the crack tip, we plotted the maximum deviation value as a function of K_{max} in Figure 12.

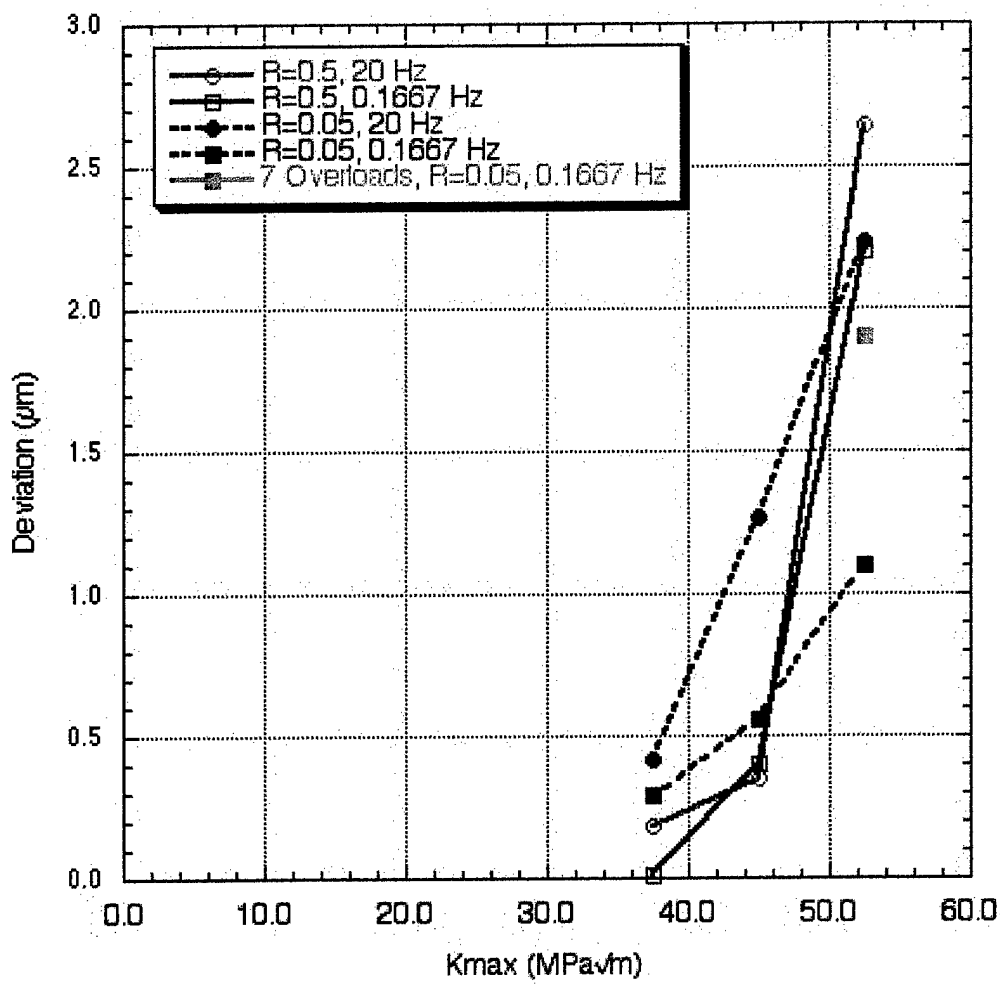

Figure 12. Maximum deviation as a function of K_{max} for four different baseline fatigue loadings in IN100 specimens.

The lines for the three cases (R=0.5, 20 Hz, R=0.05, 20 Hz, and R=0.05, 0.1667Hz) converge to zero deviation at 30 MPa√m, perhaps implying that the surface distortion measured in the vicinity of an overload is superimposed on the deformation produced by the baseline fatigue loading. In other words, we are measuring the effect of the differences between the overload and baseline fatigue loading.

When the stress ratio is very low (R=0.05) the surface deformation by the overload is more proportional to the magnitude of overload. When the stress ratio is higher (R=0.50) and the overload magnitude is lower, the deformation by the overload is not distinguishable from that of the baseline fatigue loading.

4.6 Assessment of Overload Magnitude from the Deviation

We attempted to assess the applied overload stress intensity factor using the deviation information. The overload apparently produced steps in crack opening displacement as shown in the deviation profiles (Figures 8 through 11). As done before, the crack tip opening displacement is related to the stress intensity using equation (2):

$$K = \sqrt{\frac{\delta \sigma_o E}{1-\nu^2}} \quad (2)$$

where δ is the crack tip opening displacement, σ_o is a flow stress (average of yield strength and ultimate strength), E is a modulus of elasticity, and ν is Poisson's ratio. Using the properties $E = 210$ GPa, $\sigma_o = 1062$ MPa, $\nu = 0.3$, and δ as the peak value of deviation shown in Figures 8 through 11, we obtained the results shown in Figure 13.

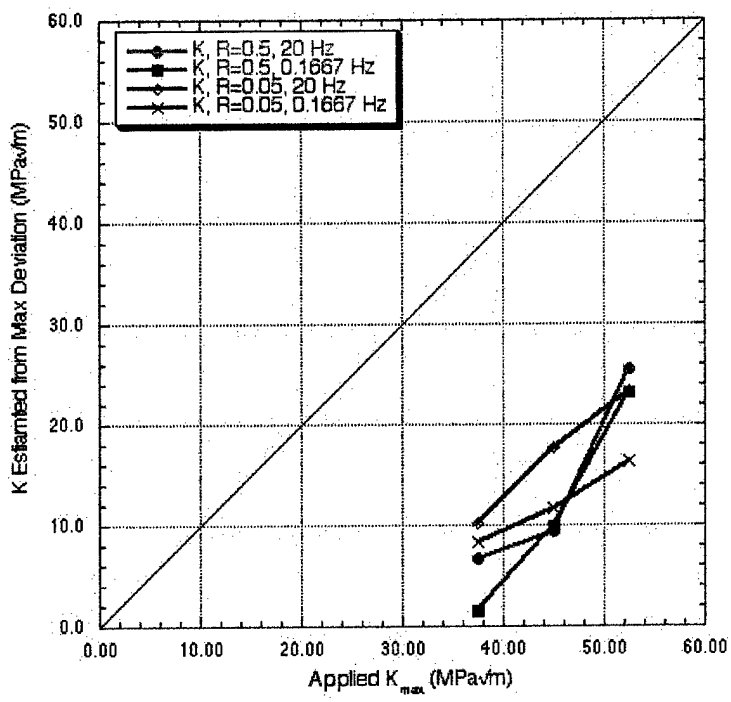

Figure 13. Estimated K_{max} from maximum deviation as a function of K_{max} for four different baseline fatigue loadings in IN100 specimens.

The estimated stress intensity values are much lower than the applied maximum stress intensity factors, possibly because the crack opening due to the baseline fatigue loading is neglected.

If the baseline fatigue loading $K_{max} = 30$ MPa√m is added to each value shown in Figure 13, then the data agree with the actual applied K_{max} values, Figure 14.

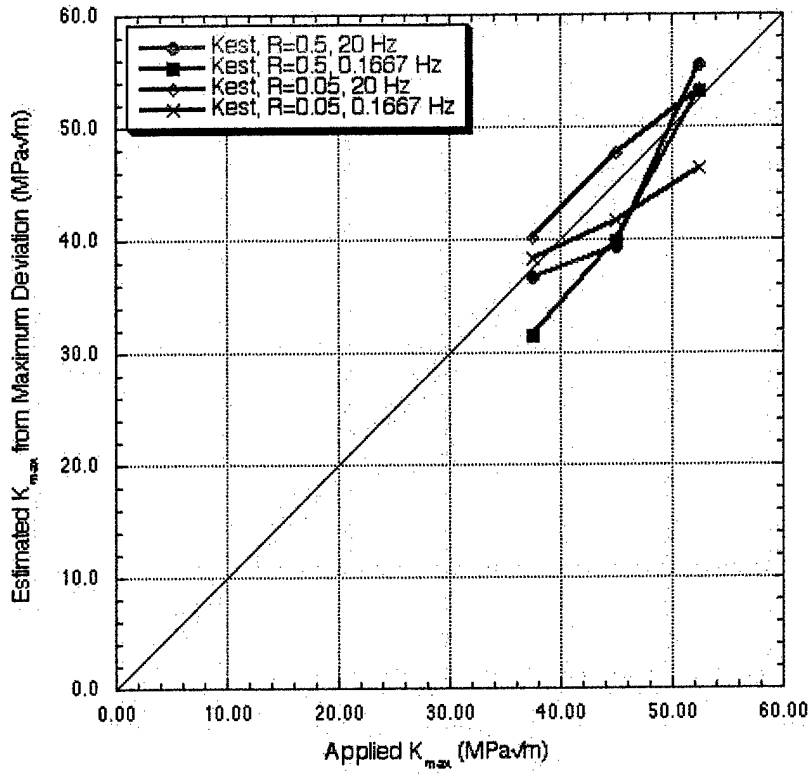

Figure 14. Estimated K_{max} as a function of applied K_{max} for four different loading conditions in IN100 specimens.

The results shown in Figure 14 suggest also that the deviation caused by the overloads and the deviation from the baseline fatigue loading are additive. Thus, an estimate of the magnitude of overload may be extractable from the fracture surfaces when the baseline fatigue loading parameters are known. Baseline fatigue loading parameters may be obtainable from fast Fourier transform analyses.

4.7 Summary of findings for IN100

1. Overloads produce a distinctive deviation profile when analyzed by FRASTA. Therefore, the occurrence of an overload in a mission spectrum may be determinable from the fracture surfaces.
2. The deviation measured on the fracture surfaces appears to be proportional to the degree the overload exceeds the baseline fatigue loading.

5 FINITE ELEMENT ANALYSIS OF CRACK TIP UNDER FATIGUE CYCLING WITH OVERLOADS

The stresses and strains that develop around a crack tip during fatigue cycling including overload were computed using the LSDYNA3D nonlinear finite element code. The analyses were performed quasistatically using implicit time integration.

Specimen geometry. We analyzed Test 97-100, a titanium alloy compact tension specimen as shown in Figure 15. The specimen was 5.0 cm wide, 4.8 cm high, and 1.0 cm thick. The holes for the loading pins were 1.0 cm in diameter. The notch in the specimen was 1.7 cm deep. The specimen was loaded by applying known displacement histories to the loading pins in order to achieve a specified stress intensity at the crack tip. These analyses were performed with the crack tip advanced 0.8 cm from the notch.

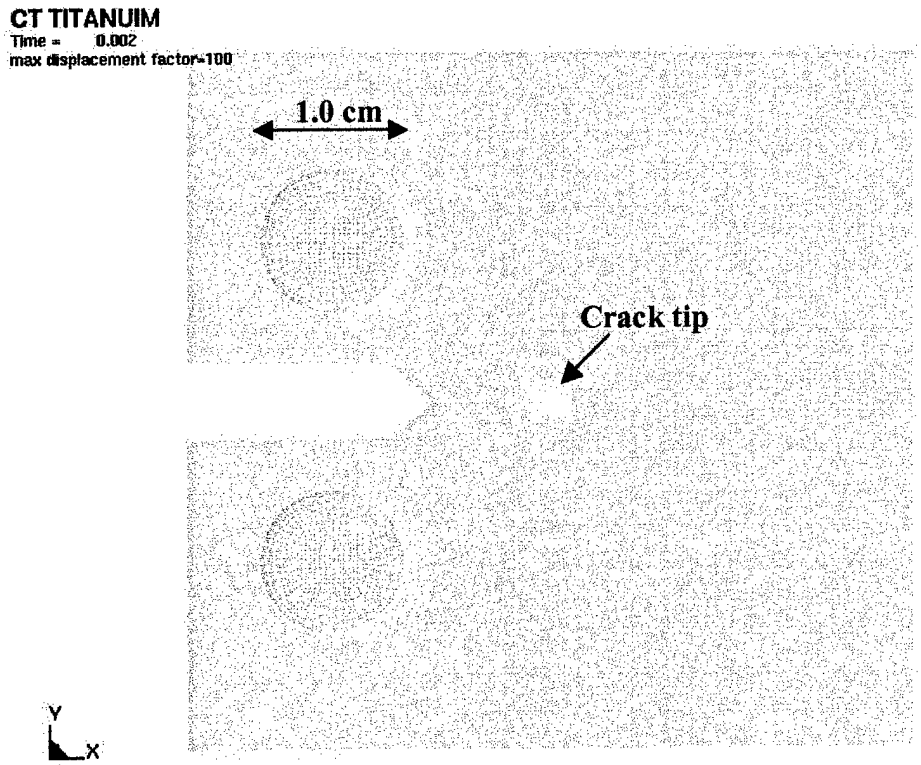

Figure 15. Finite element model of a compact tension specimen.

The mesh around the crack tip, as shown in Figure 16, was highly refined. The element dimension in the direction of crack advance was about 0.07 micron, which corresponds to the average crack extension per cycle measured for specimens loaded to 15 $MPa\sqrt{m}$ with R=0.05.

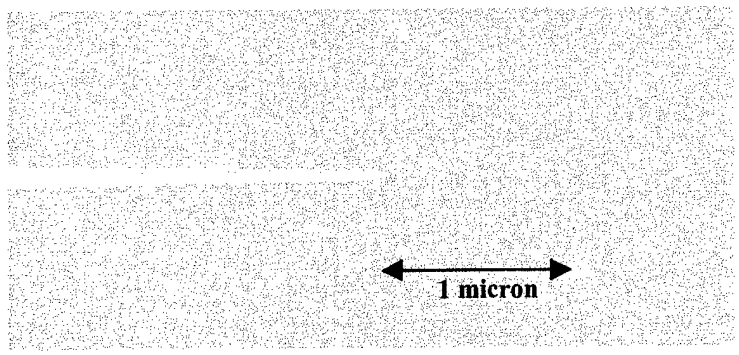

Figure 16. Fine mesh around the crack tip.

Load history and crack growth. The load history is shown in Figure 17. We applied 8 cycles of 15 MPa$\sqrt{m}$ followed by a single overload cycle of 22.5 MPa$\sqrt{m}$ and then a single cycle of 15 MPa$\sqrt{m}$.

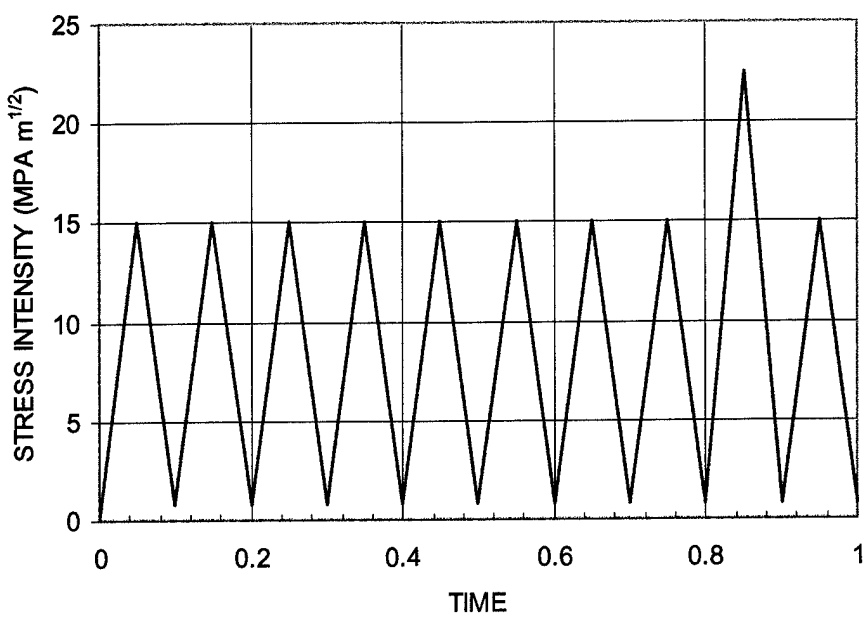

Figure 17. Cyclic loading history.

At the peak of each load cycle we grew the crack 0.07 microns by releasing the constraint that was holding together the nodes at the crack tip.

Material Model. The Ti-6Al-2Sn-4Zr-6Mo was assumed to follow power-law plasticity. The effective stress vs. effective strain curve is shown in Figure 18. Material constants are listed in Table 2.

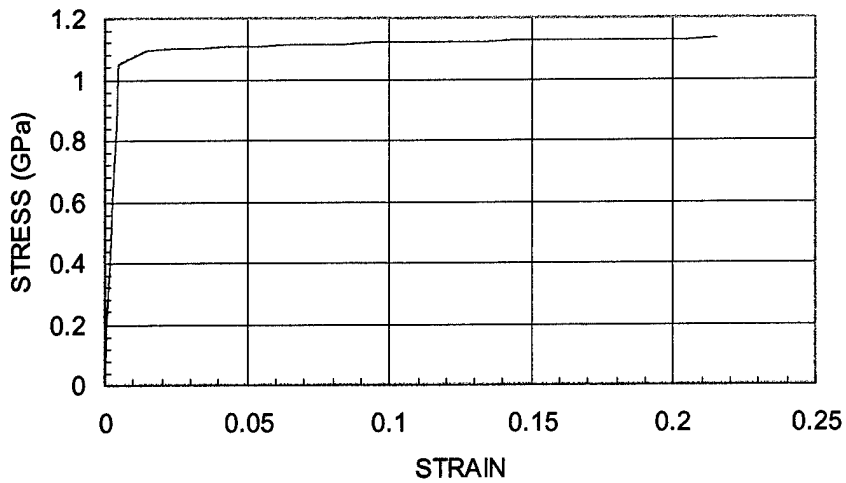

Figure 18. Power law model for Ti-6Al-2Sn-4Zr-6mo

TABLE 2. MATERIAL PROPERTIES FOR TITANIUM Ti-6Al-2Sn-4Zr-6Mo

Young's Modulus	E	210 GPa
Poisson's Ratio	ν	0.3
Stress Coefficient	k	1.16 GPa
Stress Exponent	n	0.015

Results. The calculated crack opening and development of the plastic zone around the crack tip are shown in Figure 19. The time refers to that in the loading curve shown in Figure 17. Figure 19d shows the plastic zone for the cycle before the overload. Plastic strains of over 0.8 are developed in a region of about 0.5 microns around the surface of the crack. Figure 19e shows the plastic zone for the overload cycle and Figure 19f shows the zone for the cycle following the overload.

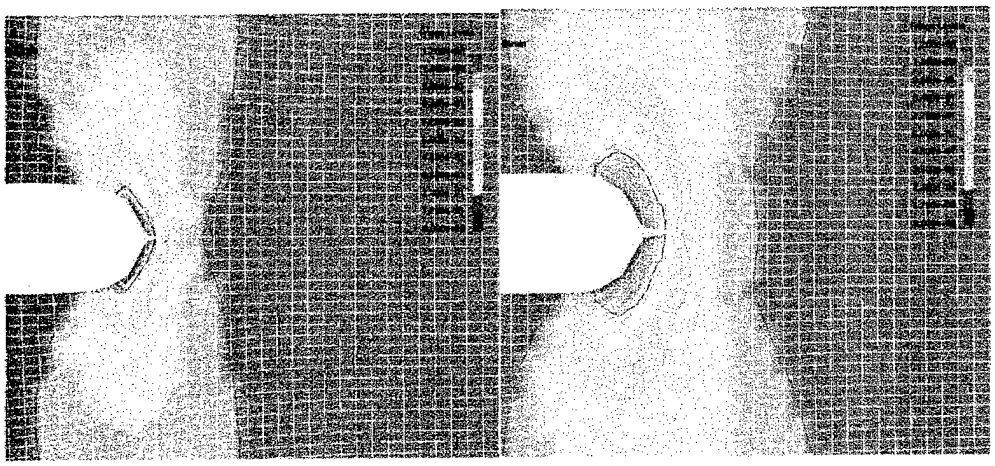

a) t=0.05 b) t=0.25

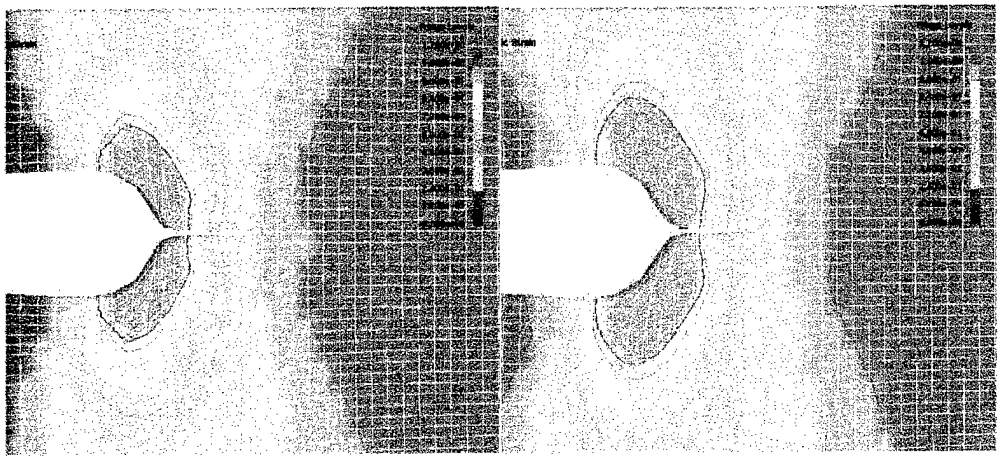

c) t=0.55 d) t=0.75

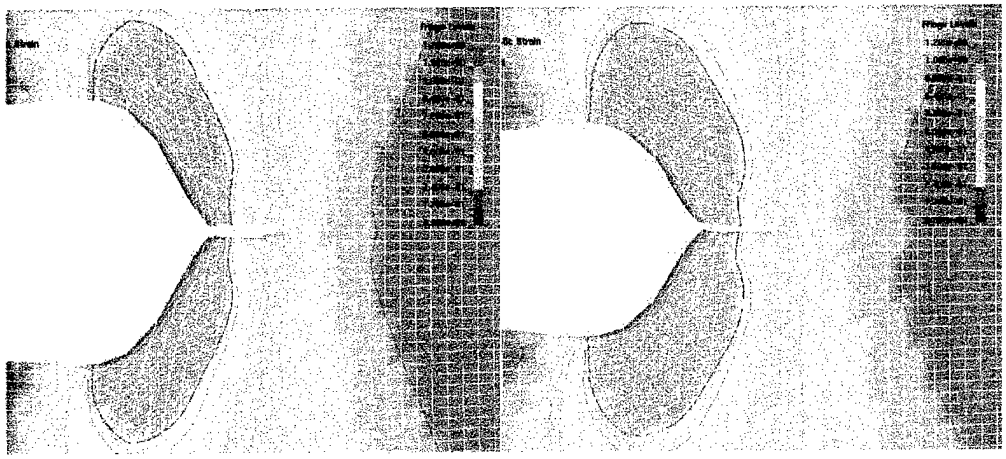

e) t=0.85 f) t=0.95

Figure 19. Calculated crack tip opening displacement and plastic zone.

Figure 20 shows the stress field at peak load for a stress intensity of 15 MPa$\sqrt{m}$ before and after the overload is applied. Before the overload shown in Figure 20a, a region of tension about 1 micron in diameter exists above about 3 GPa. After application of the overload, the stress ahead of the crack tip is reduced by about 20% from 3.8 GPa to 3.2 GPa. The diminished tensile field helps explain the effect of the overload in slowing crack advance.

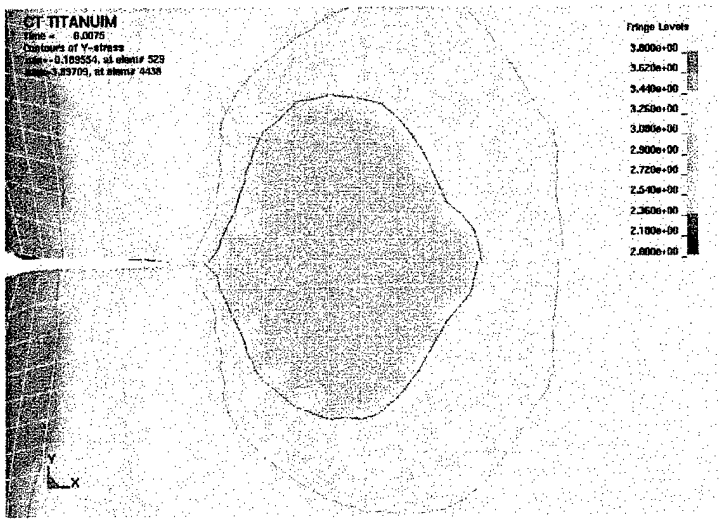

a) before the overload (t=0.75)

b) after the overload (t=0.95)

Figure 20. Calculated stress field around the crack tip.

These results show the feasibility of using high-resolution finite element analysis to investigate the process zone around the crack tip during fatigue crack growth with overloads. In the current analyses the crack tip was advanced by one element each

loading cycle. To improve the analysis, we would have the crack advance based on calculation of a damage parameter in the elements surrounding the crack tip. Such analyses could then be used to better understand some of the issues with the fractographic analyses, in particular:

1. What is the expected topography of a fracture surface in the region around overloads?
2. How does the conjugate surface separation relate to the number of cycles?
3. How is crack growth rate affected by overloads?

6. DISCUSSION

In this work we examined overloads from 1.25 to 1.75 times the baseline Kmax. As Sadananda et al [5] have pointed out after a review of the literature, overloads of less than 1.5 times the baseline have little effect on crack growth rate. Indeed, definite markings on the fracture surfaces were not detectable by scanning electron microscopy. Higher overloads would likely produce more readily measurable deformation markings and hence facilitate analyses. Higher overloads should be investigated in future work

The permanent (plastic) stretching at the crack tip caused by overloads in titanium and nickel alloys was measured by rejoining the conjugate fracture surface topographs. The influence zone of the overload was indicated by the deviation in the FPC (FRASTA-generated Fracture Progression Curve), which relates crack length to fracture surface displacement.

The FPC deviation for the titanium alloy was symmetric and bell-shaped, starting several hundred microns behind the crack tip, peaking about 250 µm in advance of the crack tip, and falling to zero 700 to 1500 µm beyond the crack tip. Thus, the influence of the overload is many times larger than the calculated plastic zone size (10 to 20 µm). Peak position was independent of overload magnitude, but the length of influence increased with overload magnitude.

Peak deviation varied linearly with Kmax when the R-value was low (0.05); (when the R-value was high (0.5), however, a relationship was not obvious), intersecting zero deviation at the baseline Kmax (See Figure 7) and suggesting that the deformation induced by overload is additive to the deformation caused by the baseline fatigue loading. A similar result was found for IN 100 (see Figures 13 and 14). These findings are consistent with observations reported in the literature [5].

The overload-induced deviation in the IN-100 specimens had a skewed-bell shape. The deviation increased steeply approximately 100 µm behind the crack tip, peaked about 100 µm ahead of the crack tip, and then decreased gradually. The shape and size differs from the titanium findings and could be attributed to material or testing condition. Although the high test temperature for IN100 (650°C) might induce creep, the skewed-bell shape was common for tests at 20 Hz and 0.1667 Hz. Thus, the material factor may be more dominant. Further investigation is needed to determine what material properties govern crack propagation through the plastic deformation zone.

Figure 21 shows crack opening displacement as a function of number of cycles computed by the finite element method. After the third cycle the crack face opening increases linearly with cycle number. During these cycles, the crack extends a fixed distance per cycle, supporting the FRASTA procedure of separating the conjugate surfaces at a constant rate.

In its present state, the FRASTA method cannot determine the crack propagation rate through an overload region. The relation between displacement and time is required. We

often observed that the fracture progression curve (FPC) relating fractured area (crack length) to conjugate fracture surface displacement is linear until an overload is applied, and is linear again with the same slope after a certain additional displacement. This suggests that the crack growth rate is constant (and in fact equal) before and after the overload. If the fatigue test can be assumed to have been conducted at a constant displacement rate, i.e., displacement increases linearly with time, then the FPC indicates the crack growth rate.

The FPC deviation extends a substantial distance beyond the location of overload application, suggesting that crack growth is affected well after the crack front has emerged from the plastic zone calculated by Eq. 1. Existing treatments of crack growth retardation predict that growth rates return to normal after the plastic zone is traversed [3,4].

The ability to determine the extent of retardation or acceleration of crack growth caused by an overload would be an important accomplishment. Development of such an ability, however, requires further thought and analysis.

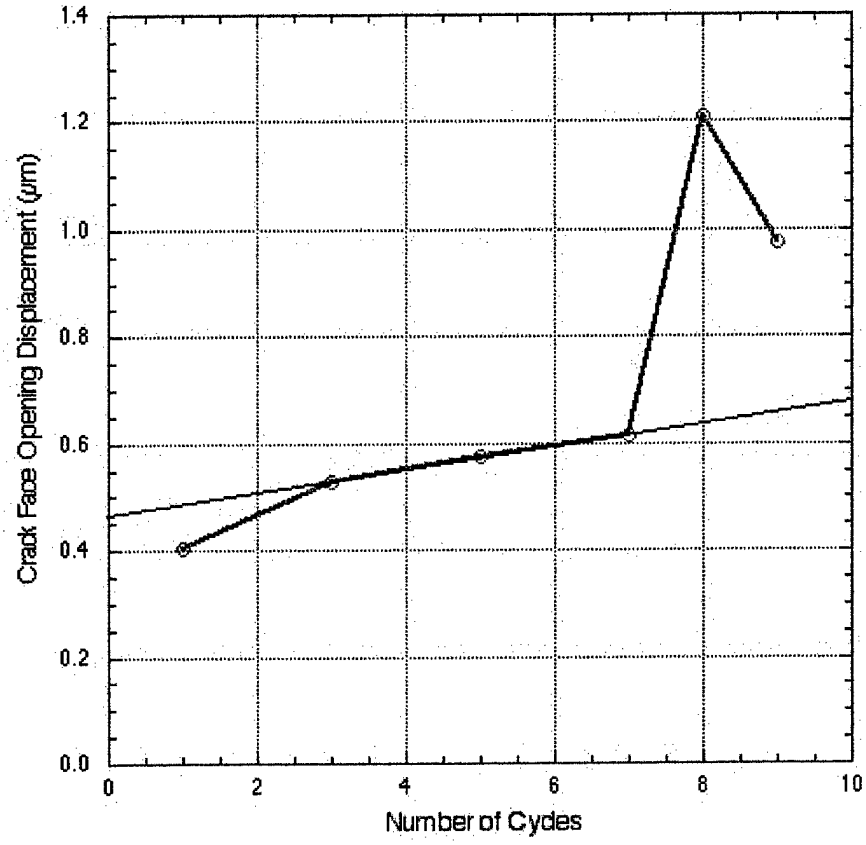

Figure 21. Crack face opening displacement as a function of number of cycles calculated by the finite element method.

REFERENCES

1. P.C. Paris, M.P. Gomez, and W.P. Anderson; "A Rational Analytic Theory of Fatigue," *The Trend in Engineering*, Vol. 13, 1961, pp. 9-14; P.C. Paris and F. Erdogan, "A Critical Analysis of Crack Propagation Laws," *Journal of Basic Engineering*, Vol. 85, pp. 528-534 (1960).
2. International Conference on Fatigue Damage
3. J. Willenborg, R.M. Engle, and H.A. Wood, "A Crack Growth Retardation Model Using an Effective Stress Concept," Technical Memorandum 71-1-FBR 7784 to the Air Force Flight Dynamics Laboratory (January 1971).
4. O.E. Wheeler, "Spectrum Loading and Crack Growth," Transactions of the ASME (March 1972).
5. K. Sadananda, A.K. Vasudevan, R.L. Holtz, and E.U. Lee; "Analysis of Overload Effects and Related Phenomena" *International Journal of Fatigue* Vol. 21 pp S233-S246 (1999).
6. R.H. VanStone and D.C. Slavik, "Prediction of Time-Dependent Crack Growth with Retardation Effects in Nickel Based Alloys, Fatigue and Fracture Mechanics," **31**, ASTM STP 1289, ASTM, pp. 405-426 (2000).
7. T. Kobayashi and D. A. Shockey, "FRASTA: A New Way to Analyze Fracture Surfaces, Part 1: Reconstructing Crack Histories," Advanced Materials & Processes, 140 (5), 28-34 (1991).
8 T. Kobayashi and D. A. Shockey, "Fracture Analysis Via FRASTA, Part 2: Determining Fracture Mechanisms and Parameters," Advanced Materials & Processes, 140 (6), 24-32 (1991).
9. Livermore Software Technology Corp., website http://www.lstc.com
10. Cornell Fracture Group website, http://www.cfg.cornell.edu/software/FRANC2D.html

APPENDICES

APPENDIX I: TOPOGRAPHIC DATA FROM FRACTURE SURFACES NEAR OVERLOAD SITES AND RESULTS OF ANALYSES

Areas of fracture surfaces where overloads had been applied were examined by scanning electron microscopy. Their topographies were quantified, and the topographic data were analyzed with the FRASTA technique. This appendix describes the data acquisition and analysis procedures, and presents the results for each fracture surface.

Fracture surfaces were provided by AFRL personnel performed a series of fatigue tests on compact tension specimens fabricated from Ti-6Al-2Sn-4Zr-6Mo and IN100 plates. During each test single cycle overloads of different magnitudes were applied after a certain amount of crack growth.

The topographies of fracture surface areas around overloads were quantified by scanning laser confocal optics microscopy. Topographs of conjugate fracture surfaces were juxtaposed and positioned relative to each other to simulate the configuration of the crack faces during the fatigue tests. Crack growth was simulated by displacing the conjugate topographs. The progress of a fatigue crack is shown in fracture area projection plots or in cross section plots.

For each specimen a series of fractured area projection plots (FAPPs) was produced and superimposed on the scanning electron microscope photograph of fracture surfaces. These FAPP-superimposed photographs illustrate details of the crack front movement in the plastic zone. The cross-sectional plots (XSPs) show changes in the crack tip opening displacement and opening angles. The fractured area increase as a function of conjugate surface spacing, i.e. the fracture progression curve (FPC), delineates the effect of overload and underload as a degree of deviation from a straight line. The procedure is known as FRASTA (Fracture Surface Topography Analysis) and is described in detail in references 7 and 8.

The disruptive effect of an overload on the otherwise steady crack growth rate is shown in fracture progression plots obtained by computing crack length (relative FAPP areas) and converting topograph displacement to plastic opening displacement. Deviation from the linear steady state relation indicates the size of the stretch zone, how much the crack has slowed, and the linear extent of the overload influence.

We applied the FRASTA technique to all areas of the fracture surfaces where an overload was applied.

Two materials were examined—a titanium alloy (Ti-6Al-2Sn-4Zr-6Mo) and IN100, a nickel base superalloy—and two specimens of each material were analyzed. The baseline stress intensity, stress ratio, and overload magnitude were varied. In all, nine load conditions for the titanium alloy and seven conditions for the IN100 alloy were evaluated. The results for each load condition are presented as an SEM photo, a gray area

representation of the fracture surface topography, a FRASTA simulation of crack growth, a plot representing crack growth history, and a profile of the crack blunting caused by the overload.

1.Titanium Alloy (Ti-6Al-2Sn-4Zr-6Mo) Properties and Test Conditions

TABLE AI-1. MECHANICAL PROPERTIES OF Ti-6Al-2Sn-4Zr-6Mo AT ROOM TEMPERATURE.

Modulus of Elasticity, E, (Gpa)	210
0.2 % Yield Strength , $\sigma_{0.2}$, (MPa)	1158
Ultimate Strength, σ_{UTS}, (MPa)	1232
Elongation (%)	10.9
Fracture Toughness, K_{IC}, (MPa√m)	29

Two fatigue tests in which the load conditions were varied systematically were selected for analysis. One test was conducted at a baseline stress intensity of 15 MPa√m, a baseline frequency of 20 Hz, and a stress ratio (R) of 0.05. The second test was conducted at a stress ratio of 0.5. In each test three magnitudes of single cycle overloads were applied after several mm of crack growth so that effects of individual overloads were clearly separable from later overloads. The fatigue loading conditions for the two specimens are given in Tables AI-2 and AI-3.

TABLE AI-2. TEST CONDITIONS FOR Ti-ALLOY SPECIMEN NO. 97-100 (R = 0.05).

Load Status	Temp (°C)	Kmax (MPa√m)	Kmin (MPa√m)	R	Freq (Hz)	Number of Cycles	Crack Length (mm)
Baseline	23	15.00	0.75	0.05	20	47871	9.8859
1.25 OL	23	18.75	0.75	0.04	na	77712	12.1379
Baseline	23	15.00	0.75	0.05	20	77713	12.1379
1.375 OL	23	20.625	0.75	0.03636	na	126800	16.0069
Baseline	23	15.00	0.75	0.05	20	126801	16.0069
1.50 OL	23	22.50	0.75	0.03333	na	179256	19.9314
Baseline	23	15.00	0.75	0.05	20	179257	19.9314
Specimen Rupture	23					205612	21.9249

TABLE AI-3. TEST CONDITIONS FOR TI-ALLOY SPECIMEN NO. 97-101
(R = 0.50)

Load Status	Temp (°C)	Kmax (MPa√m)	Kmin (MPa√m)	R	Freq (Hz)	Number of Cycles	Crack Length (mm)
Baseline	23	15.00	7.50	0.50	20	125185	11.201
1.25 OL	23	18.75	7.50	0.40	na	234150	13.059
Baseline	23	15.00	7.50	0.50	20	234151	13.059
1.375 OL	23	20.625	7.50	0.3636	na	471400	17.181
Baseline	23	15.00	7.50	0.50	20	471401	17.181
1.50 OL	23	22.50	7.50	0.3333	na	700380	20.974
Baseline	23	15.00	7.50	0.50	20	700381	20.974
1.25 OL	23	18.75	7.50	0.40	na	946811	24.921
Baseline	23	15.00	7.50	0.50	20	946812	24.921
1.50 OL	23	22.50	7.50	0.3333	na	1192400	28.8795
Baseline	23	15.00	7.50	0.50	20	1192401	28.8795
Baseline with Low R	23	15.00	0.75	0.05	na	1315234	30.699
1.50 OL	23	22.50	0.75	0.0333 3	na	1347617	32.869
Baseline with Low R	23	15.00	0.75	0.05	20	1347618	32.869
Specimen Rupture	23					1376866	-

Crack length versus number of cycles for the two specimens is plotted in Figure AI-1. The relationship is nearly linear, suggesting that the applied overloads did not significantly influence crack growth rate. The failure surfaces also showed no evidence of a change in crack growth rate.

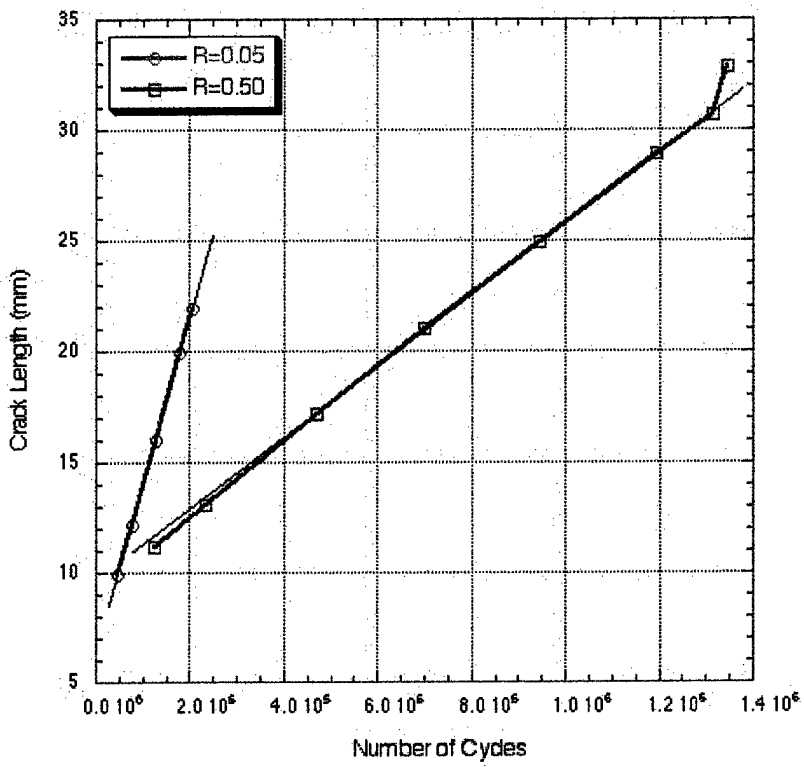

Figure AI-1. Crack length vs. number of cycles for two specimens that experienced several single-cycle overloads.

Specimen 97-100 was cyclically loaded at a baseline stress intensity of 15 MPa√m, a stress intensity ratio (R) of 0.05, and a frequency of 20 Hz. Overloads of 18.75, 20.63, and 22.50 MPa√m, corresponding to 1.25, 1.375, and 1.5 times the baseline stress intensity, respectively, were applied after several mm of crack growth.

2. Fracture Surface Analysis Results

Ti-alloy, R=0.05, freq=20 Hz, baseline K_{max}=15 MPa√m, overload Kmax=18.75 MPa√m (1.25 times the baseline stress intensity).

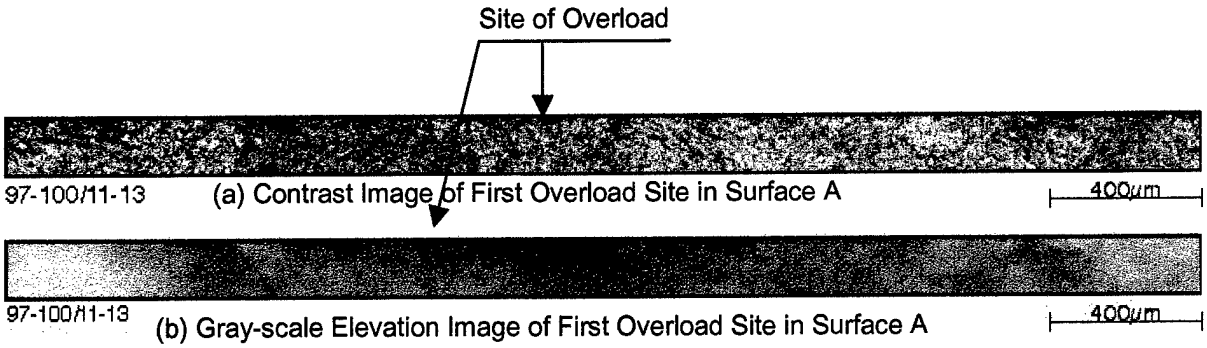

Figure AI-2. Contrast and gray-scale elevation images of fracture surface area surrounding overload site.

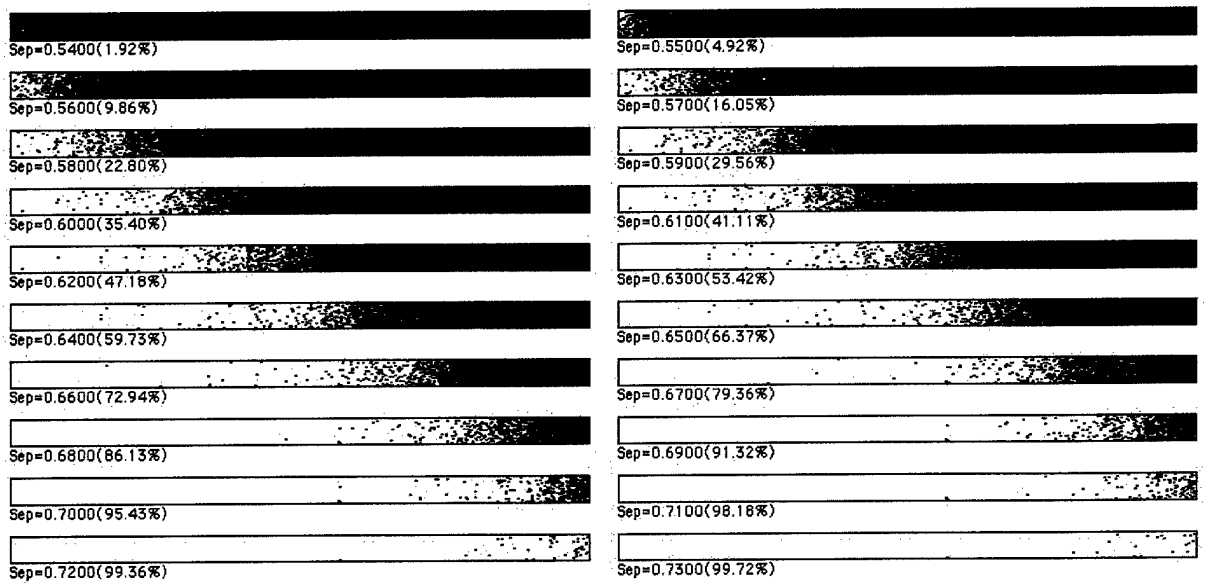

Figure AI-3. Fractured area projection plots (FAPPs) indicating the progression of the crack front.

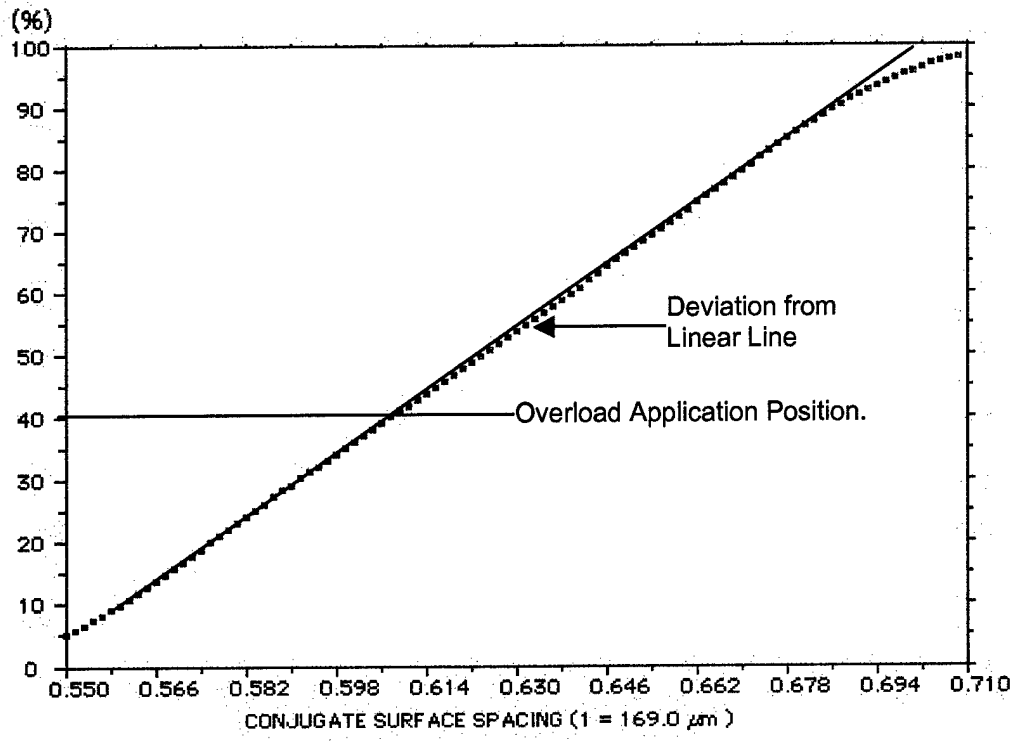

Figure AI-4. Increase in fractured area with increased spacing of the conjugate topographs.

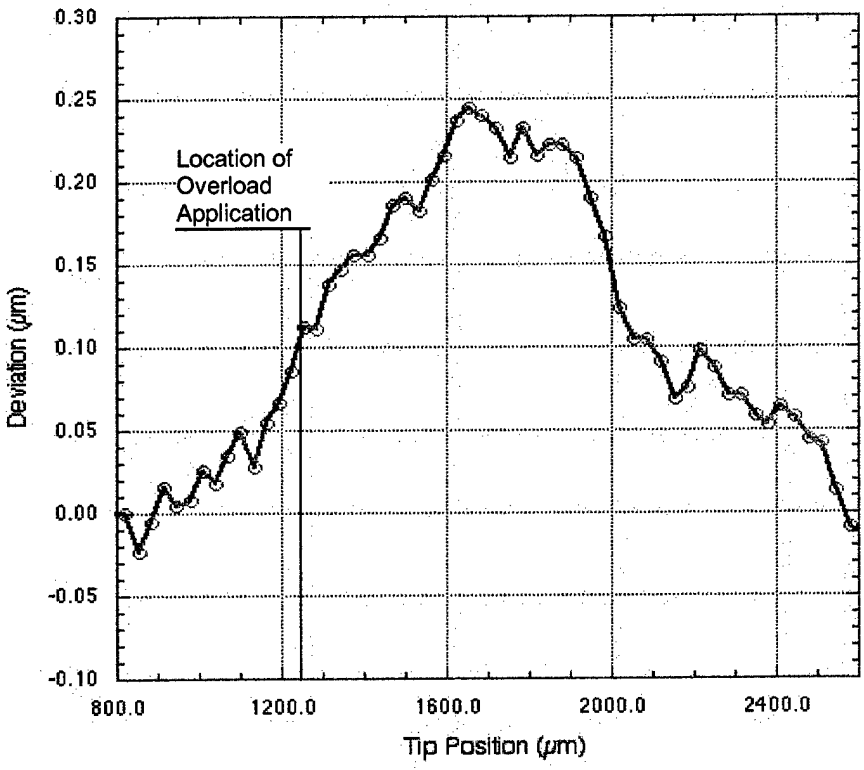

Figure AI-5. Deformation profile of the crack front in the vicinity of overload application.

Ti-alloy, R=0.05, freq=20 Hz, baseline K_{max}=15 MPa√m, overload Kmax=20.63 MPa√m (1.375 times the baseline stress intensity).

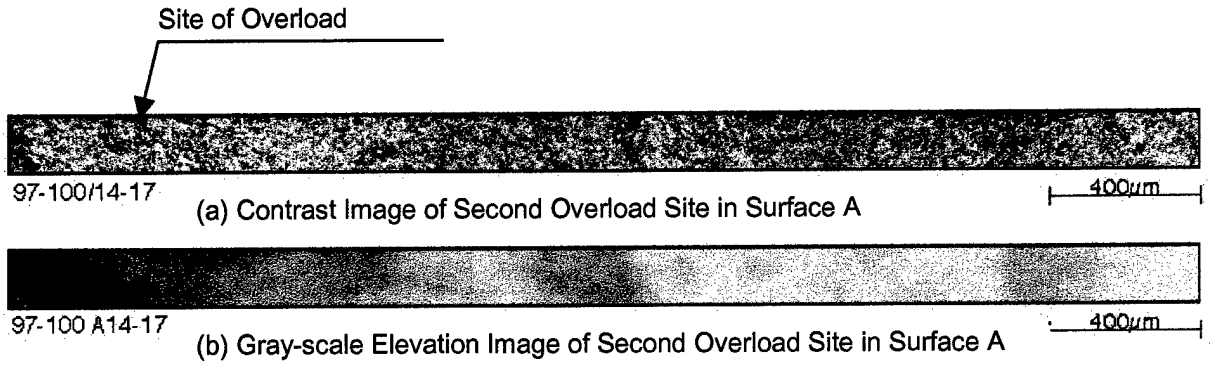

Figure AI-6. Contrast and gray-scale elevation images of fracture surface area surrounding overload site.

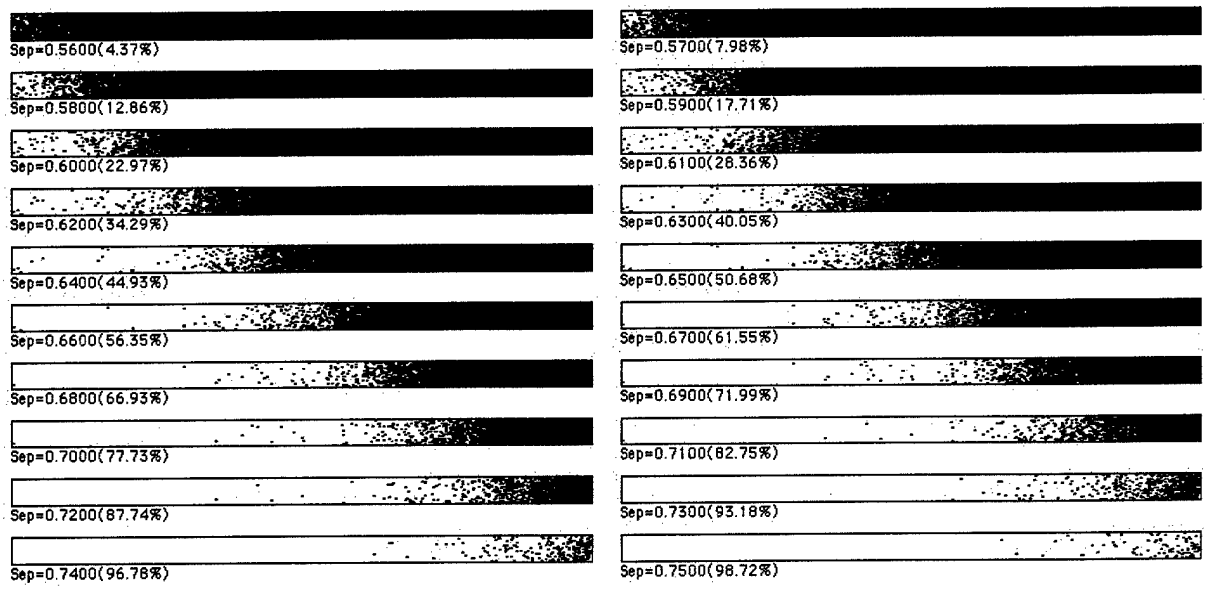

Figure AI-7. Fractured area projection plots (FAPPs) indicating the progression of the crack front.

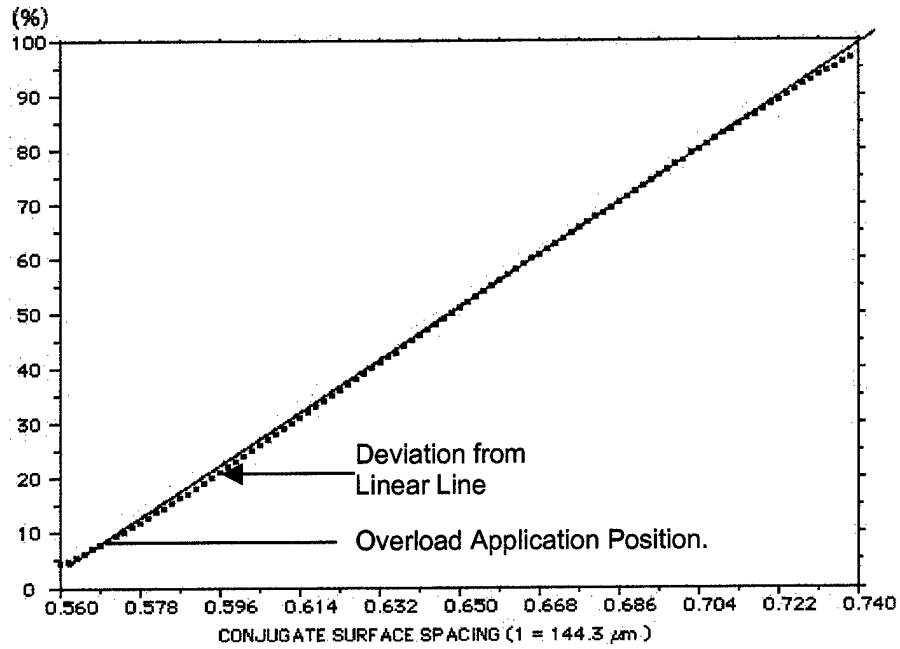

Figure AI-8. Increase in fractured area with increased spacing of the conjugate topographs.

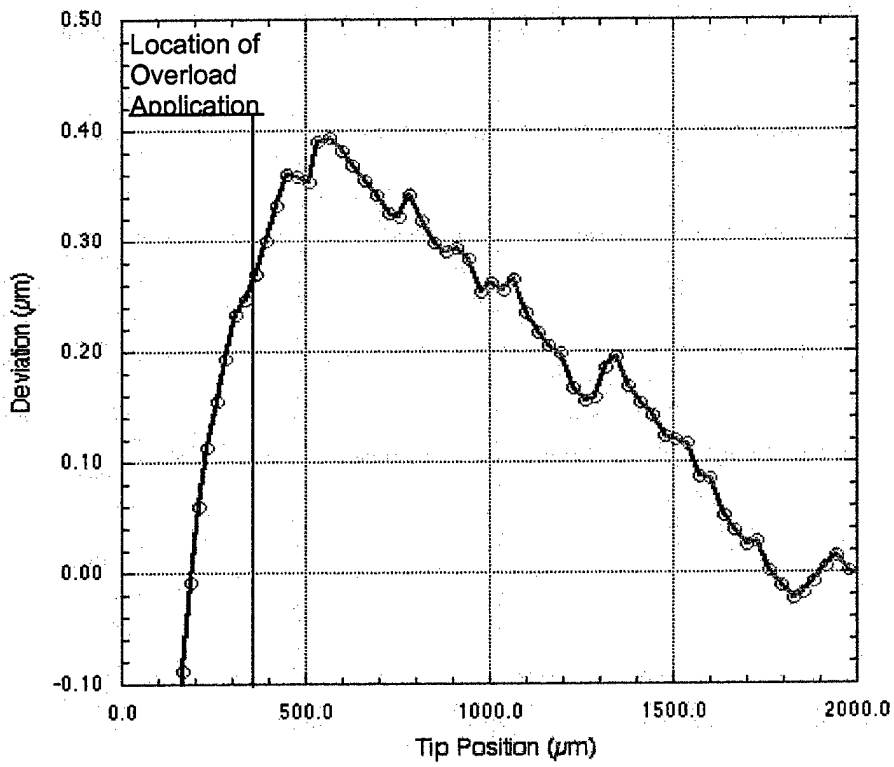

Figure AI-9. Deformation profile of the crack front in the vicinity of overload application.

Ti-alloy, R=0.05, freq=20 Hz, baseline K_{max}=15 MPa√m, overload Kmax=22.50 MPa√m (1.50 times the baseline stress intensity).

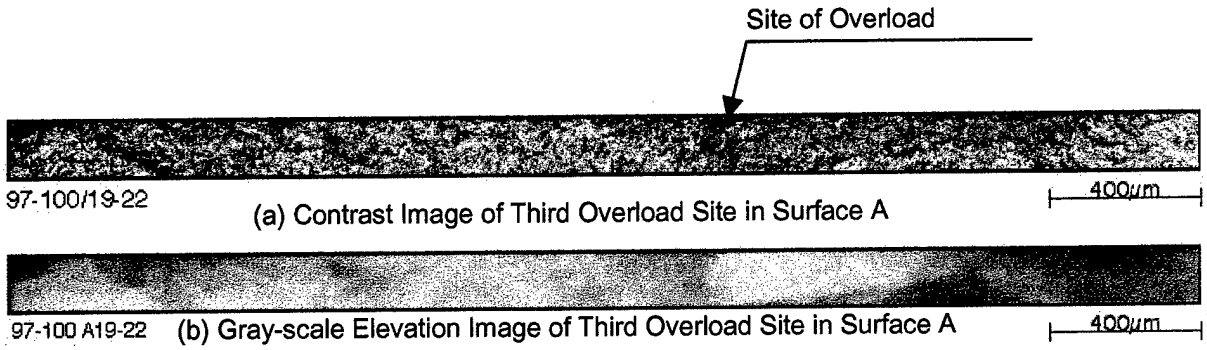

Figure AI-10. Contrast and gray-scale elevation images of fracture surface area surrounding overload site.

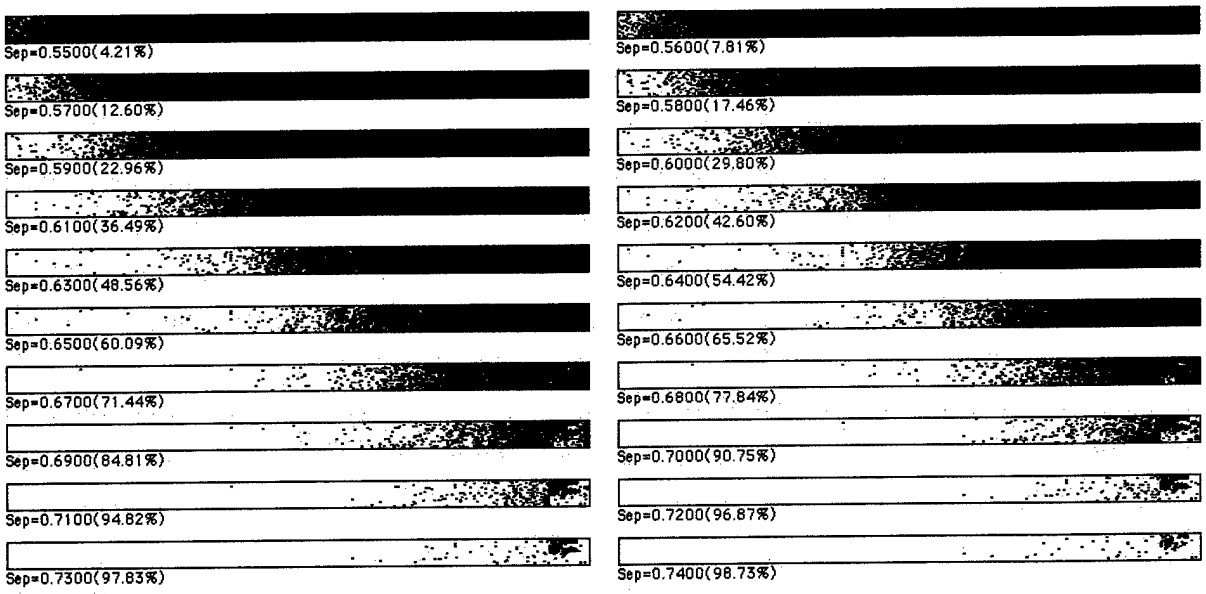

Figure AI-11. Fractured area projection plots (FAPPs) indicating the progression of the crack front.

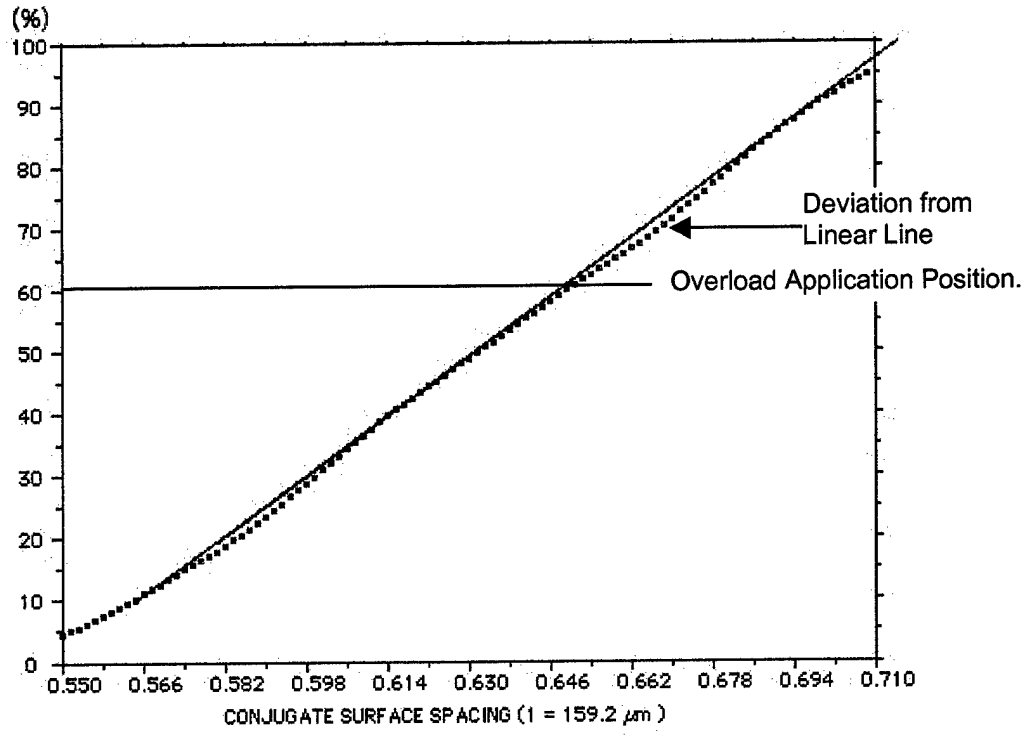

Figure AI-12. Increase in fractured area with increased spacing of the conjugate topographs.

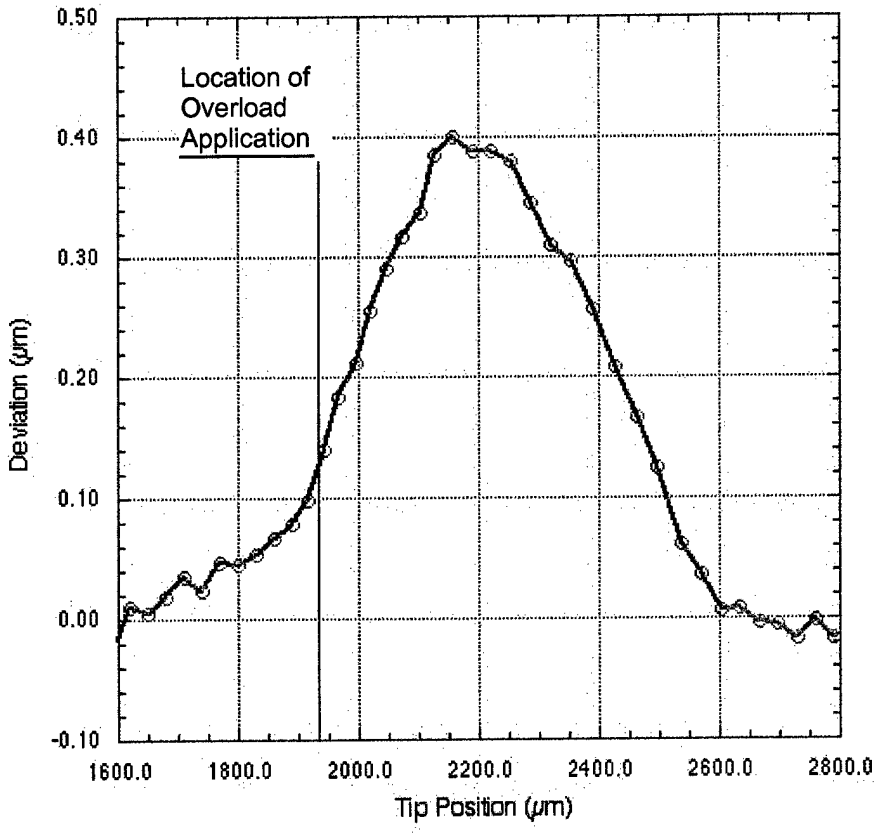

Figure AI-13. Deformation profile of the crack front in the vicinity of overload application.

Specimen 97-101 was cyclically loaded under the same conditions as Specimen 97-100, except at a stress intensity ratio (R) of 0.50. The baseline stress intensity was 15 MPa√m, the frequency was 20 Hz, and the overloads were 18.75, 20.63, and 22.50 MPa√m, corresponding to 1.25, 1.375, and 1.5 times the baseline stress intensity, respectively. The 1.25 and 1.50 overloads were applied twice, and the 1.50 overload was applied a third time with a stress ratio of 0.05 (see Table AI-3).

Ti-alloy, R=0.5, freq=20 Hz, baseline K_{max}=15 MPa√m, overload Kmax=18.75 MPa√m (1.25 times the baseline stress intensity).

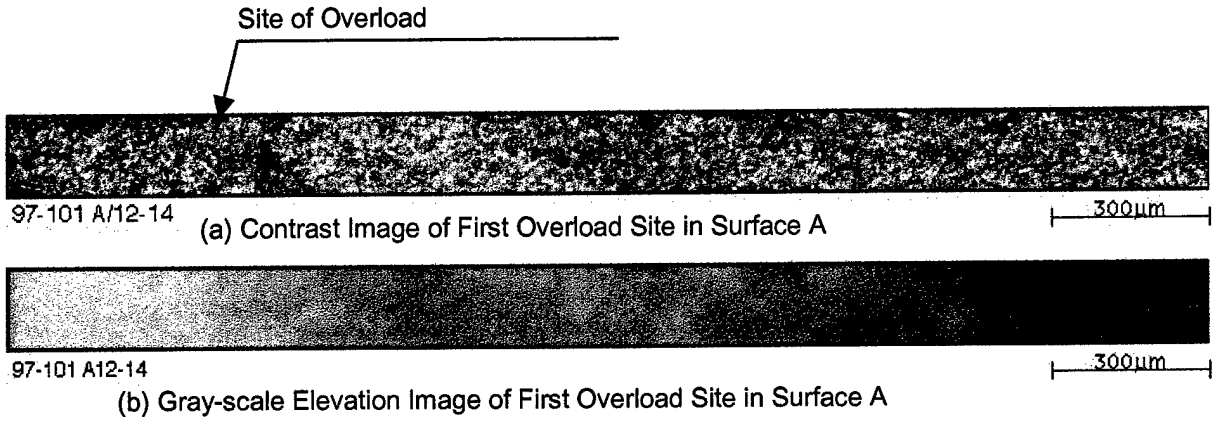

(a) Contrast Image of First Overload Site in Surface A

(b) Gray-scale Elevation Image of First Overload Site in Surface A

Figure AI-14. Contrast and gray-scale elevation images of fracture surface area surrounding overload site.

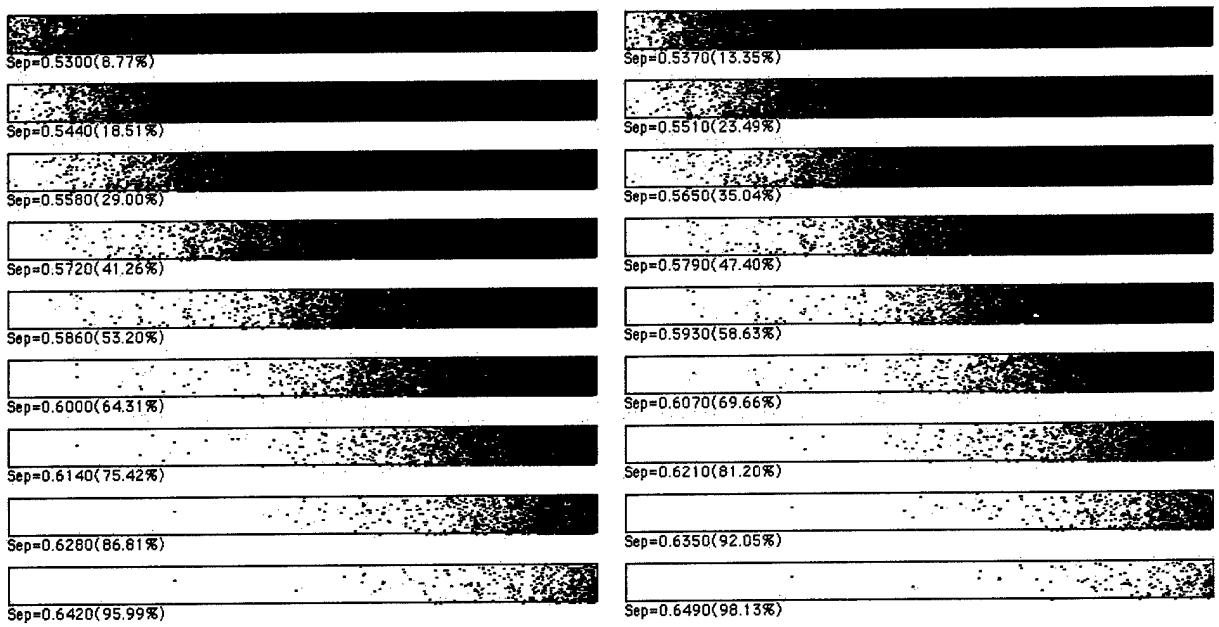

Figure AI-15. Fractured area projection plots (FAPPs) indicating the progression of the crack front.

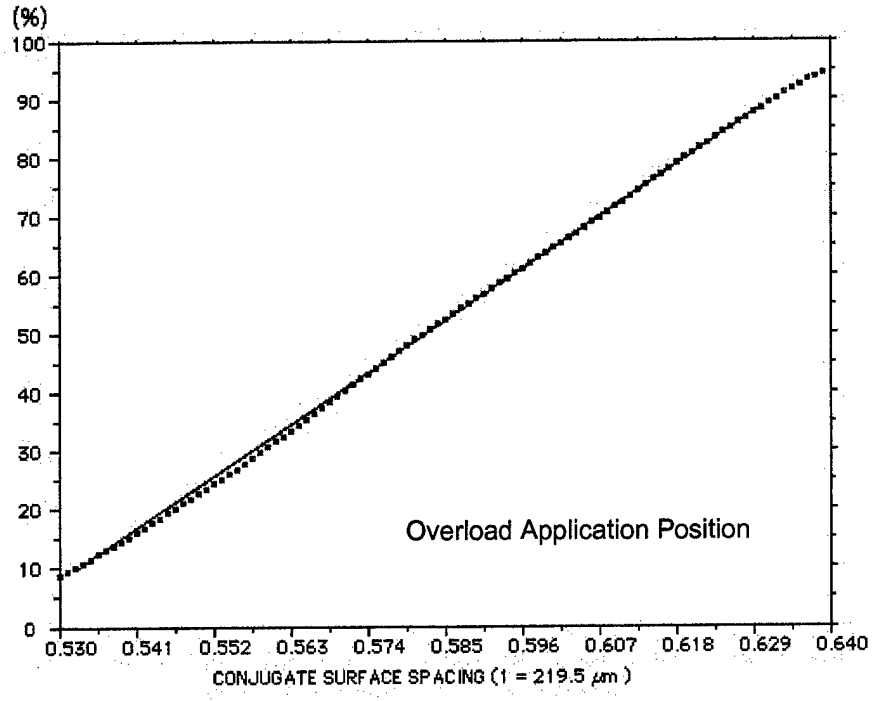

Figure AI-16. Increase in fractured area with increased spacing of the conjugate topographs.

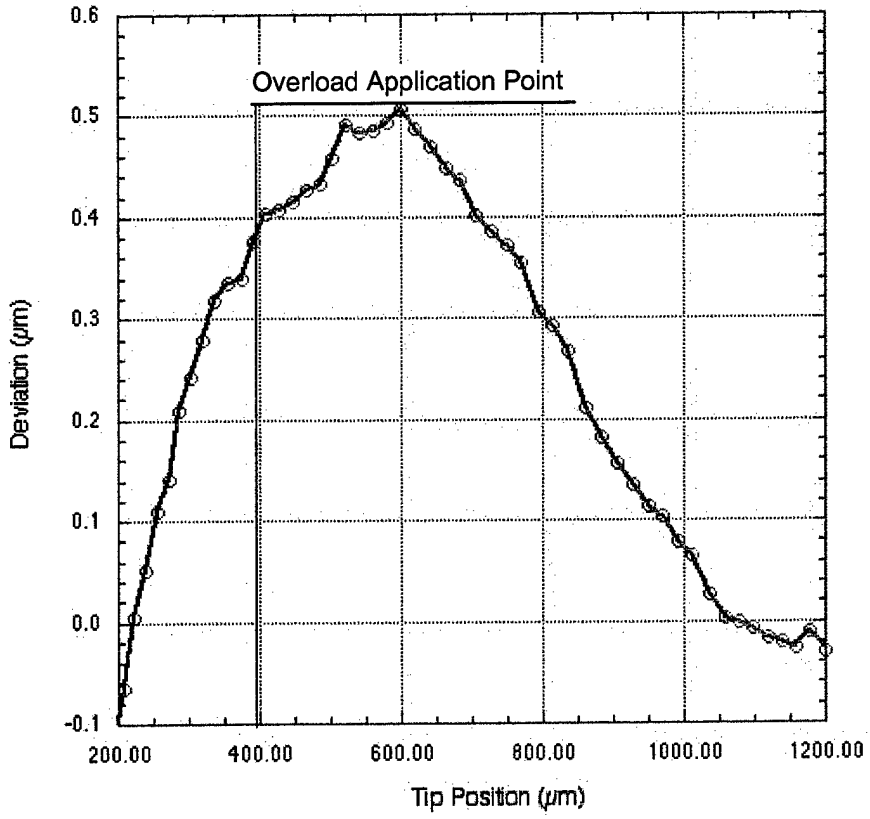

Figure AI-17. Deformation profile of the crack front in the vicinity of overload application.

Ti-alloy, R=0.5, freq=20 Hz, baseline K_{max}=15 MPa√m, overload Kmax=20.63 MPa√m (1.375 times the baseline stress intensity).

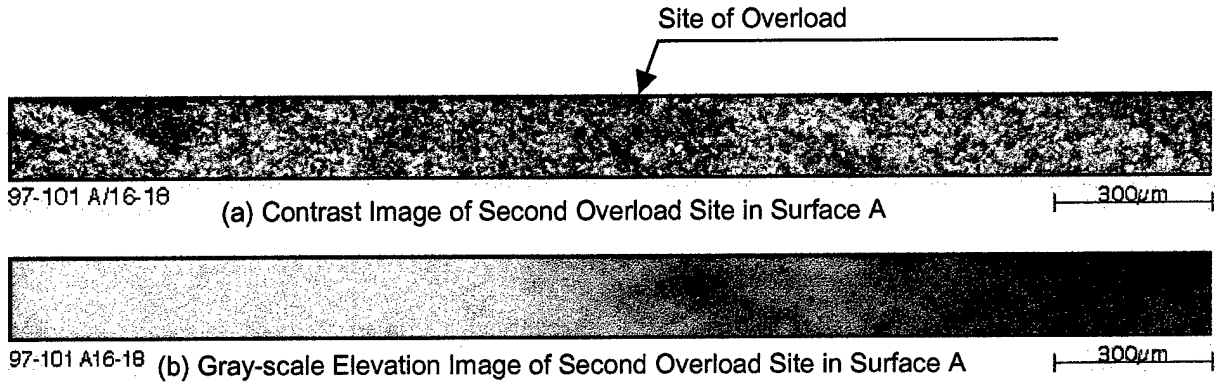

Figure AI-18. Contrast and gray-scale elevation images of fracture surface area surrounding overload site.

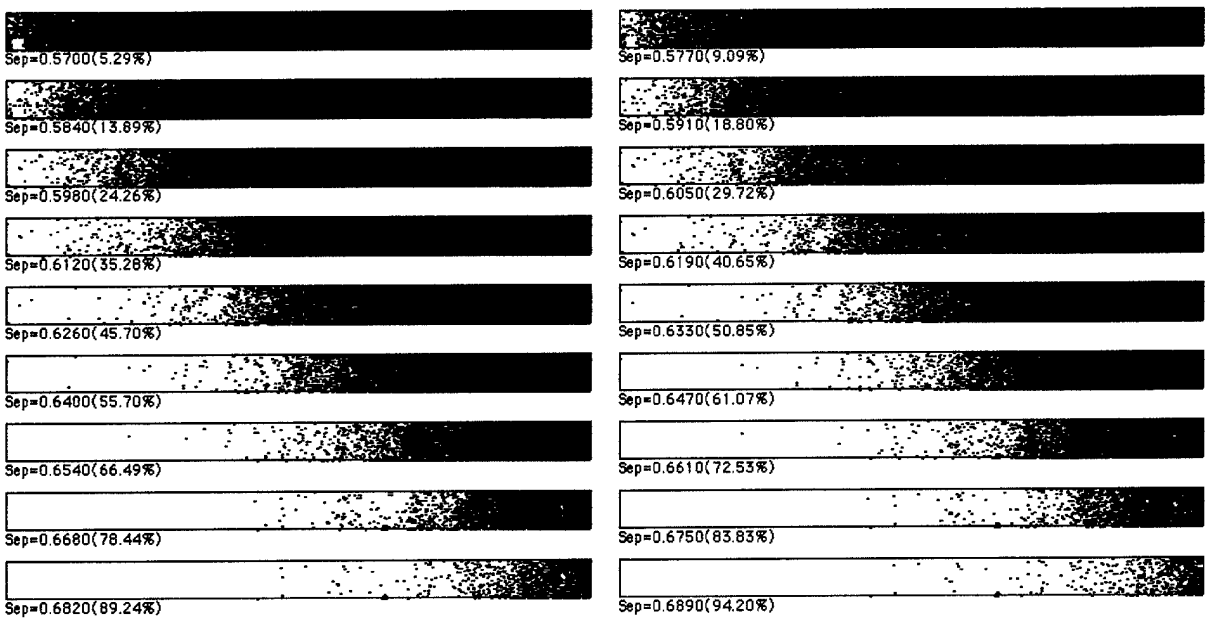

Figure AI-19. Fractured area projection plots (FAPPs) indicating the progression of the crack front.

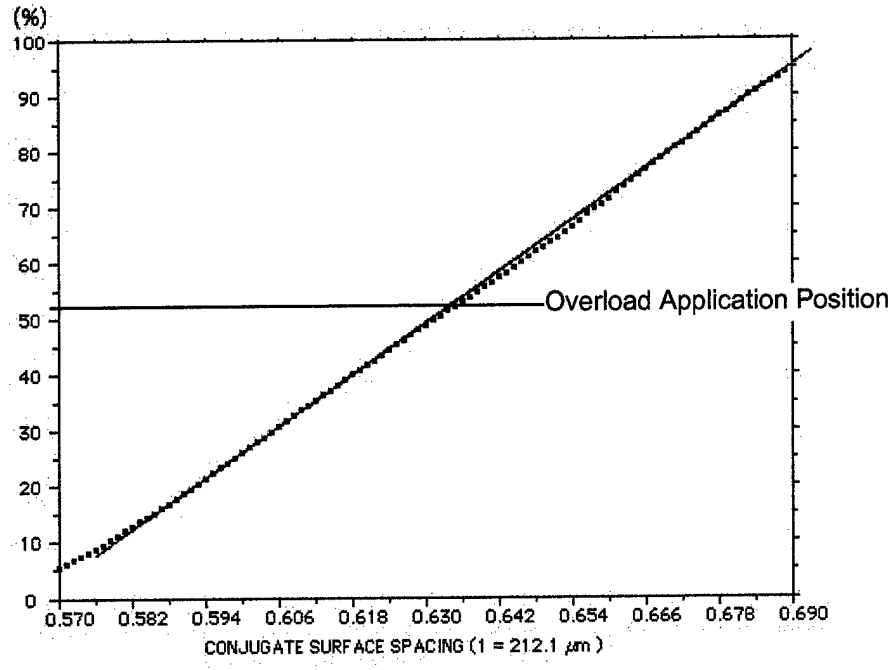

Figure AI-20. Increase in fractured area with increased spacing of the conjugate topographs.

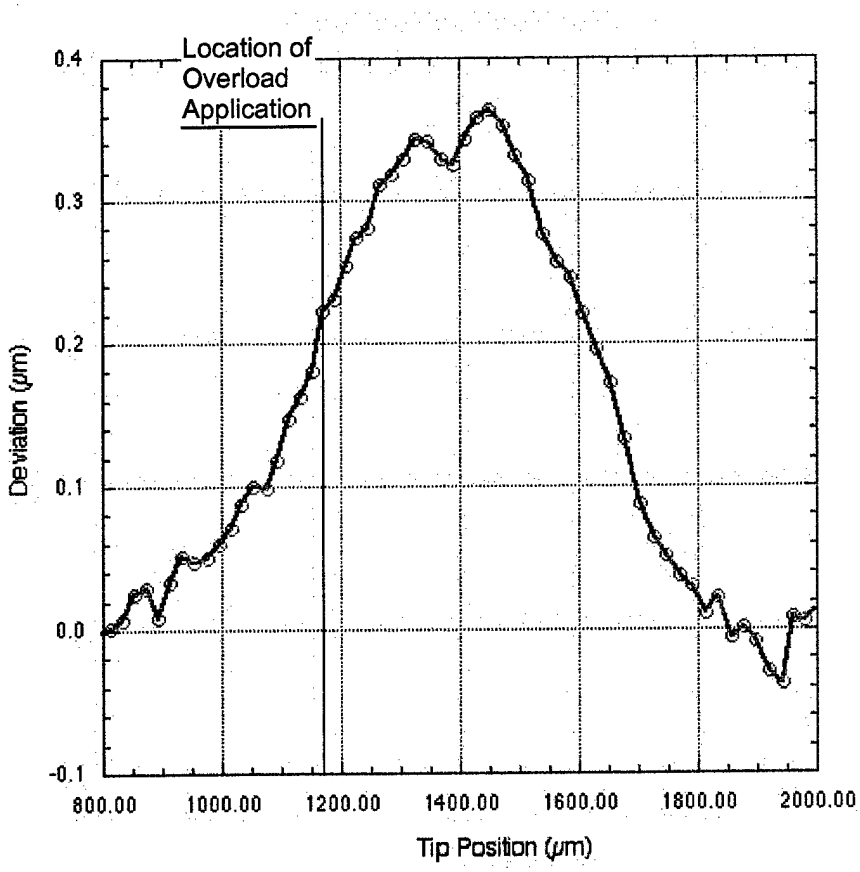

Figure AI-21. Deformation profile of the crack front in the vicinity of overload application.

Ti-alloy, R=0.5, freq=20 Hz, baseline K_{max}=15 MPa√m, overload Kmax=22.50 MPa√m (1.50 times the baseline stress intensity).

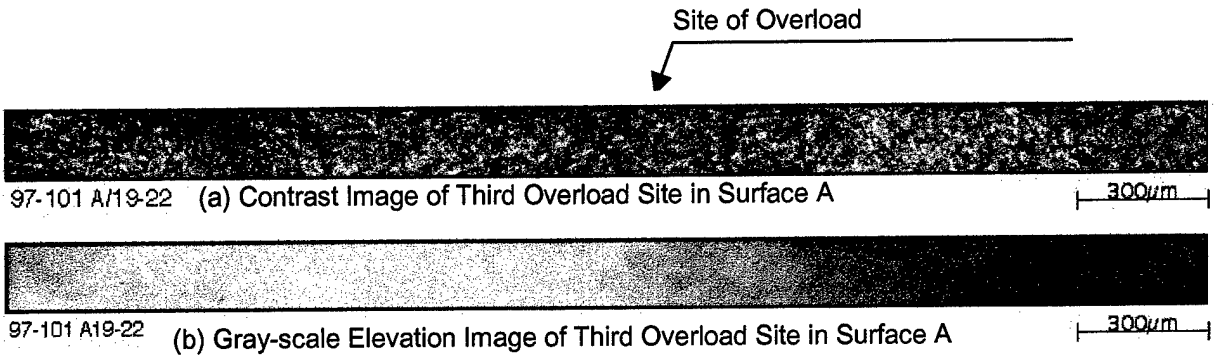

Figure AI-22. Contrast and gray-scale elevation images of fracture surface area surrounding overload site.

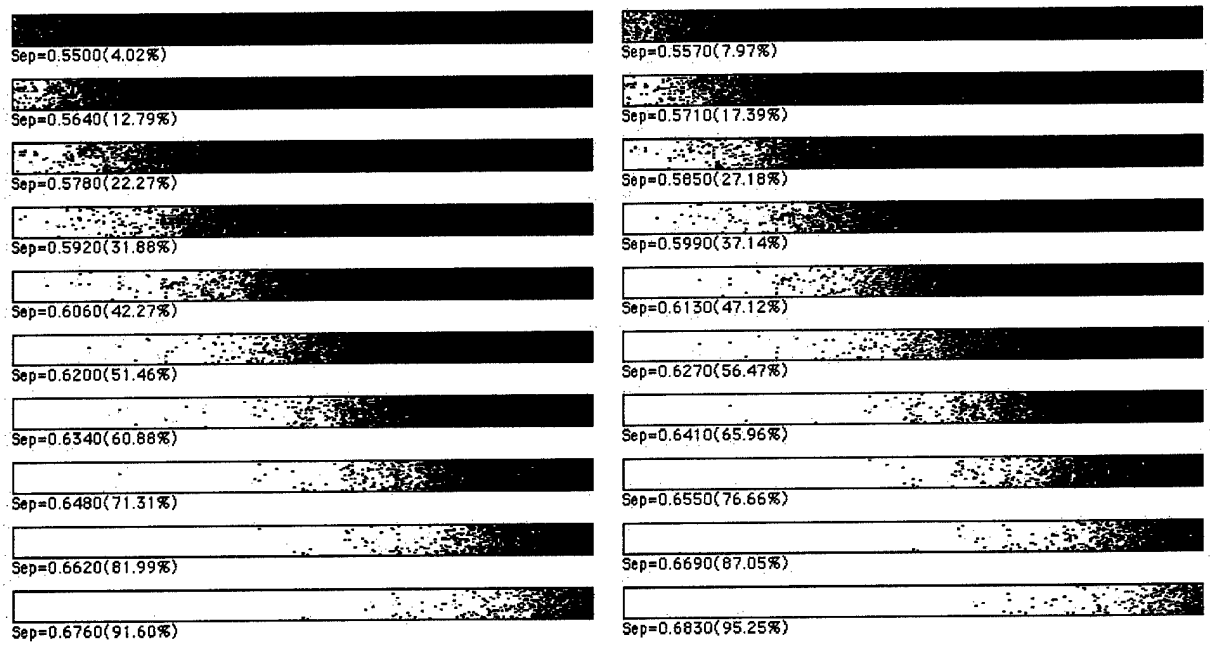

Figure AI-23. Fractured area projection plots (FAPPs) indicating the progression of the crack front.

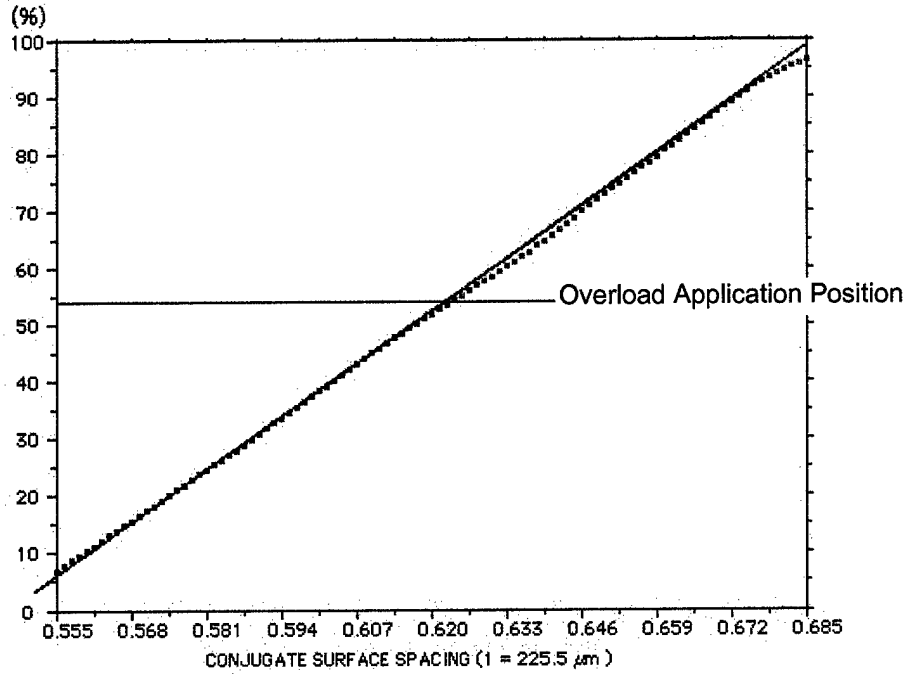

Figure AI-24. Increase in fractured area with increased spacing of the conjugate topographs.

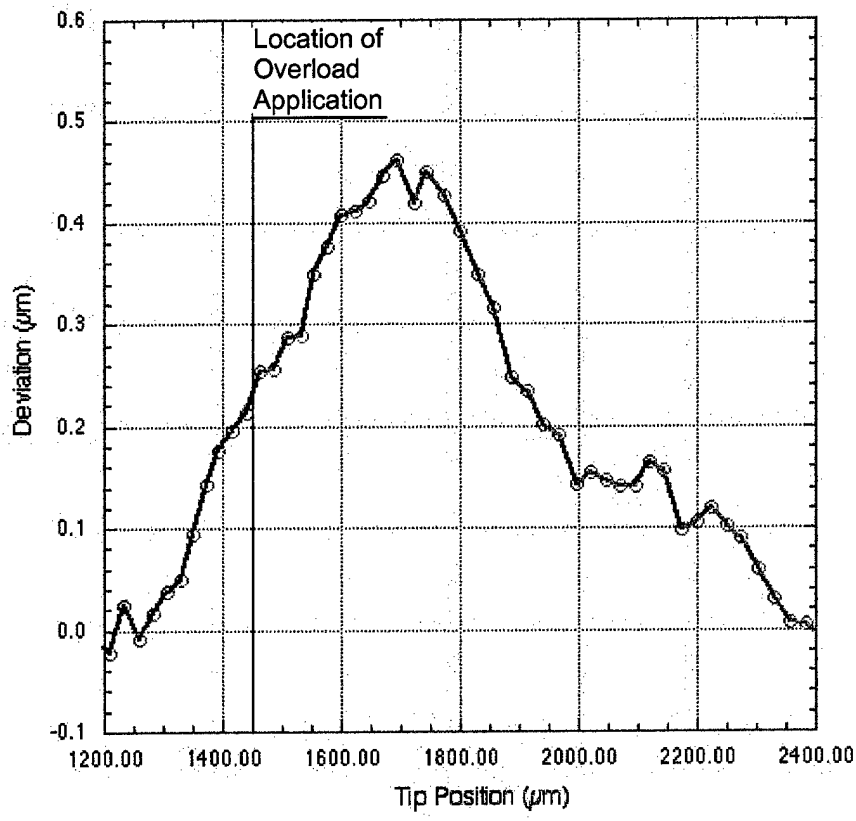

Figure AI-25. Deformation profile of the crack front in the vicinity of overload application.

Ti-alloy, R=0.5, freq=20 Hz, baseline K_{max}=15 MPa√m, overload Kmax=18.75 MPa√m (1.25 times the baseline stress intensity).

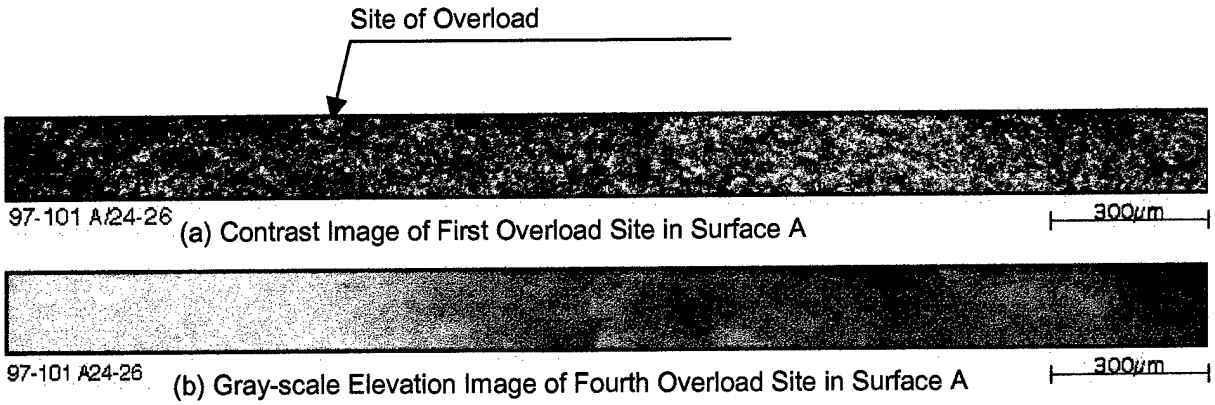

Figure AI-26. Contrast and gray-scale elevation images of fracture surface area surrounding overload site.

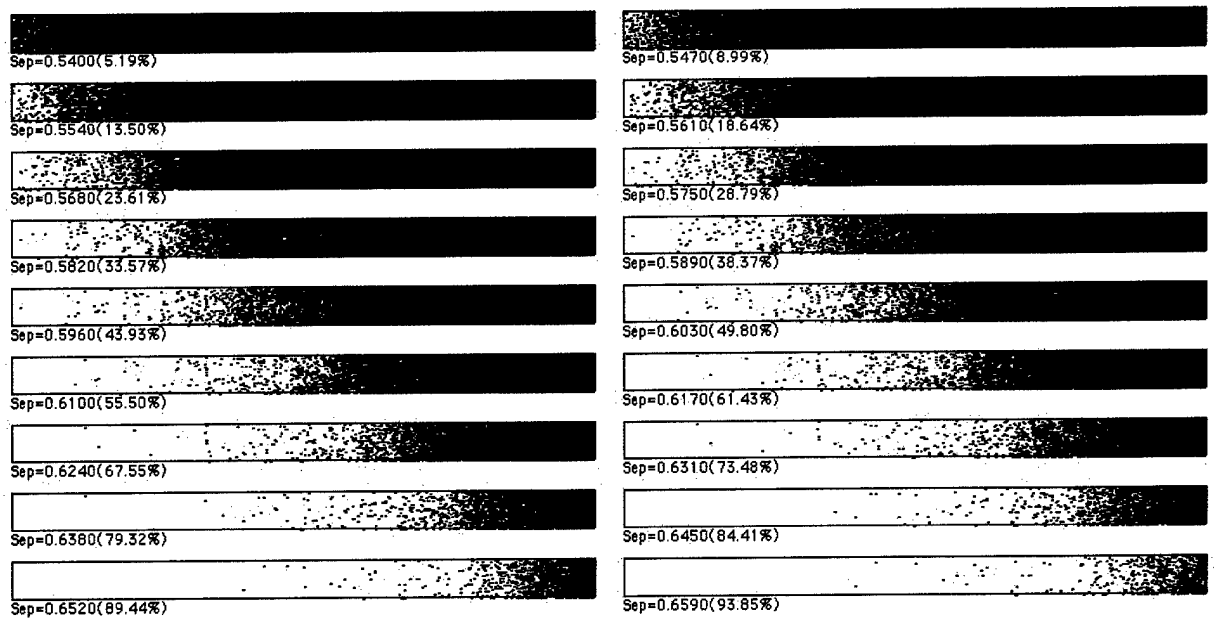

Figure AI-27. Fractured area projection plots (FAPPs) indicating the progression of the crack front.

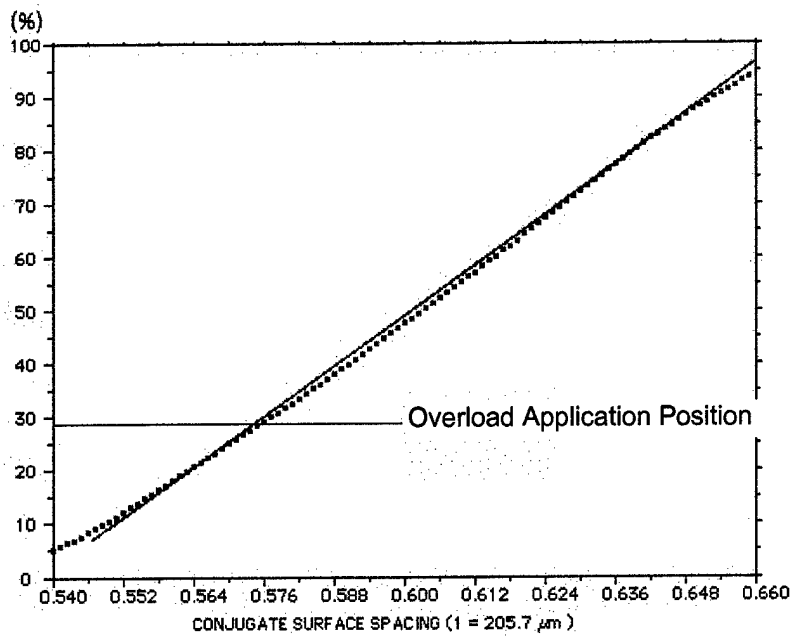

Figure AI-28. Increase in fractured area with increased spacing of the conjugate topographs.

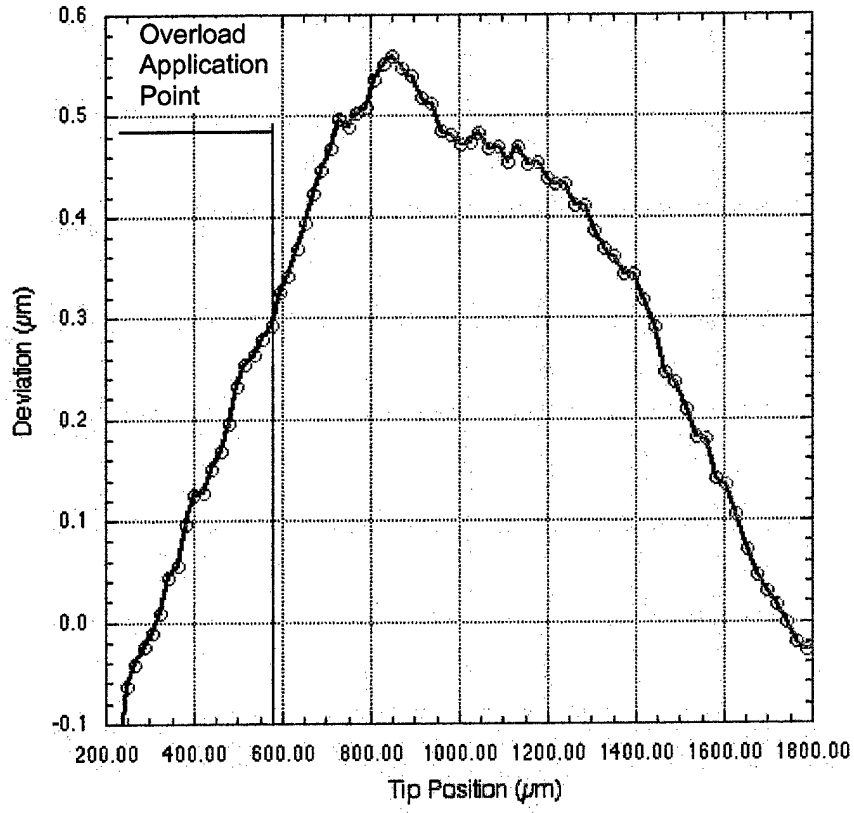

Figure AI-29. Deformation profile of the crack front in the vicinity of overload application.

Ti-alloy, R=0.5, freq=20 Hz, baseline K_{max}=15 MPa√m, overload Kmax=22.50 MPa√m (1.50 times the baseline stress intensity).

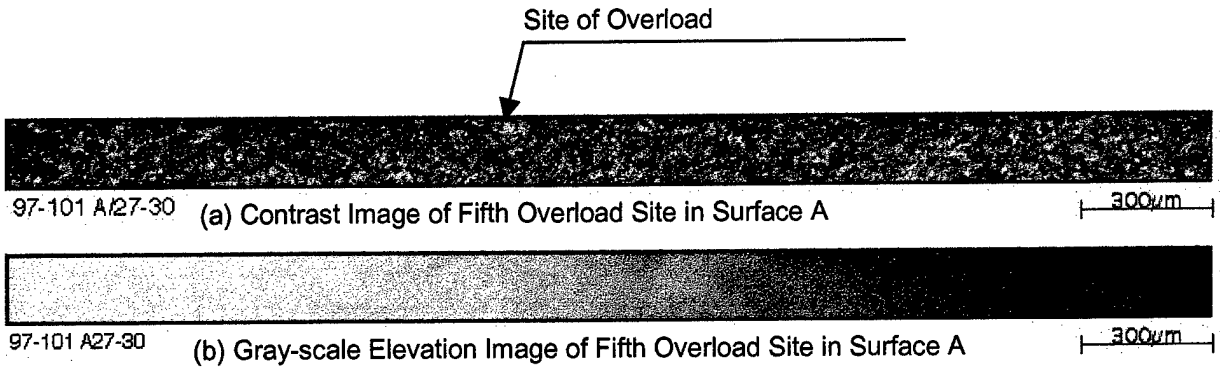

Figure AI-30. Contrast and gray-scale elevation images of fracture surface area surrounding overload site.

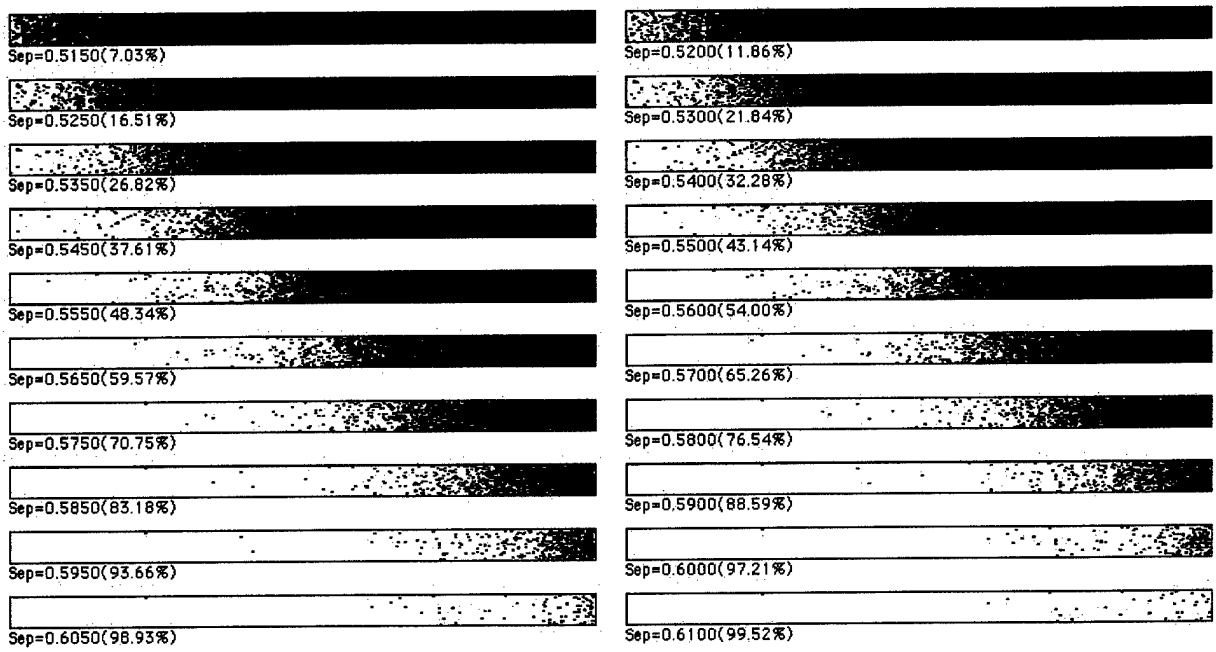

Figure AI-31. Fractured area projection plots (FAPPs) indicating the progression of the crack front.

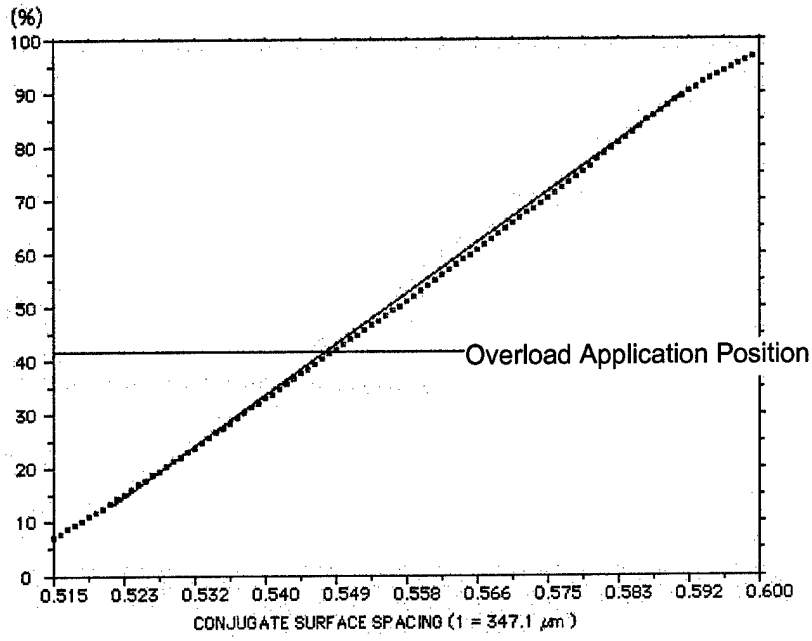

Figure AI-32. Increase in fractured area with increased spacing of the conjugate topographs.

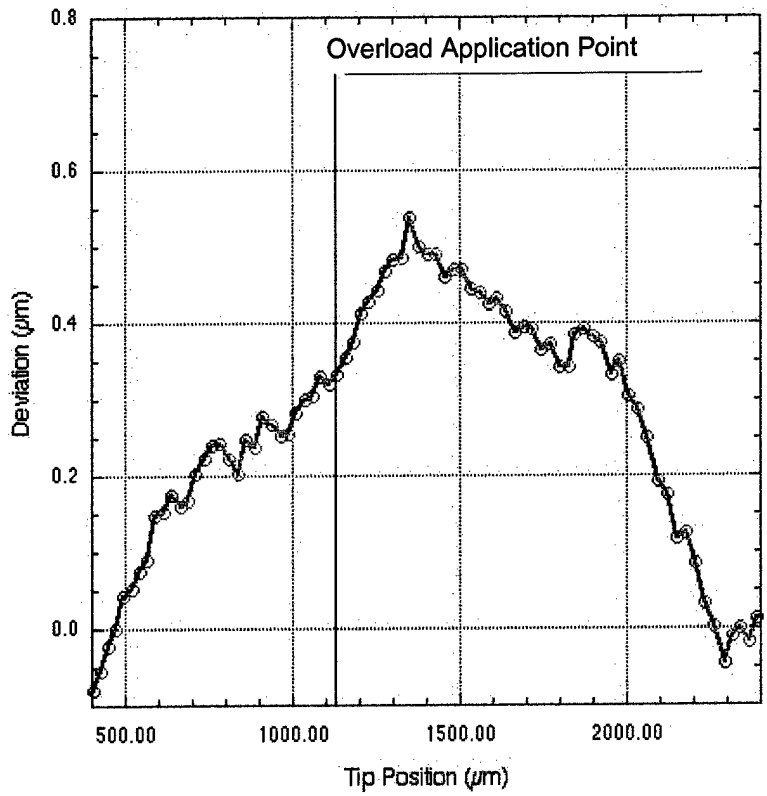

Figure AI-33. Deformation profile of the crack front in the vicinity of overload application.

Ti-alloy, R=0.05, freq=20 Hz, baseline K_{max}=15 MPa√m, overload Kmax=22.50 MPa√m (1.50 times the baseline stress intensity).

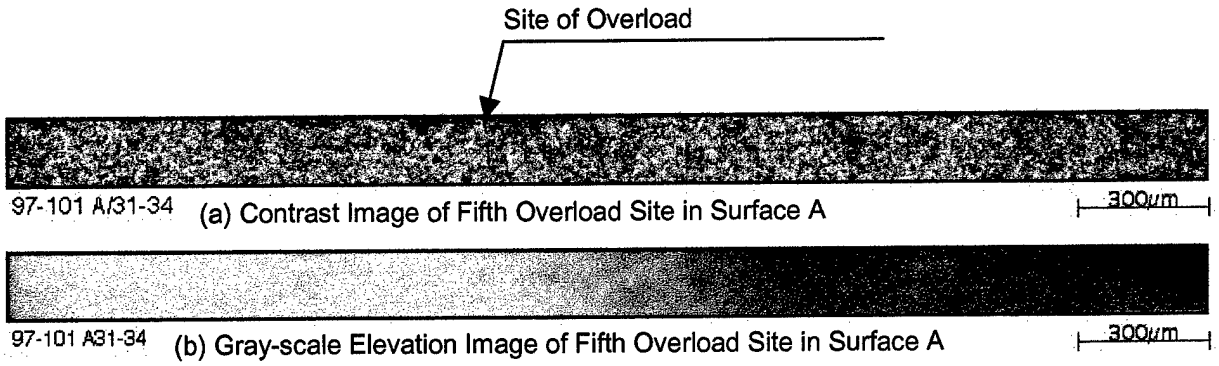

Figure AI-34. Contrast and gray-scale elevation images of fracture surface area surrounding overload site.

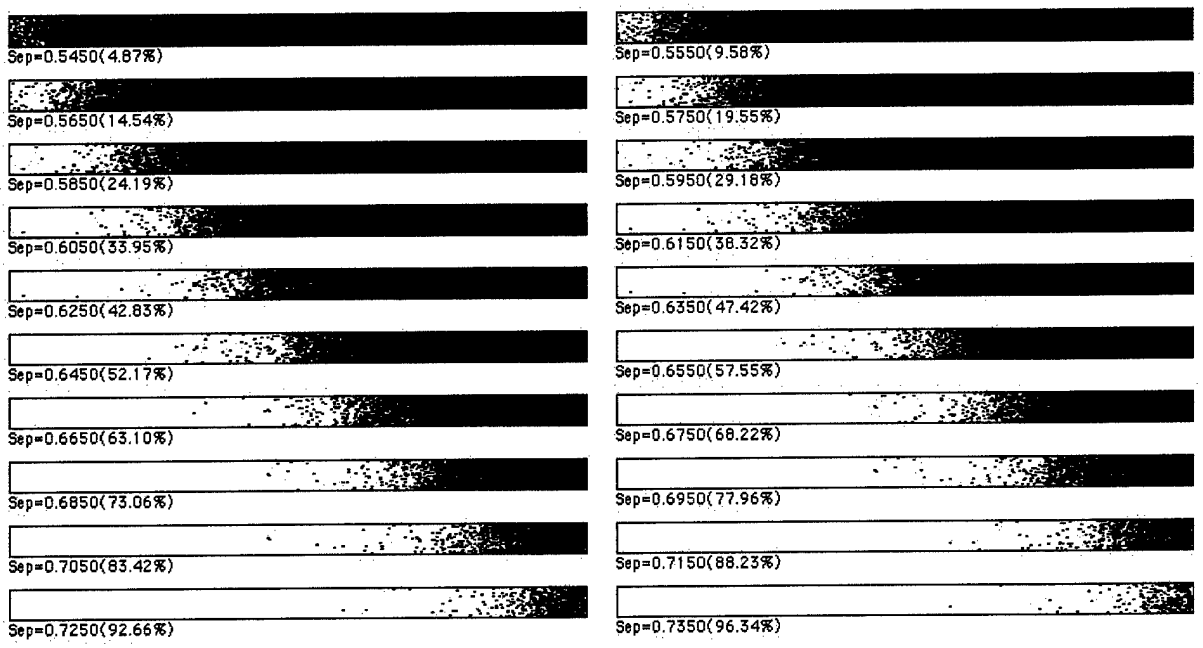

Figure AI-35. Fractured area projection plots (FAPPs) indicating the progression of the crack front.

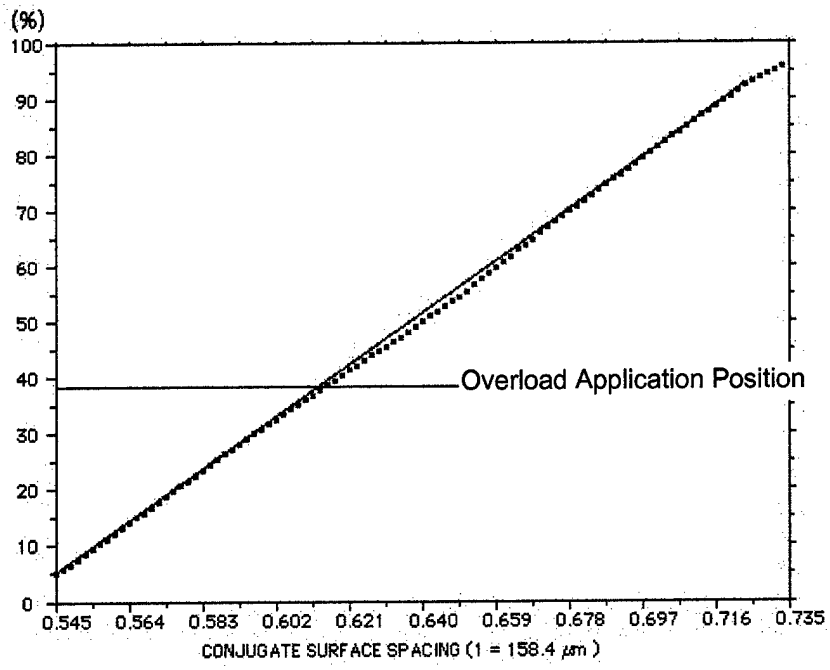

Figure AI-36. Increase in fractured area with increased spacing of the conjugate topographs.

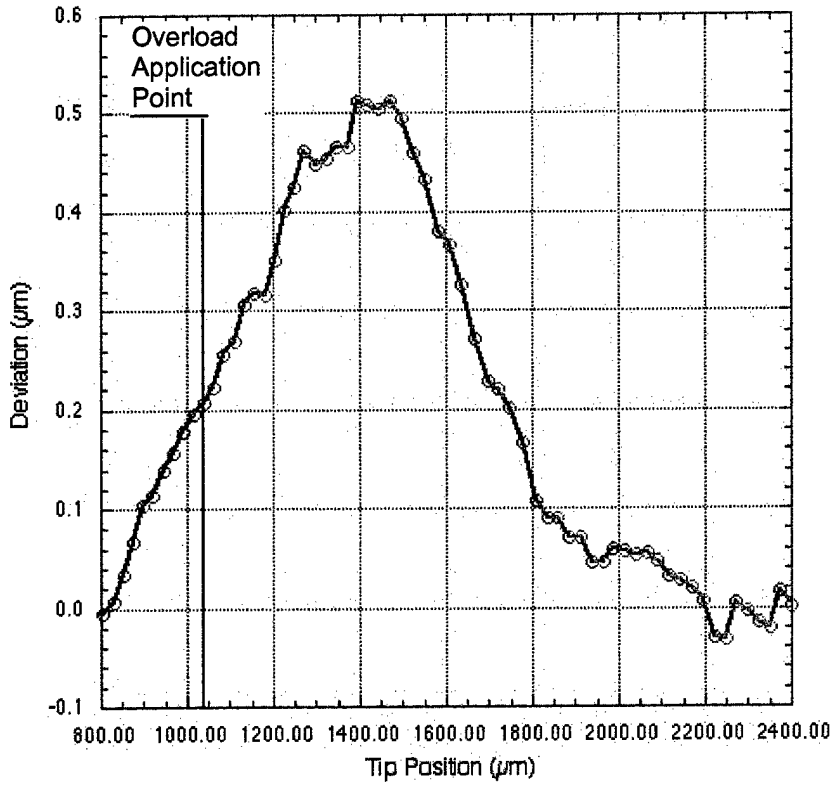

Figure AI-37. Deformation profile of the crack front in the vicinity of overload application.

Appendix II: IN100 NICKEL-BASE ALLOY

1. Nickel Based Super Alloy (IN100) Properties and Test Conditions

Two compact tension (CT) fatigue tests in which the load conditions were varied systematically were selected for analysis. One test was conducted at a baseline fatigue stress intensity of 1.5 MPa√m, and a stress ratio (R) of 0.05 in laboratory air at 650°C. Two different frequencies in fatiguing were used in this test, 20 Hz and 0.1667 Hz. During the fatigue loading, three magnitudes of single overloads (1.25, 1.375, and 1.75 times the maximum stress intensity of the baseline fatigue loading) were applied after approximately three mm of fatigue crack growth. The second test was conducted at a baseline stress intensity of 15 MPa√m, with a stress ratio of 0.5 in laboratory air at 650°C. Again, two frequencies were used for baseline fatigue loading, 20 Hz and 0.1667 Hz. Three magnitudes of single overloads were also applied after approximately three mm of crack growth. In the test with the stress ratio of 0.5, the crack did not reinitiate after the highest overload (1.75 times baseline fatigue stress intensity) even after a million baseline cycles. In these case the baseline fatigue stress intensity was raised to induce crack re-initiation.

The mechanical properties of IN100 at 650°C are tabulated in table AII-1.

TABLE AII-1. MECHANICAL PROPERTIES OF IN100

Modulus of Elasticity, E, (GPa)	210
Yield Strength, (MPa)	1062
Poisson's Ratio	0.300

The fatigue loading conditions for the two specimens are given in tables AII-2 and AII-3.

TABLE AII-2. TEST CONDITIONS FOR IN100 SPECIMEN NO. 82-213 (R = 0.05)

Load Status	Kmax (MPa√m)	Kmin (MPa√m)	R	Freq (Hz)	Number of Cycles	Crack Length (mm)
Baseline	30.0	1.50	0.05	20		9.423-12.43
1.25 OL	37.5	1.50	0.04	na	9570	12.43
Baseline	30.0	1.50	0.05	20		12.43-15.45
1.375 OL	45.0	1.50	0.03333	na	18973	15.45
Baseline	30.00	1.50	0.05	20		15.45-18.43
1.75 OL	52.5	1.50	0.02857	na	29432	18.43
Baseline	30.0	1.50	0.05	20		18.43-21.47
Baseline	30.0	1.50	0.05	0.1667		21.47-24.45
1.25 OL	37.5	1.50	0.04	na	42034	24.45
Baseline	30.0	1.50	0.05	0.1667		24.45-25.94
Paused at Minimum Load overnight	1.50	1.50		-------		25.94
Baseline	30.0	1.50	0.05	0.1667		25.94-27.43
1.375 OL	45.0	1.50	0.03333	na	43741	27.43
Baseline	30.0	1.50	0.05	0.1667		27.43-30.43
7 Overload Cycles	52.5	1.50	0.02875	na	45558	30.43-30.81
Baseline	30.0	1.50	0.05	0.1667		30.81-33.46
1.75 OL	52.5	1.50	0.02875	na	48296	33.46
Baseline	30.0	1.50	0.05	0.1667		33.46-36.43

TABLE AII-3. TEST CONDITIONS FOR IN100 SPECIMEN NO. 82-216
(R = 0.50)

Load Status	Kmax (MPa√m)	Kmin (MPa√m)	R	Freq (Hz)	Number of Cycles	Crack Length (mm)
Baseline	30.0	15.0	0.5	20		9.423-12.43
1.25 OL	37.5	15.0	0.4	na	23205	12.43
Baseline	30.0	15.0	0.5	20		12.43-15.66
1.375 OL	45.0	15.0	0.3333	na	48078	15.66
Baseline	30.00	15.0	0.5	20		15.66-18.70
1.75 OL	52.5	15.0	0.2857	na	78920	18.70
Baseline (No Crack Growth for 1,107.458 Cycles)	30.0	15.0	0.5	20		18.70-18.70
Raised Baseline	40.0	20.0	0.5	20		18.70-19.64
Lowered Baseline	30.0	15.0	0.5	20		19.64-22.66
Baseline	30.0	15.0	0.5	0.1667		22.66-5.44
1.25 OL	37.5	15.0	0.4	na	1222519	25.44
Baseline	30.0	15.0	0.5	0.1667		25.44-28.46
Paused at Minimum Load overnight	15.0	15.0		-------		28.46
1.375 OL	45.0	15.0	0.3333	na	1228576	28.46
Baseline	30.0	15.0	0.5	0.1667		28.46-30.94
Paused at Minimum Load overnight	15.0	15.0				30.94
Baseline	30.0	15.0	0.5	0.1667		30.94-31.45
1.75 OL	52.5	15.0	0.2875	na	1239488	31.45
Baseline (No Crack Growth for 12,429 Cycles)	30.0	15.0	0.5	0.1667		31.45-31.45
Raised Baseline	35.0	17.5	0.5	0.1667		31.45-34.26

In the above tests, the crack length was measured by a DC potential drop method. Figures AII-1 and AII-2 show a plot of the crack length versus the number of cycles for two cases. The crack growth rate deviated from the linear line at the point of overload application and the magnitude of deviation was roughly proportional to the magnitude of overload.

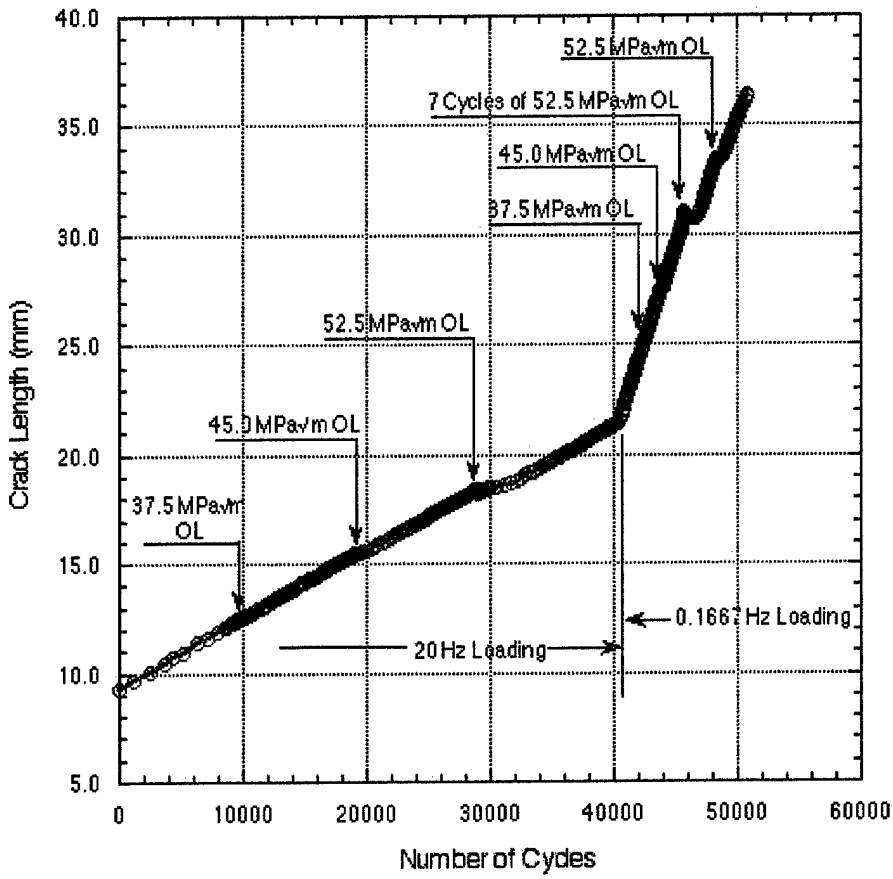

Figure AII-1. Crack length versus number of cycles for IN100 specimen 82-213 showing the effects of overload on crack growth behavior.

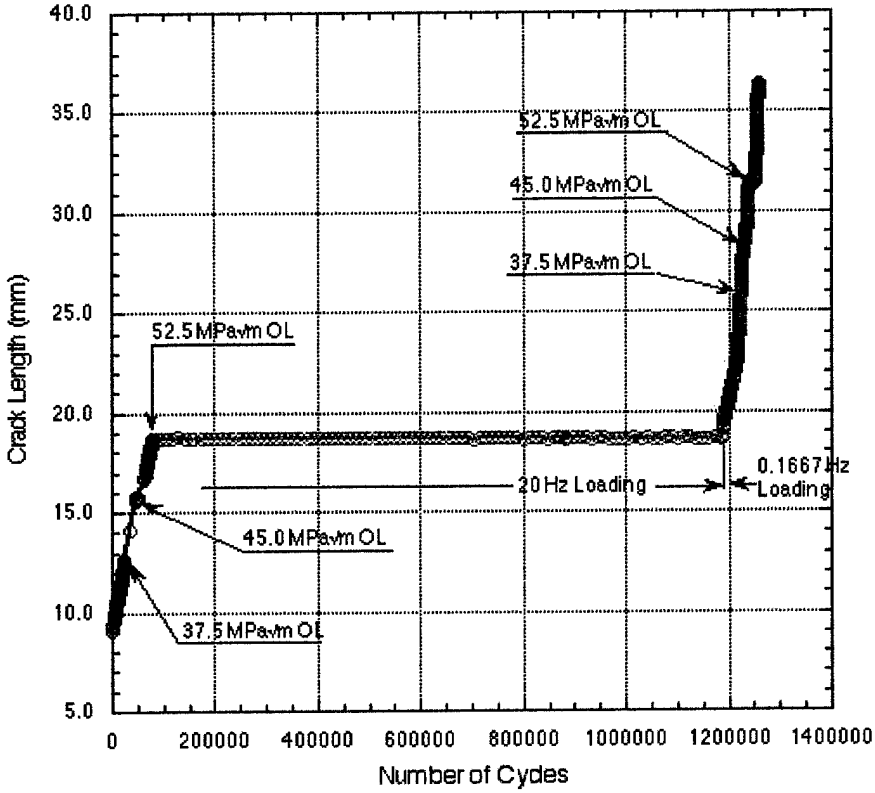

Figure AII-2. Crack length versus number of cycles for IN100 specimen 82-213 showing the effects of overload on crack growth behavior.

The plastic zone size for each overload level was calculated and summarized in table AII-4.

TABLE AII-4. CALCULATED PLASTIC ZONE SIZES UNDER PLANE STRAIN CONDITION

Applied Stress Intensity (MPa√m)	Radius of Plastic Zone (Plane Strain) (μm)
30	38.8
37.5	60.6
45.0	87.2
52.5	118.7

2. Fracture Surface Analysis Results

IN100-alloy, R=0.05, freq=20 Hz, baseline K_{max}=30.0 MPa√m, overload Kmax=37.5 MPa√m (1.25 times the baseline stress intensity).

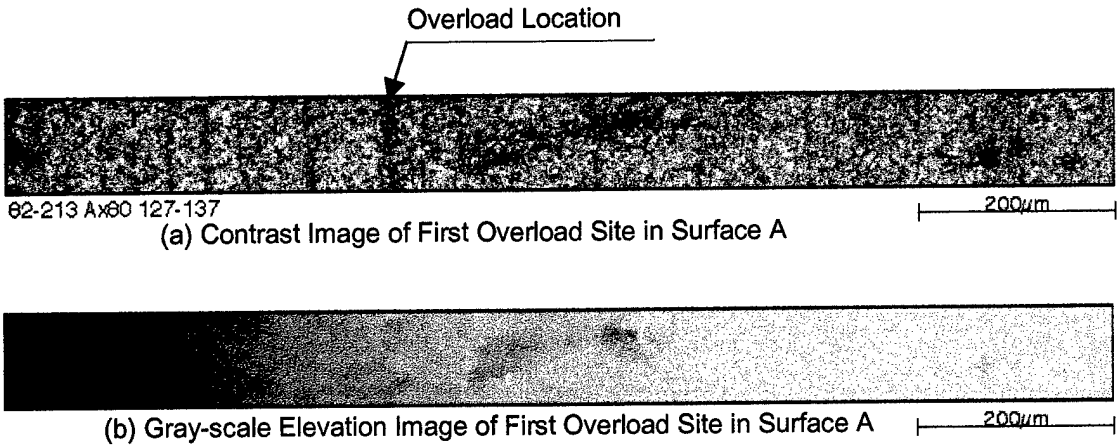

Figure AII-3. Contrast and gray-scale elevation images of fracture surface area surrounding 37.5 MPa√m overload site in baseline fatigue loading with R=0.05 and freq=20 Hz.

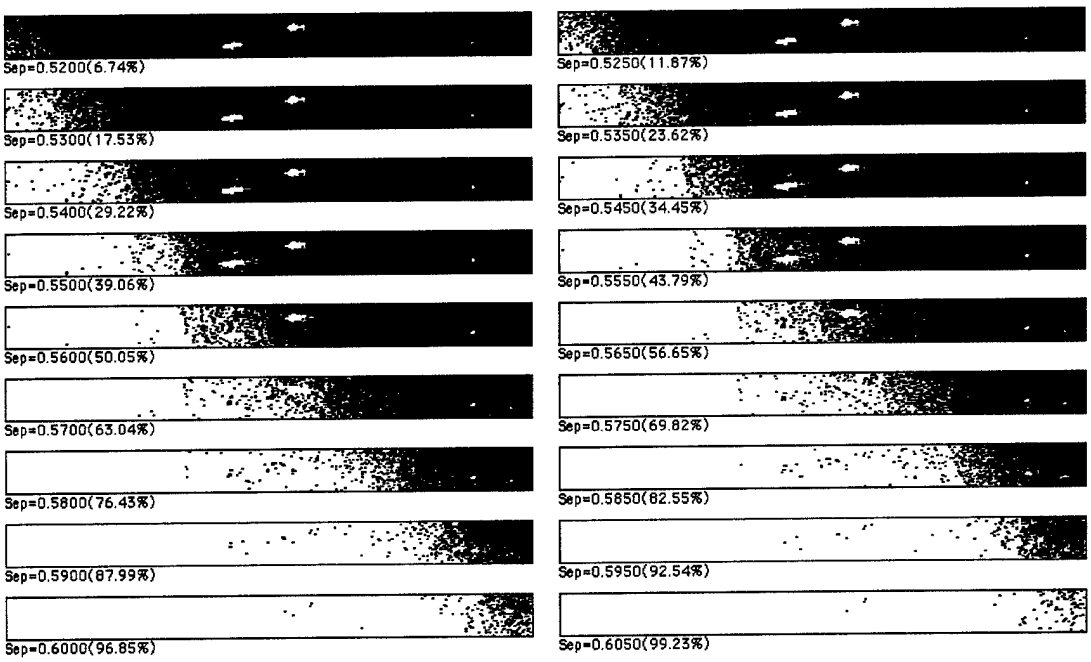

Figure AII-4. Fractured area projection plots (FAPPs) indicating the progress of the crack front.

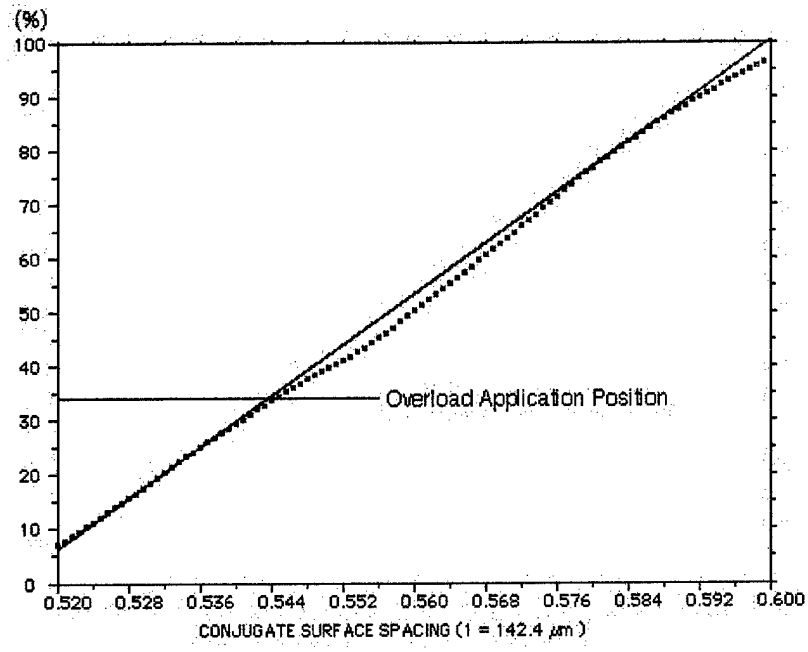

Figure AII-5. Increase in fractured area with increased spacing of the conjugate topographs.

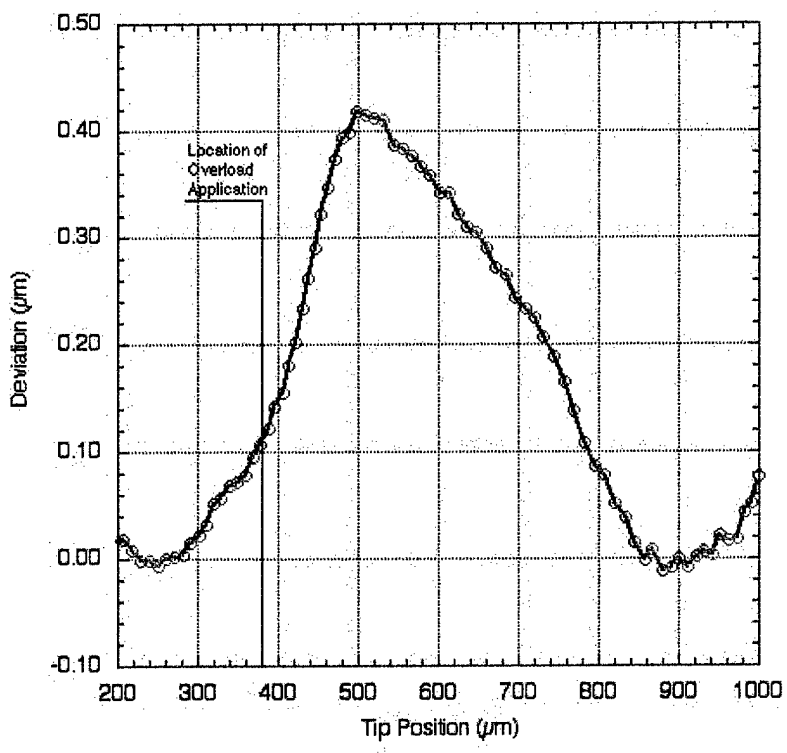

Figure AII-6. Deformation profile of the crack front in the vicinity of 37.5 MPA √m overload site in baseline fatigue loading with R=0.05 and freq=20 Hz

IN100-alloy, R=0.05, freq=20 Hz, baseline K_{max}=30.0 MPa√m, overload Kmax=45.0 MPa√m (1.375 times the baseline stress intensity).

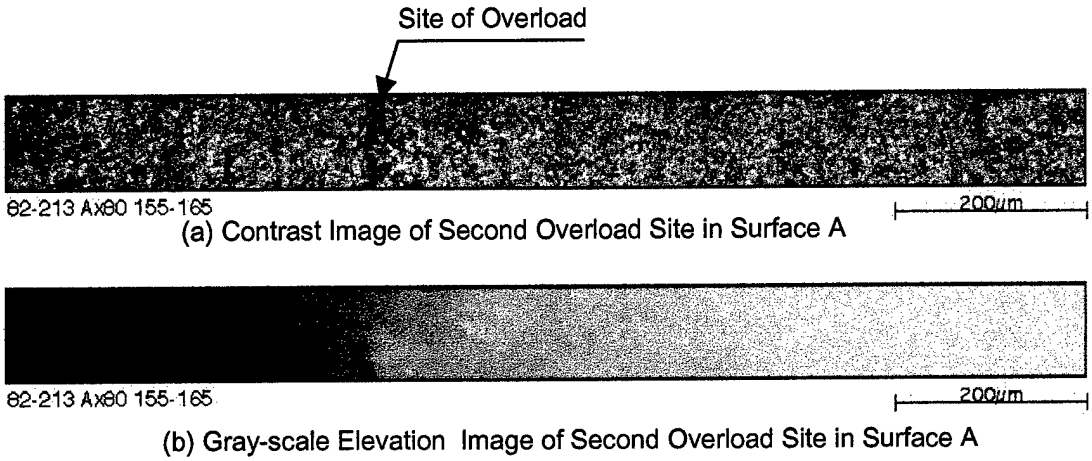

Figure AII-7. Contrast and gray-scale elevation images of fracture surface area surrounding 45.0 MPa√m overload site in baseline fatigue loading with R=0.05 and freq=20 Hz.

Figure AII-8. Fractured area projection plots (FAPPs) indicating the progression of the crack front.

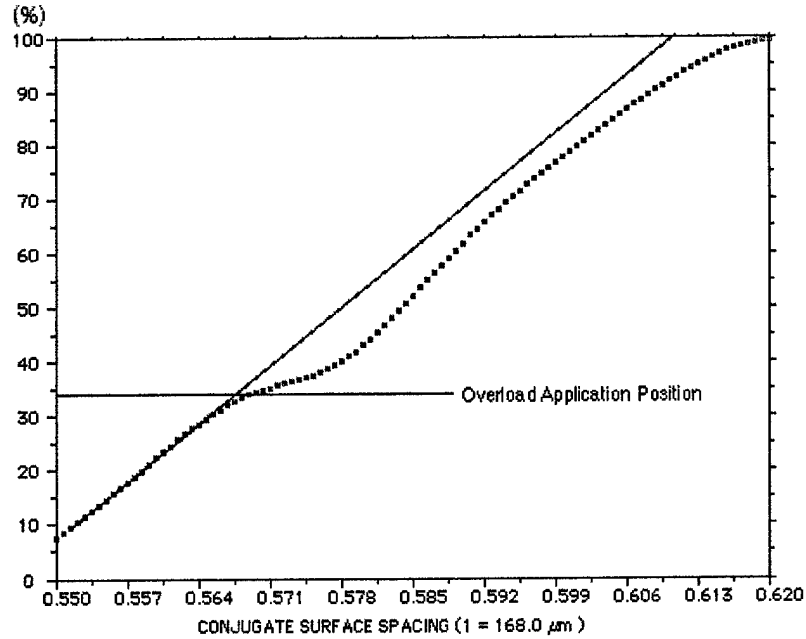

Figure AII-9. Increase in fractured area with increased spacing of the conjugate topographs.

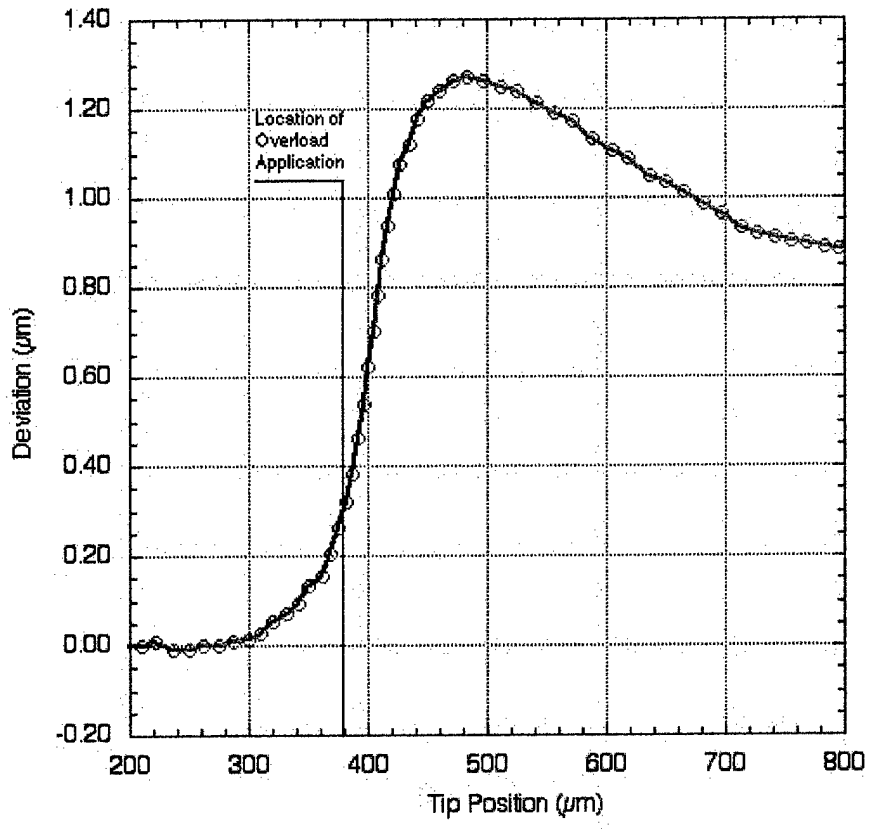

Figure AII-10. Deformation profile of the crack front in the vicinity of 45.0 MPa√m overload site in baseline fatigue loading with R=0.05 and freq=20 Hz.

IN100-alloy, R=0.05, freq=20 Hz, baseline K_{max}=30.0 MPa√m, overload Kmax=52.5 MPa√m (1.75 times the baseline stress intensity).

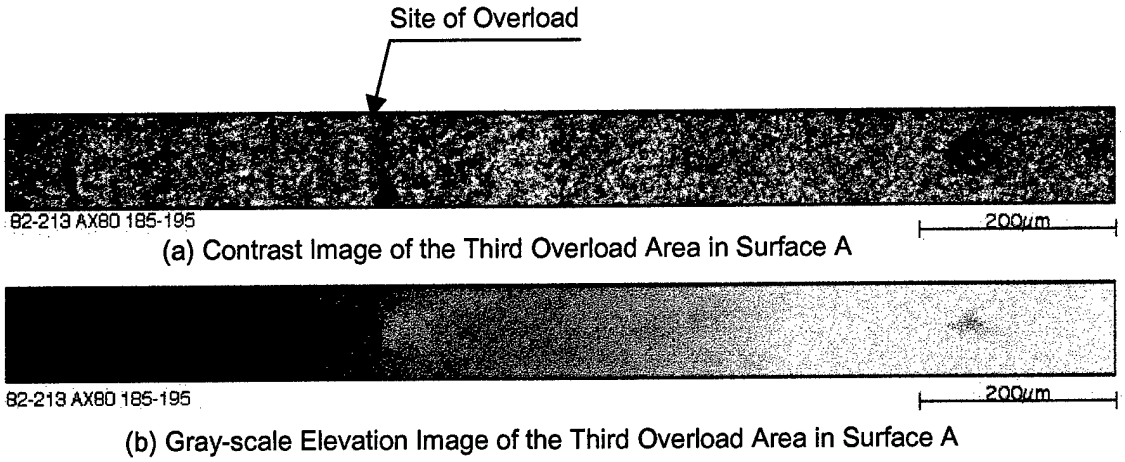

Figure AII-11. Contrast and gray-scale elevation images of fracture surface area surrounding the 52.5 MPa√m overload site in baseline fatigue loading with R=0.05 and freq=20 Hz.

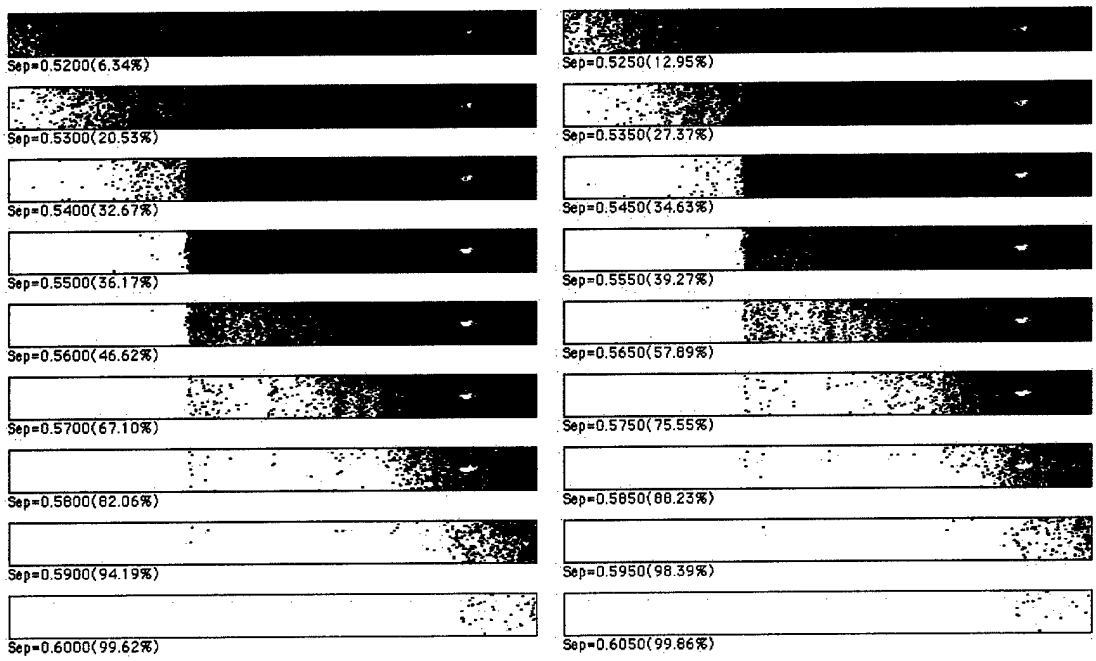

Figure AII-12. Fractured area projection plots (FAPPs) indicating the progression of the crack front.

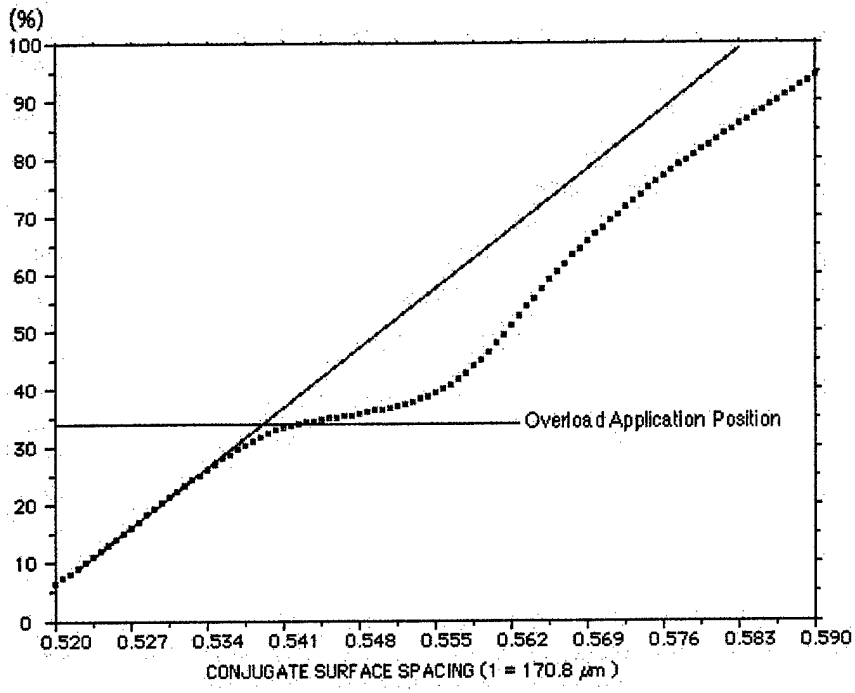

Figure AII-13. Increase in fractured area with increased spacing of the conjugate topographs.

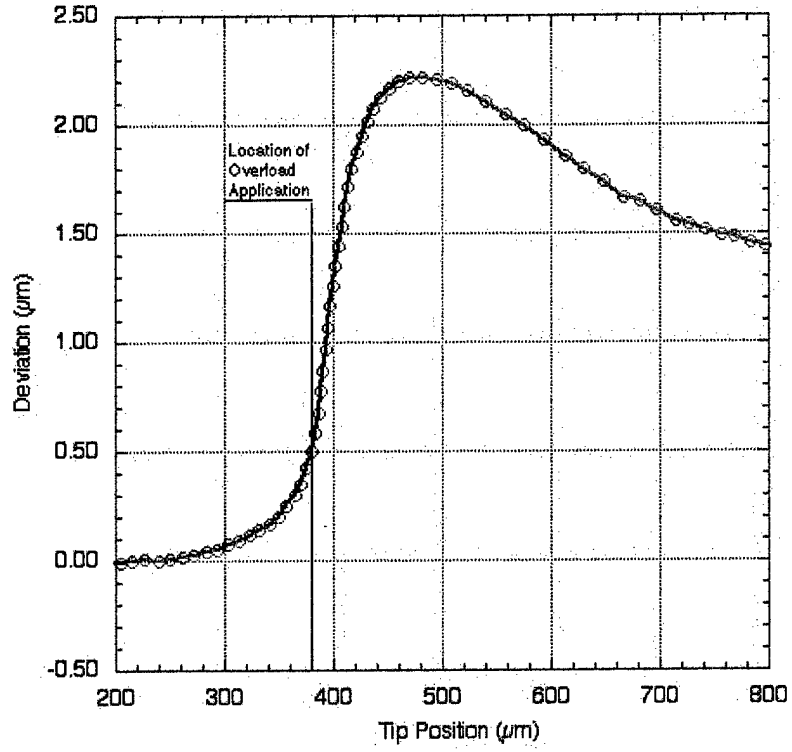

Figure AII-14. Deformation profile of the crack front in the vicinity of 52.5 MPa√m overload site in baseline fatigue loading with R=0.05 and freq=20 Hz.

IN100-alloy, R=0.05, freq=0.1667 Hz, baseline K_{max}=30.0 MPa√m, overload Kmax=37.5 MPa√m (1.25 times the baseline stress intensity).

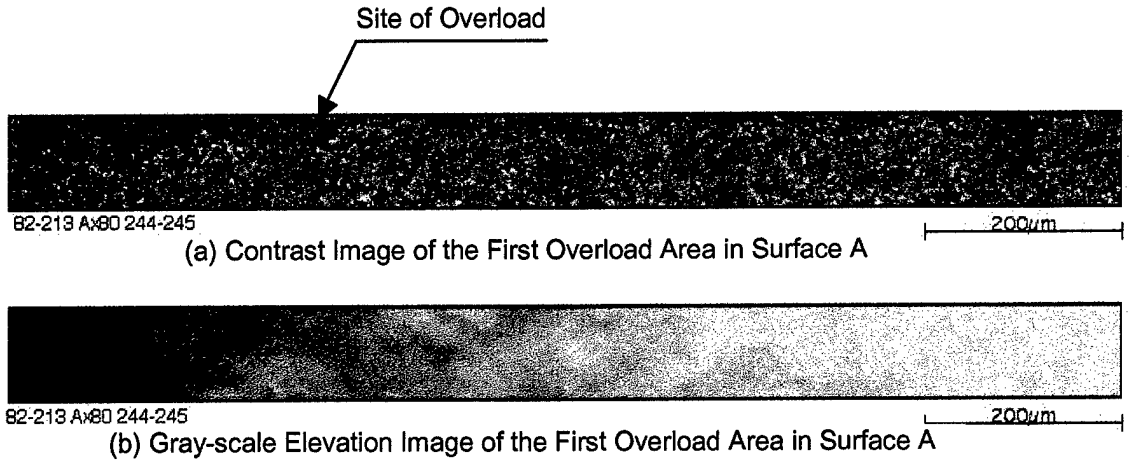

Figure AII-15. Contrast and gray-scale elevation images of fracture surface area surrounding 37.5 MPa√m overload site in baseline fatigue loading with R=0.05 and freq=0.1667 Hz.

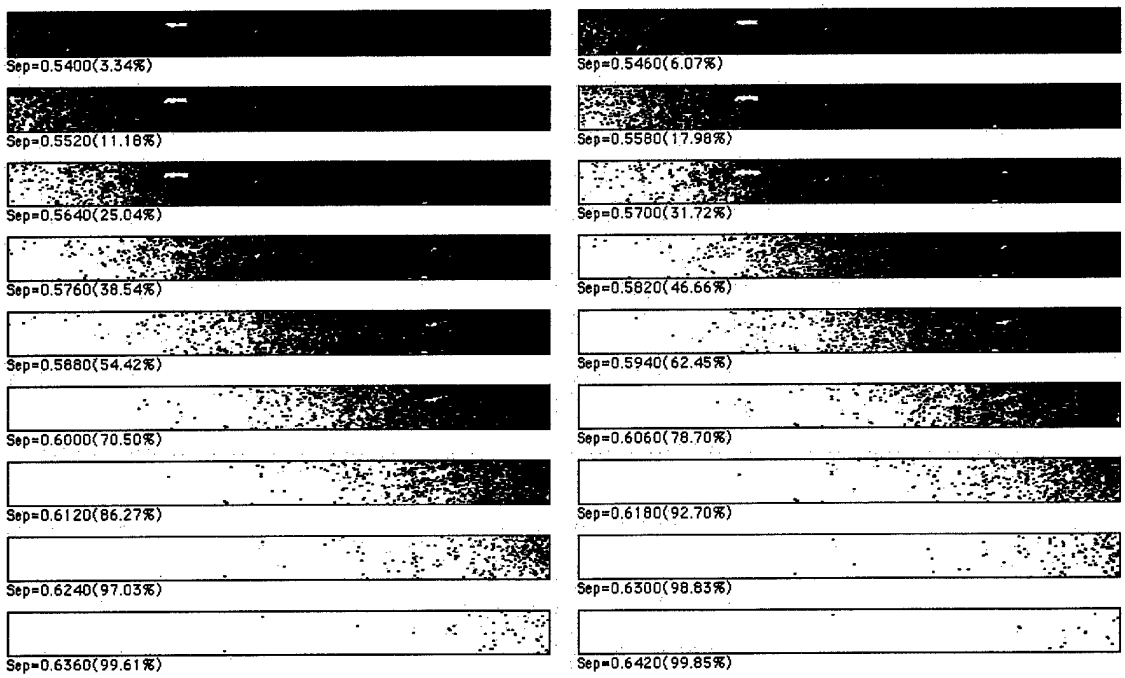

Figure AII-16. Fractured area projection plots (FAPPs) indicating the progression of the crack front.

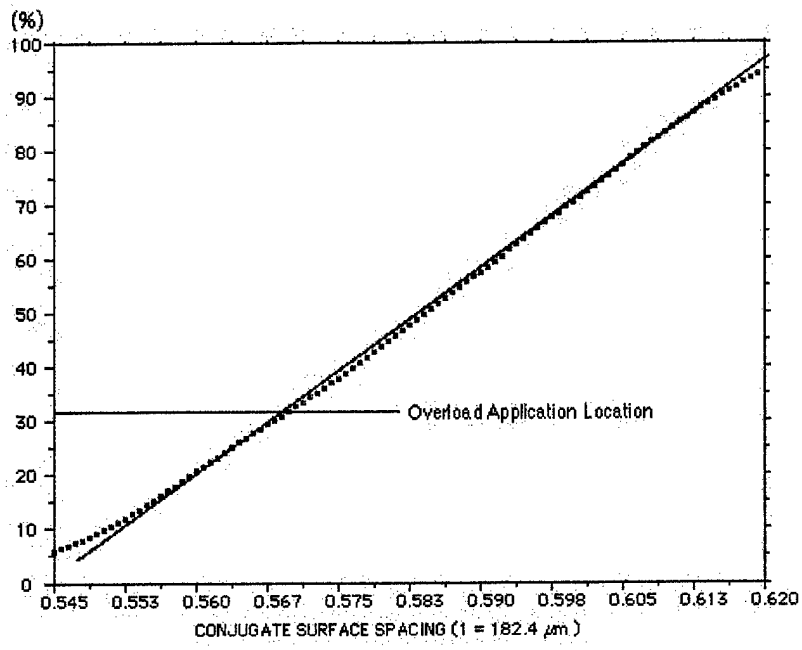

Figure AII-17. Increase in fractured area with increased spacing of the conjugate topographs.

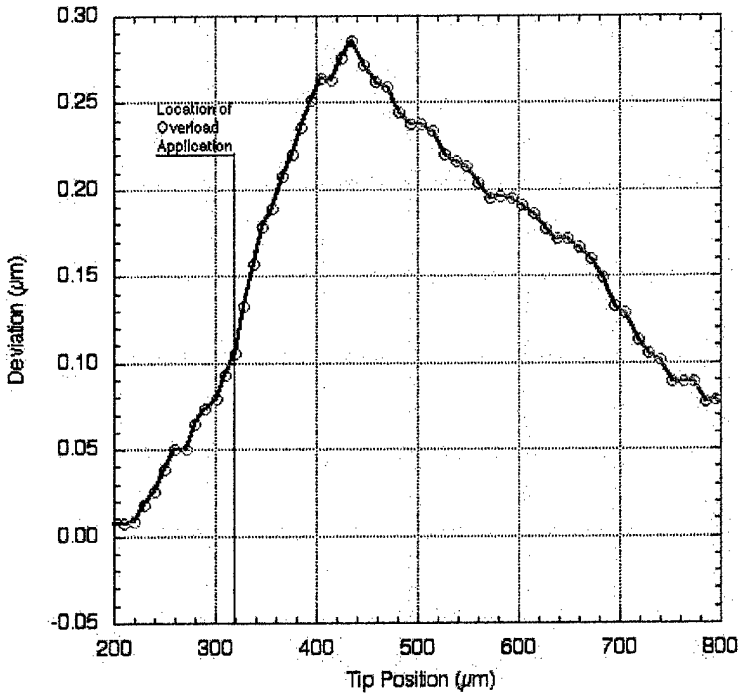

Figure AII-18. Deformation profile of the crack front in the vicinity of 37.5 MPa√m overload site in baseline fatigue loading with R=0.05 and freq=0.1667 Hz.

IN100-alloy, R=0.05, freq=0.1667 Hz, baseline K_{max}=30.0 MPa√m, overload Kmax=45.0 MPa√m (1.375 times the baseline stress intensity).

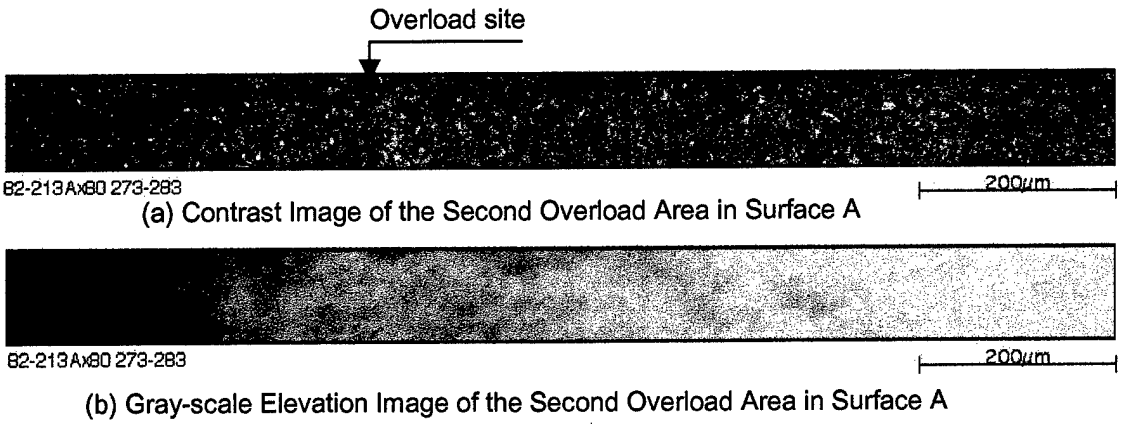

(a) Contrast Image of the Second Overload Area in Surface A

(b) Gray-scale Elevation Image of the Second Overload Area in Surface A

Figure AII-19. Contrast and gray-scale elevation images of fracture surface area surrounding the 45.0 MPa√m overload site in baseline fatigue loading with R=0.05 and freq=0.1667 Hz.

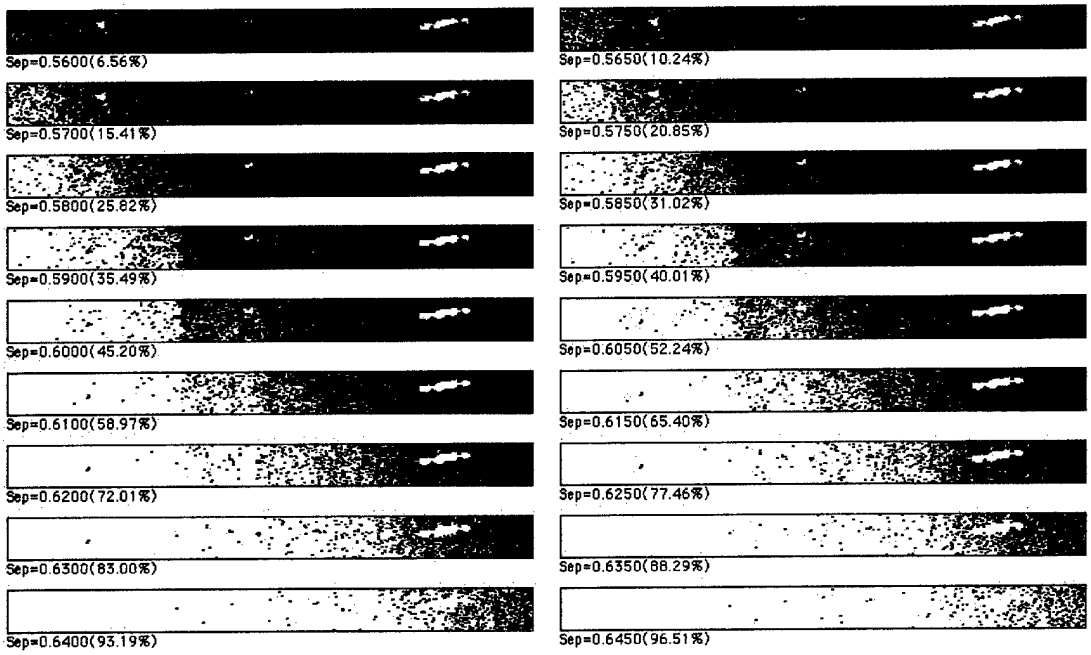

Figure AII-20. Fractured area projection plots (FAPPs) indicating the progression of the crack front.

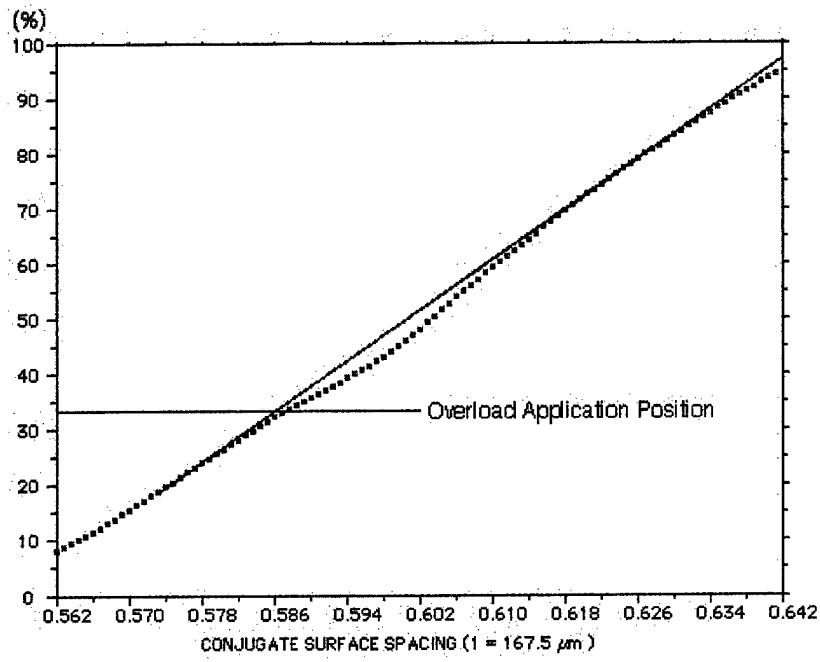

Figure AII-21. Increase in fractured area with increased spacing of the conjugate topographs.

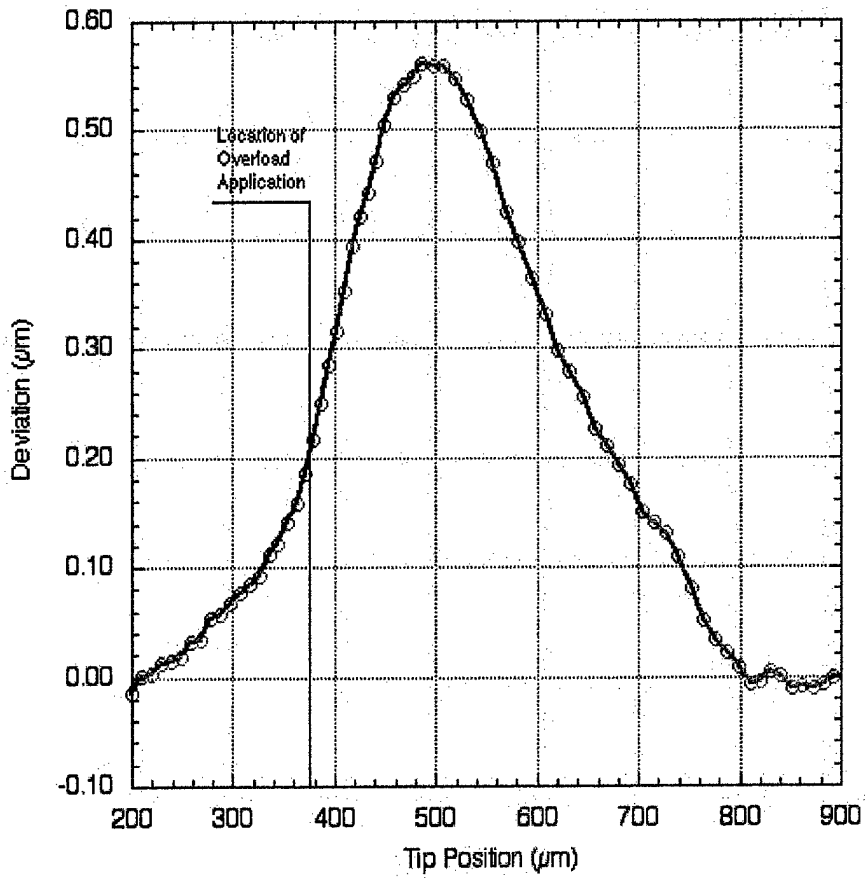

Figure AII-22. Deformation profile of the crack front in the vicinity of the 45.0 MPa√m overload site in baseline fatigue loading with R=0.05 and freq=0.1667 Hz.

IN100-alloy, R=0.05, freq=0.1667 Hz, baseline K_{max}=30.0 MPa√m, seven cycles of overload Kmax=52.5 MPa√m (1.75 times the baseline stress intensity)

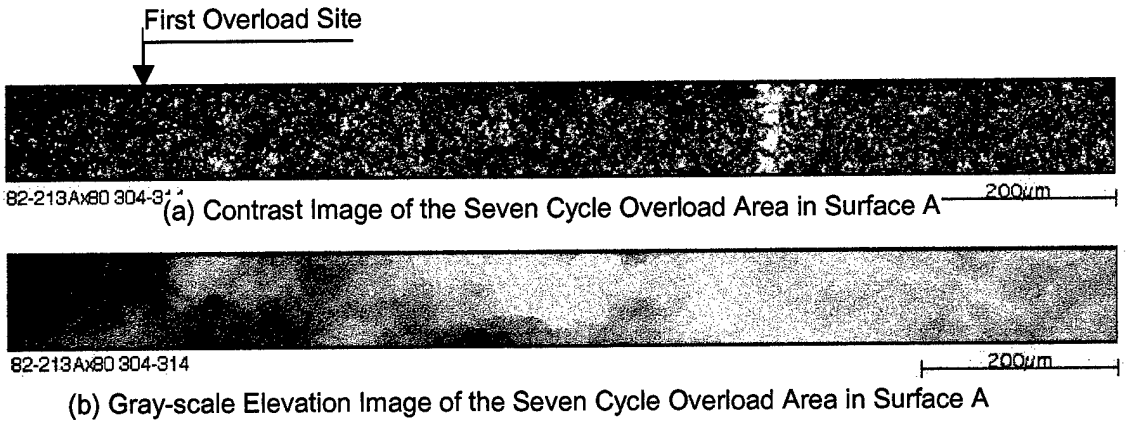

(a) Contrast Image of the Seven Cycle Overload Area in Surface A

(b) Gray-scale Elevation Image of the Seven Cycle Overload Area in Surface A

Figure AII-23. Contrast and gray-scale elevation images of fracture surface area surrounding the seven cycles of 52.5 MPa√m overload site in baseline fatigue loading with R=0.05 and freq=0.1667 Hz.

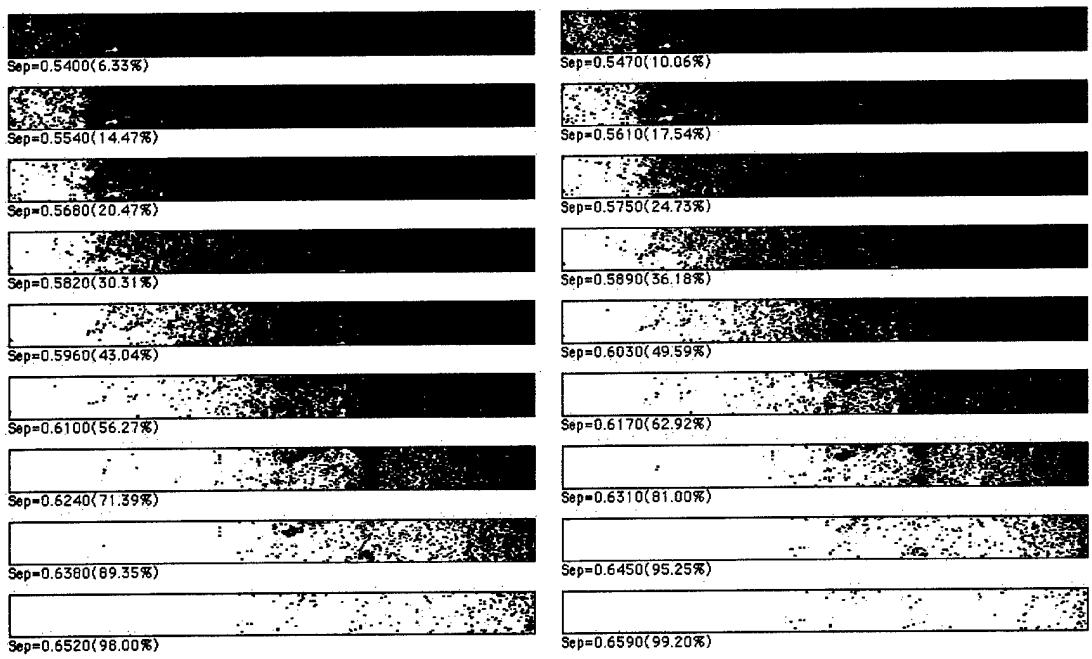

Figure AII-24. Fractured area projection plots (FAPPs) indicating the progression of the crack front.

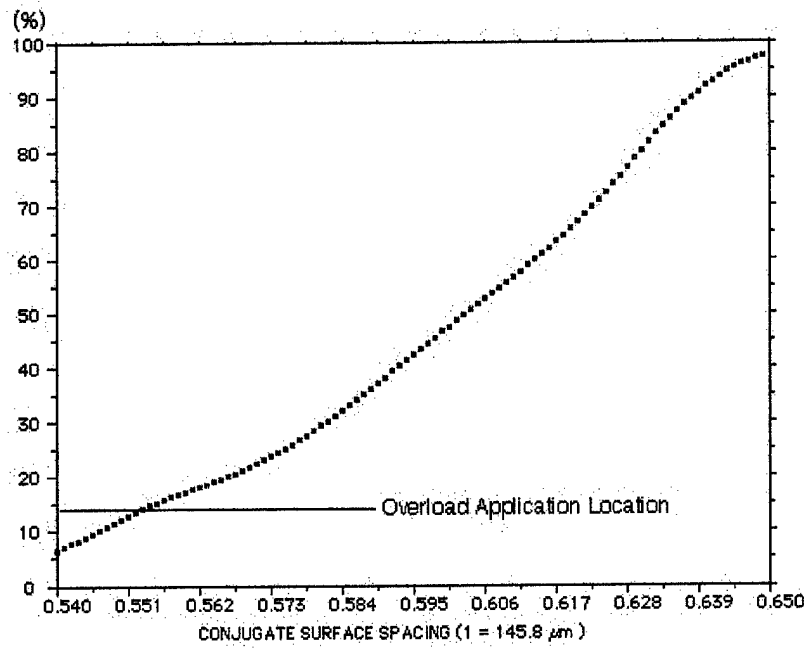

Figure AII-25. Increase in fractured area with increased spacing of the conjugate topographs.

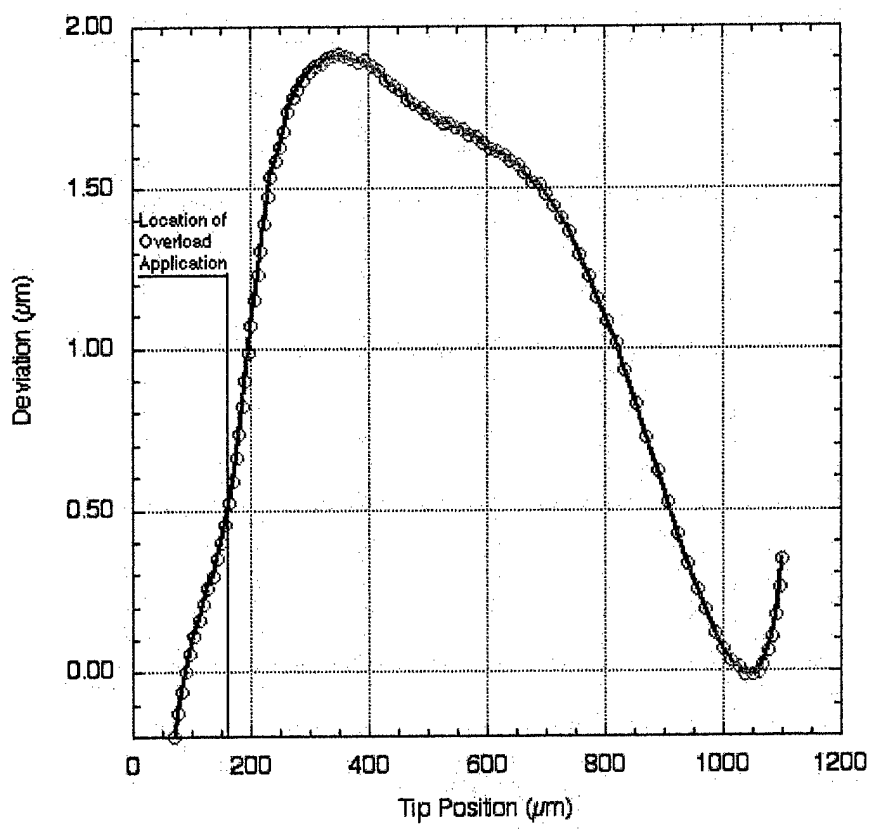

Figure AII-26. Deformation profile of the crack front in the vicinity of the seven cycles 52.5 MPa√m overload site in baseline fatigue loading with R=0.05 and freq=0.1667 Hz.

IN100-alloy, R=0.05, freq=0.1667 Hz., baseline K_{max}=30.0 MPa√m, one cycle of overload Kmax=52.5 MPa√m (1.75 times the baseline stress intensity)

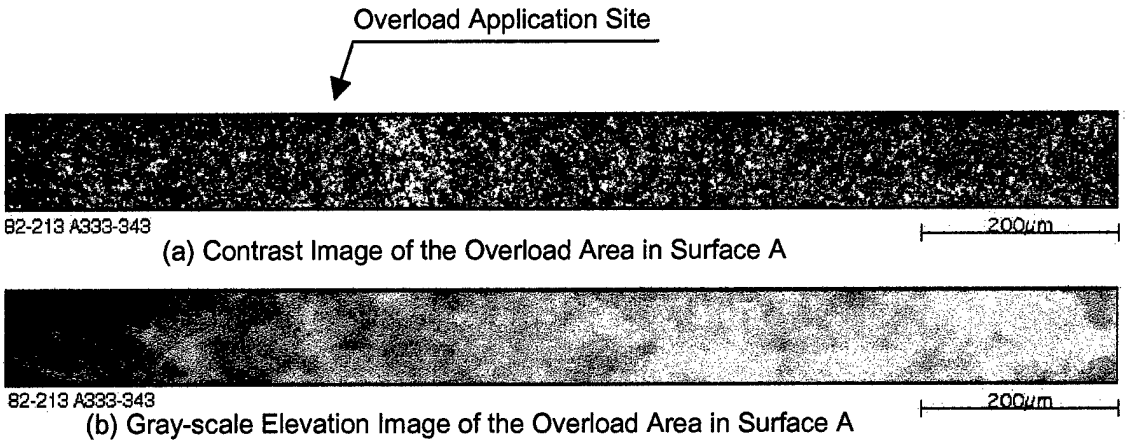

Figure AII-27. Contrast and gray-scale elevation images of single 52.5 MPa √m overload in R=0.05 and freq=0.1667 Hz. baseline fatigue region.

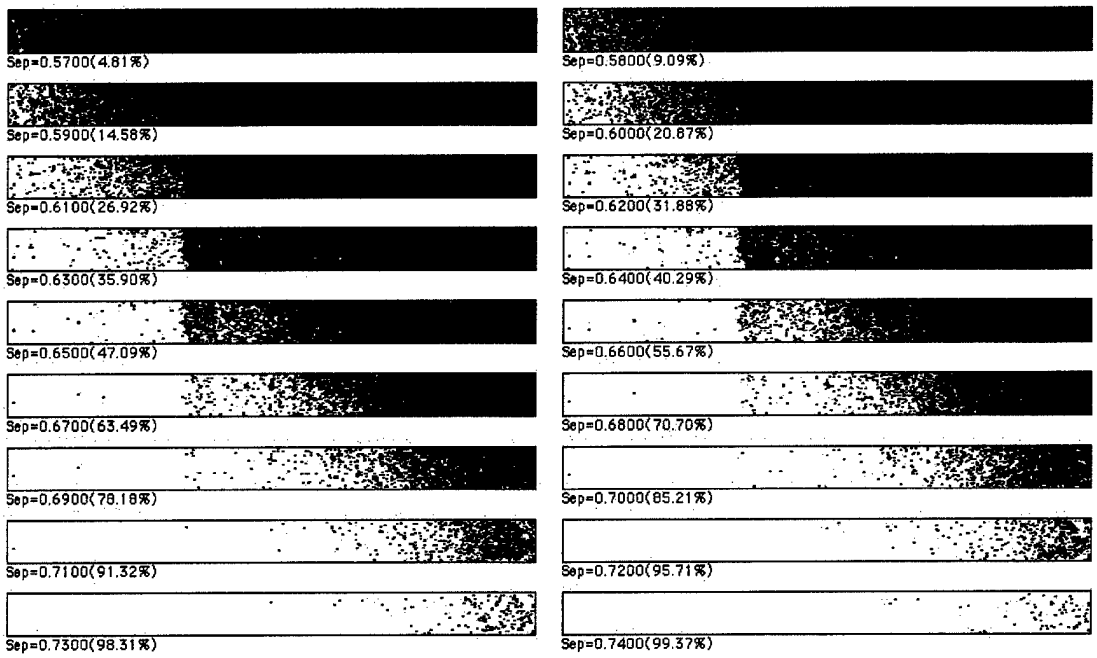

Figure AII-28. Fractured area projection plots (FAPPs) indicating the progression of the crack front.

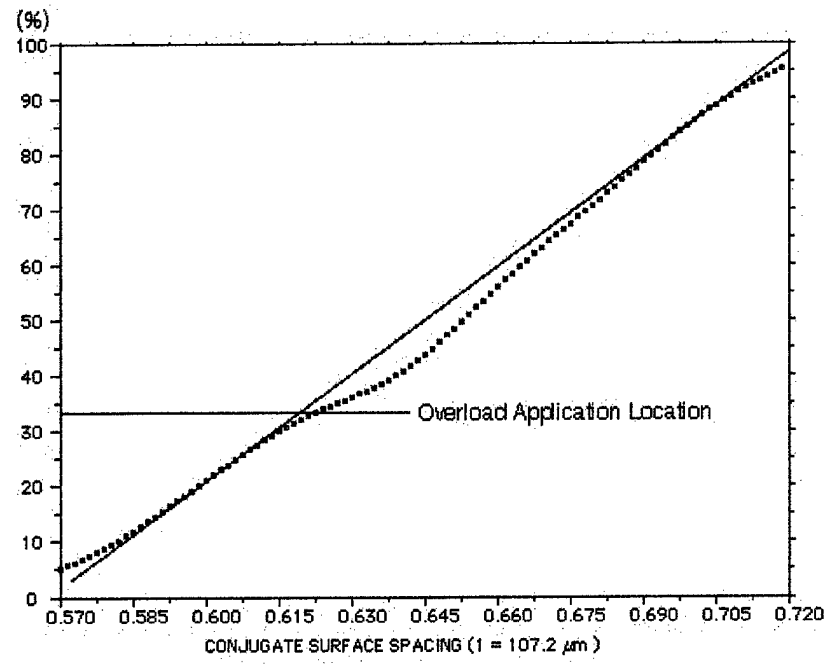

Figure AII-29. Increase in fractured area with increased spacing of the conjugate topographs.

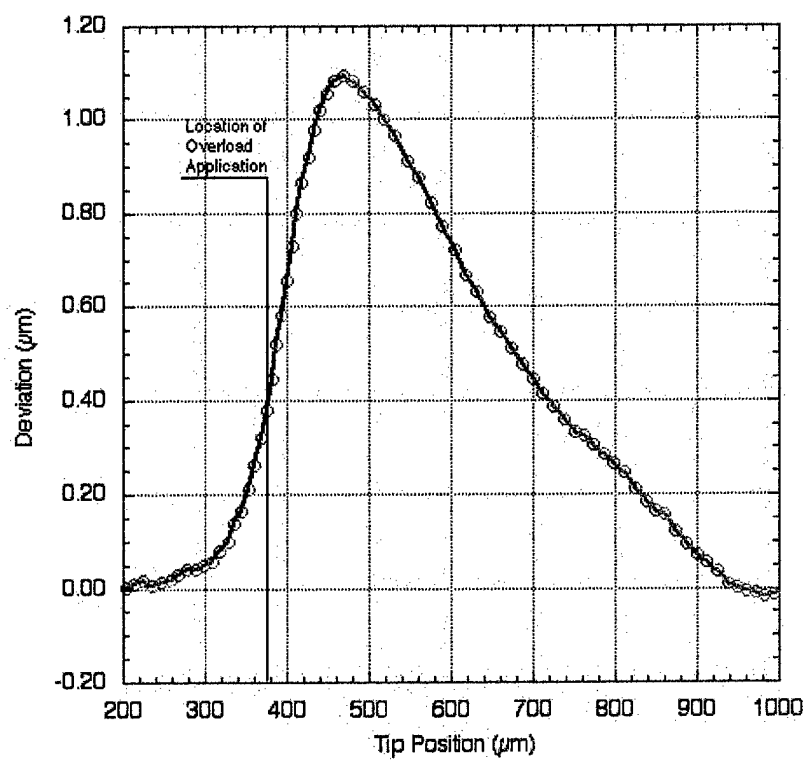

Figure AII 30. Deformation profiles of the crack front in the vicinity of 52.5 MPa√m overload in the baseline fatigue loading of R=0.05 and 0.1667 Hz.

IN100-alloy, R=0.50, freq=20 Hz, baseline K_{max}=30.0 MPa√m, overload Kmax=37.5 MPa√m (1.25 times the baseline stress intensity)

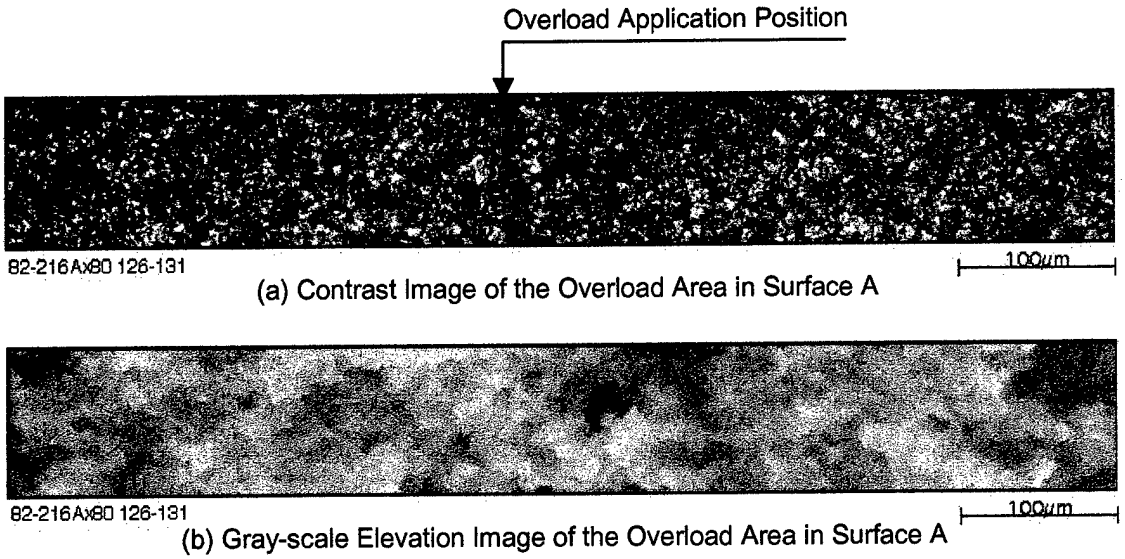

Figure AII-31. Contrast and gray-scale elevation images of single 37.5 MPa √m overload in R=0.50 and freq=20 Hz baseline fatigue region.

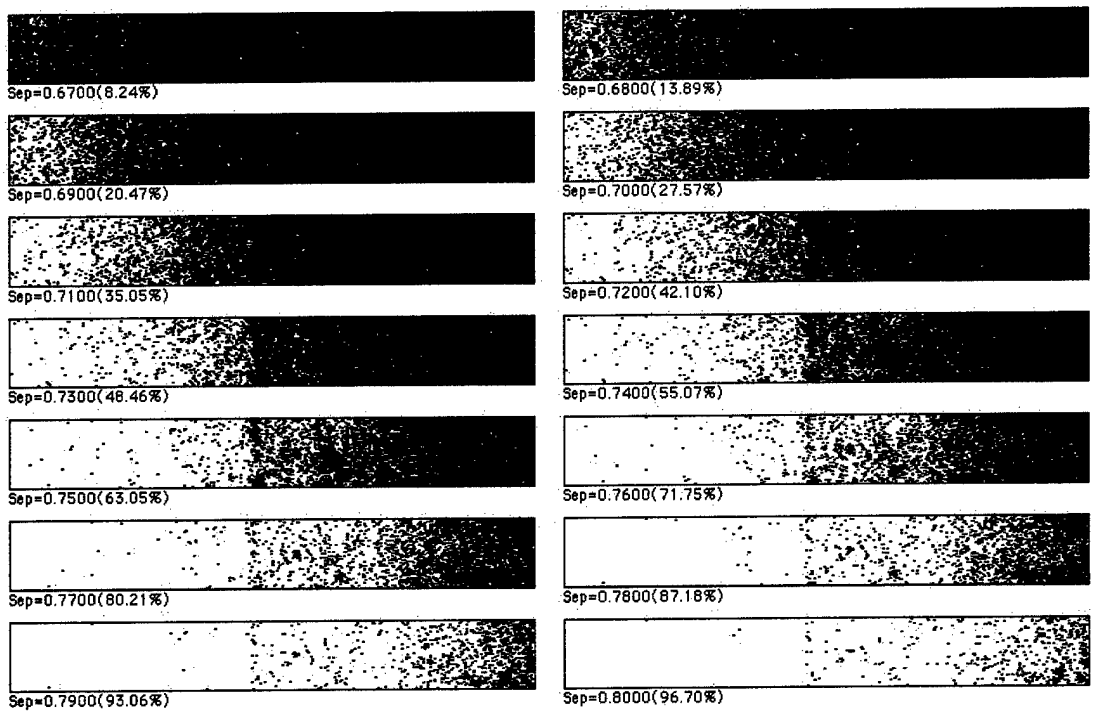

Figure AII-32. Fractured area projection plots (FAPPs) indicating the progression of the crack front.

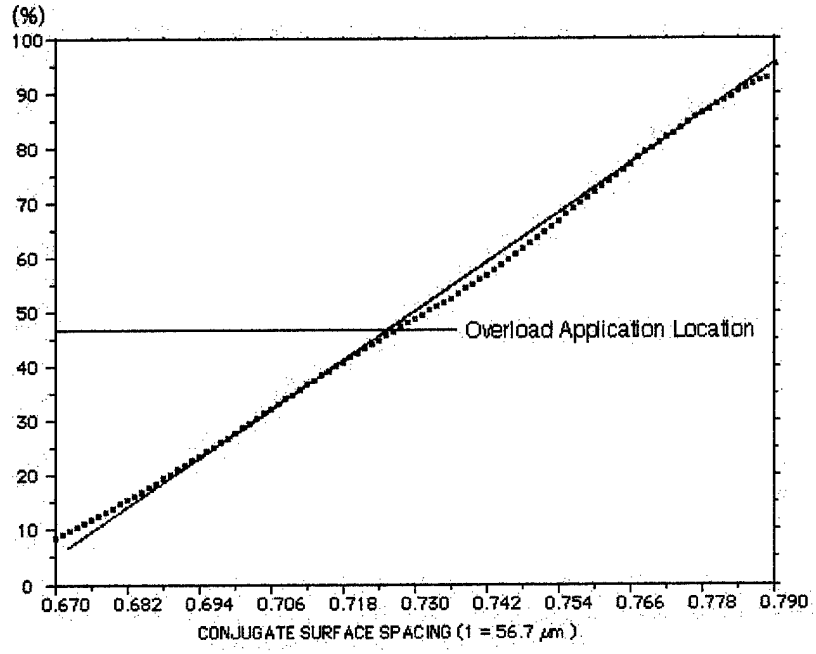

Figure AII-33. Increase in fractured area with increased spacing of the conjugate topographs.

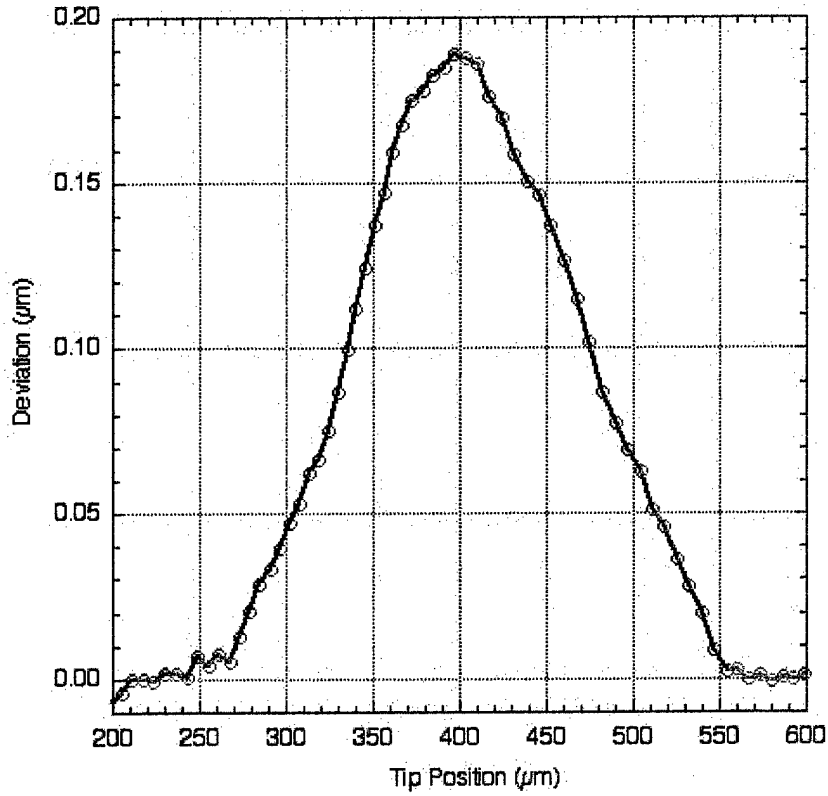

Figure AII-34. Deformation profile of the crack front in the vicinity of 37.5 MPa√m overload in the base fatigue loading of R=0.50 and 20 Hz.

IN100-alloy, R=0.50, freq=20 Hz, baseline K_{max}=30.0 MPa√m, overload Kmax=45.0 MPa√m (1.375 times the baseline stress intensity)

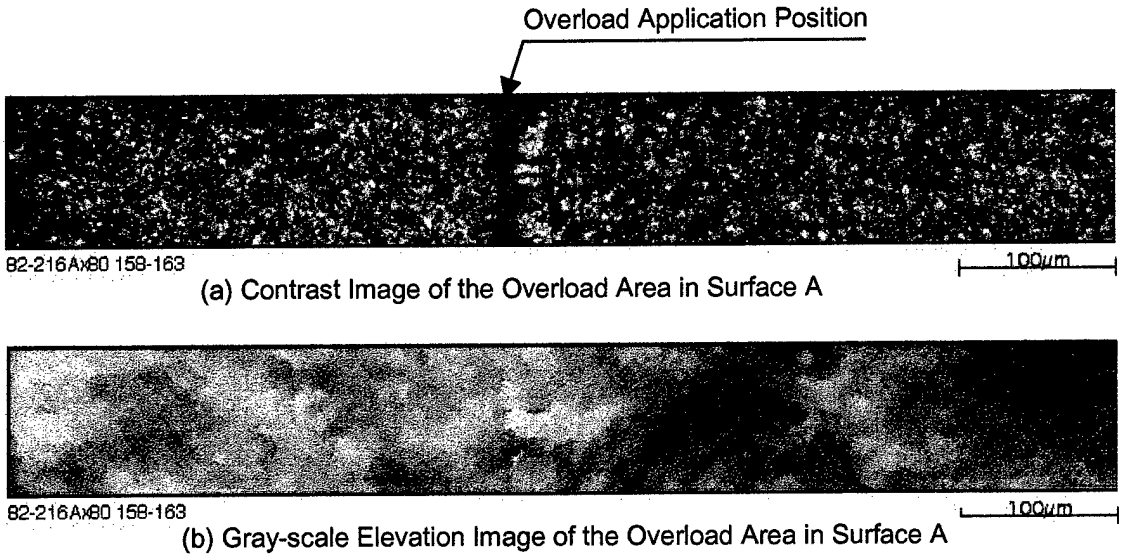

Figure AII-35. Contrast and gray-scale elevation images of single 45.0 MPa√m overload in R=0.50 and freq=20 Hz baseline fatigue region

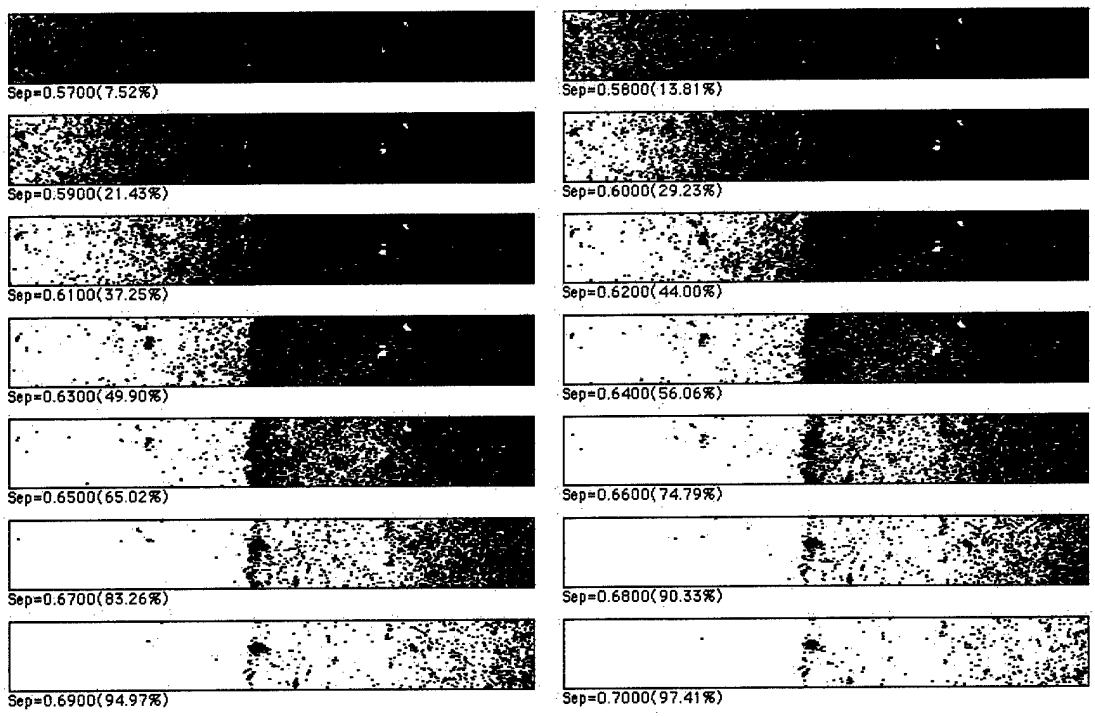

Figure AII-36. Fractured area projection plots (FAPPs) indicating the progression of the crack front.

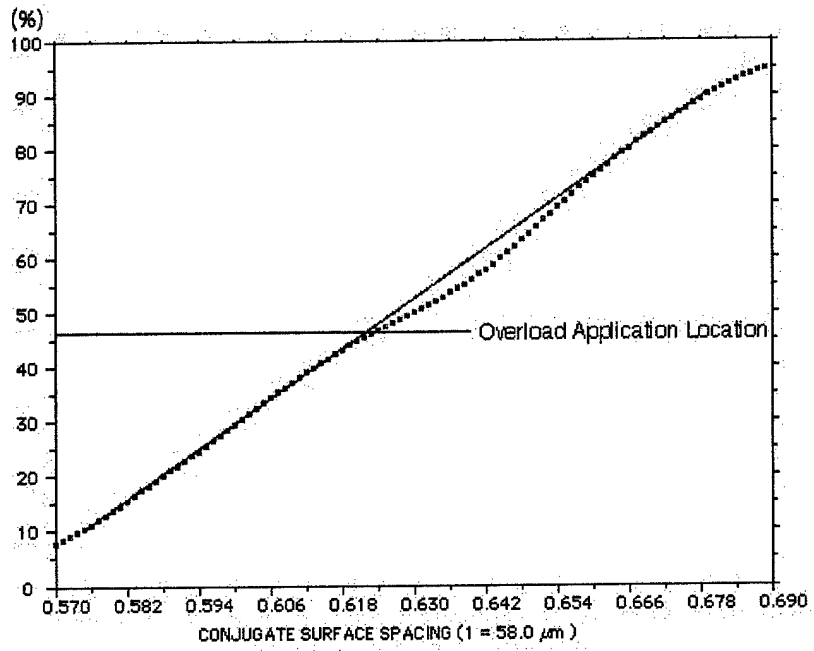

Figure AII-.37. Increase in fractured area with increased spacing of the conjugate topographs.

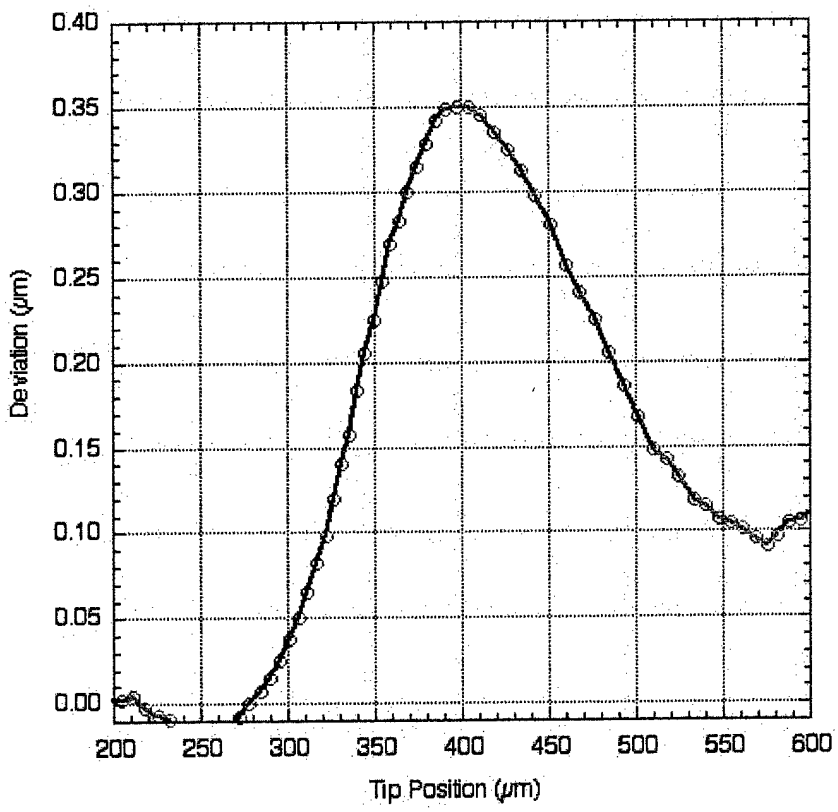

Figure AII-38. Deformation profile of the crack front in the vicinity of 45.0 MPa√m overload in the base fatigue loading of R=0.50 and 20 Hz.

IN100-alloy, R=0.50, freq=20 Hz, baseline K_{max}=30.0 MPa√m, overload Kmax=52.5 MPa√m (1.75 times the baseline stress intensity)

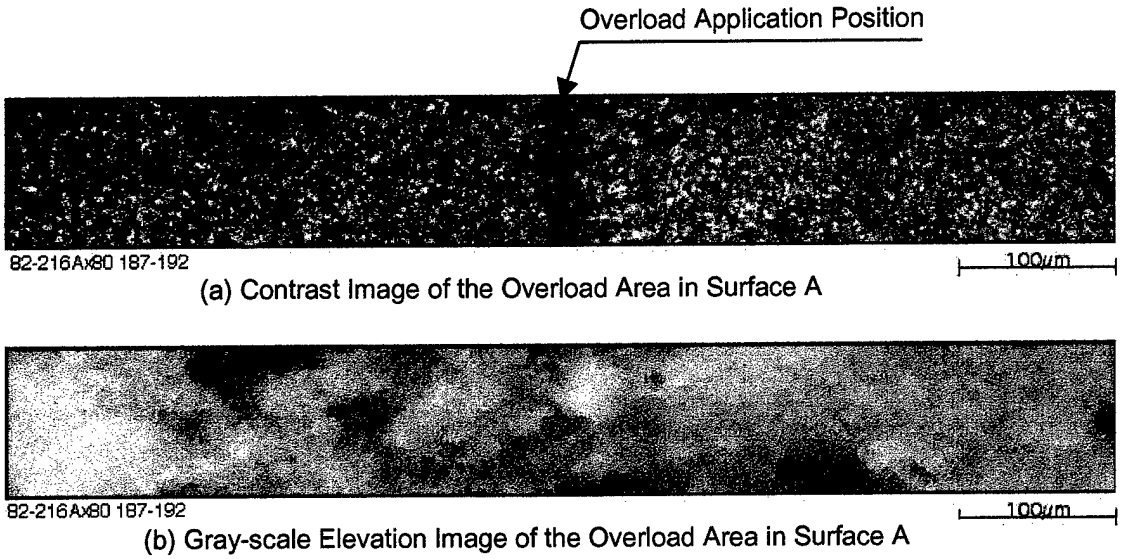

Figure AII-39. Contrast and gray-scale elevation images of single 52.5 MPa √m overload in R=0.50 and freq=20 Hz baseline fatigue region.

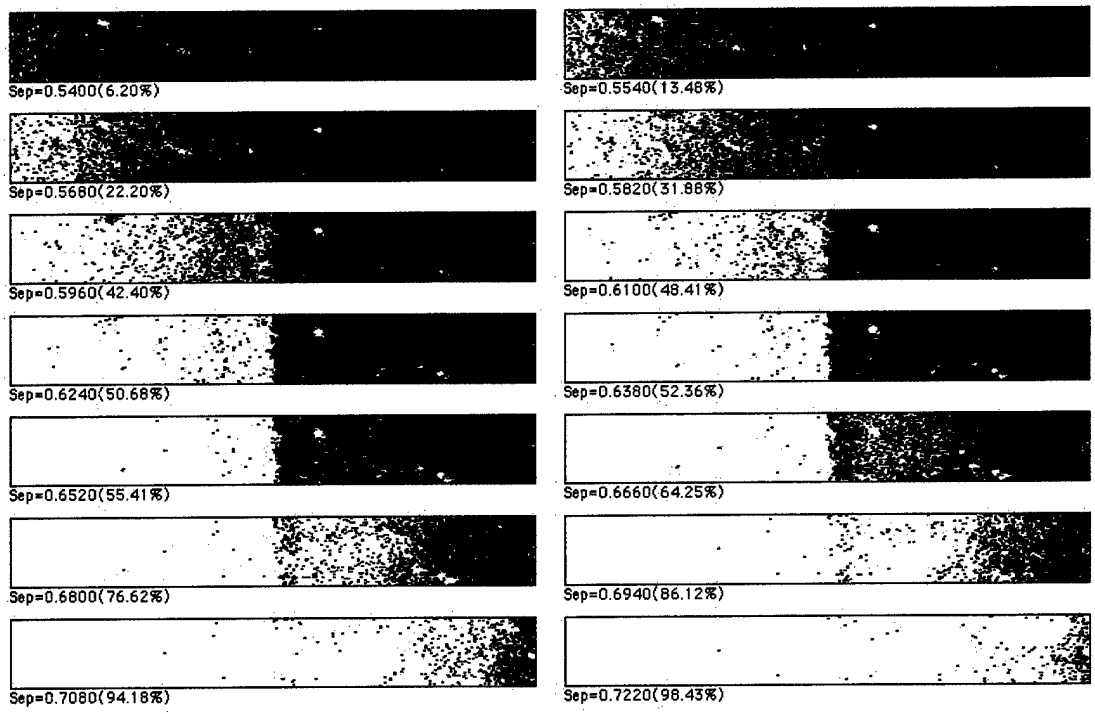

Figure AII-40. Fractured area projection plots (FAPPs) indicating the progression of the crack front.

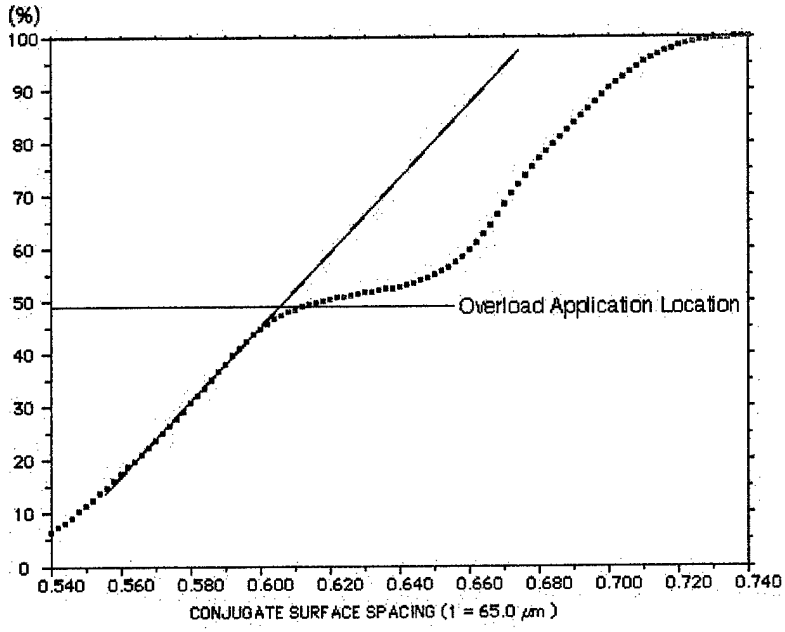

Figure AII-41. Increase in fractured area with increased spacing of the conjugate topographs.

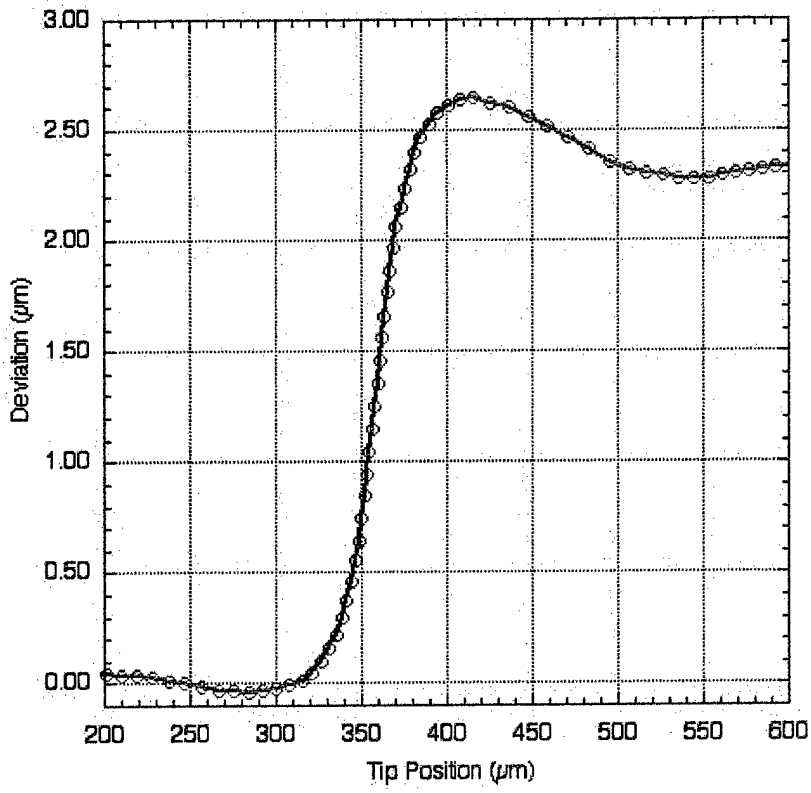

Figure AII-42. Deformation profile of the crack front in the vicinity of 52.5 MPa√m overload in the base fatigue loading of R=0.50 and 20 Hz.

IN100-alloy, R=0.50, freq=0.1667 Hz, baseline K_{max}=30.0 MPa√m, overload Kmax=37.5 MPa√m (1.25 times the baseline stress intensity)

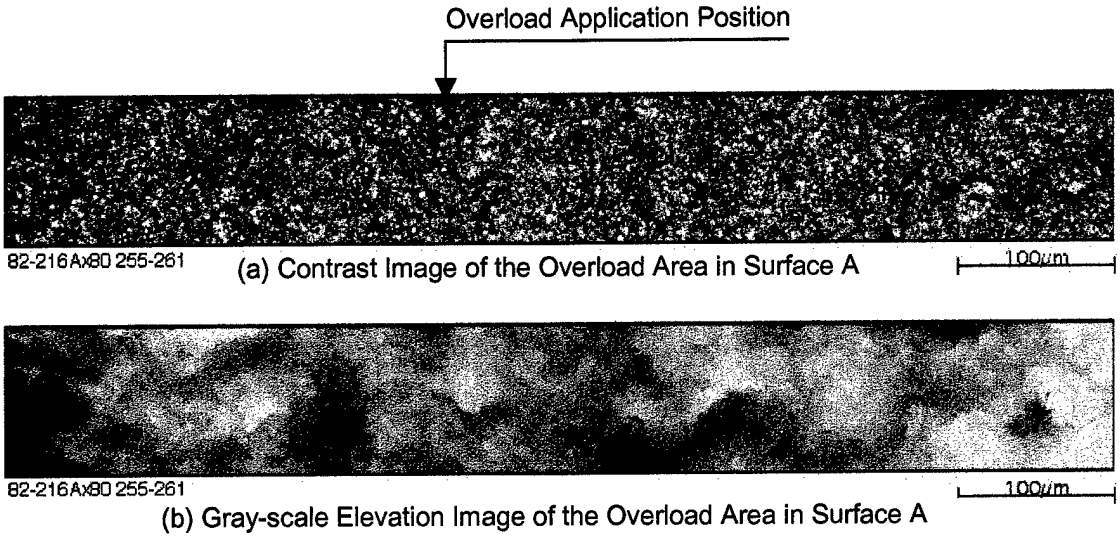

(a) Contrast Image of the Overload Area in Surface A

(b) Gray-scale Elevation Image of the Overload Area in Surface A

Figure AII-43. Contrast and gray-scale elevation images of single 37.5 MPa√m overload in R=0.50 and freq=0.1667 Hz baseline fatigue region.

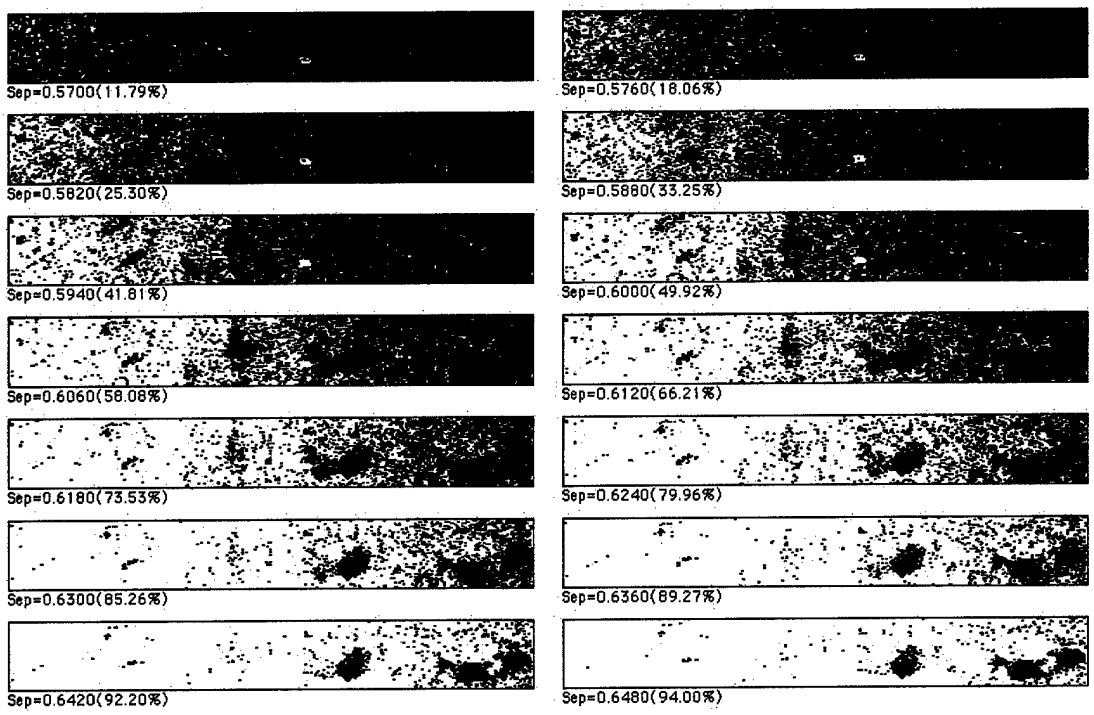

Figure AII-44. Fractured area projection plots (FAPPs) indicating the progression of the crack front.

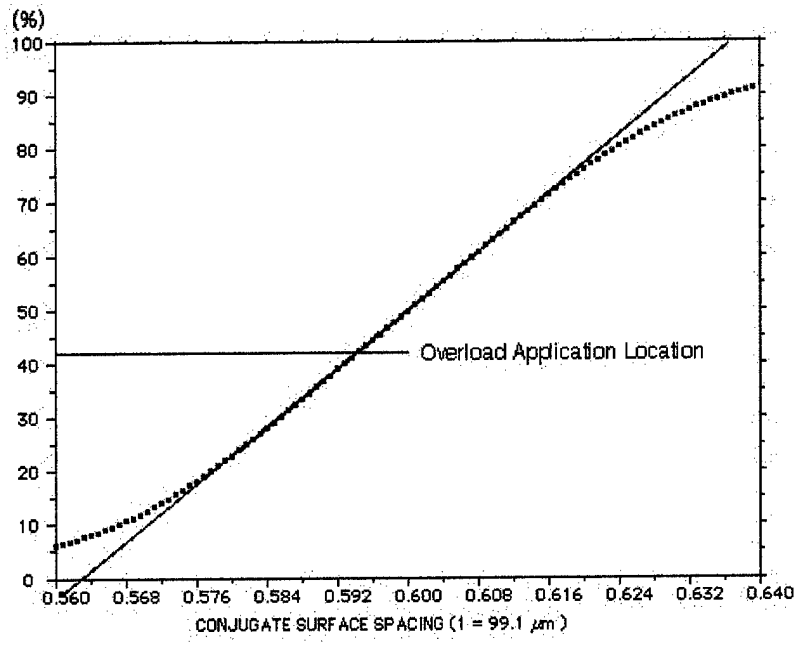

Figure AII-45. Increase in fractured area with increased spacing of the conjugate topograph.

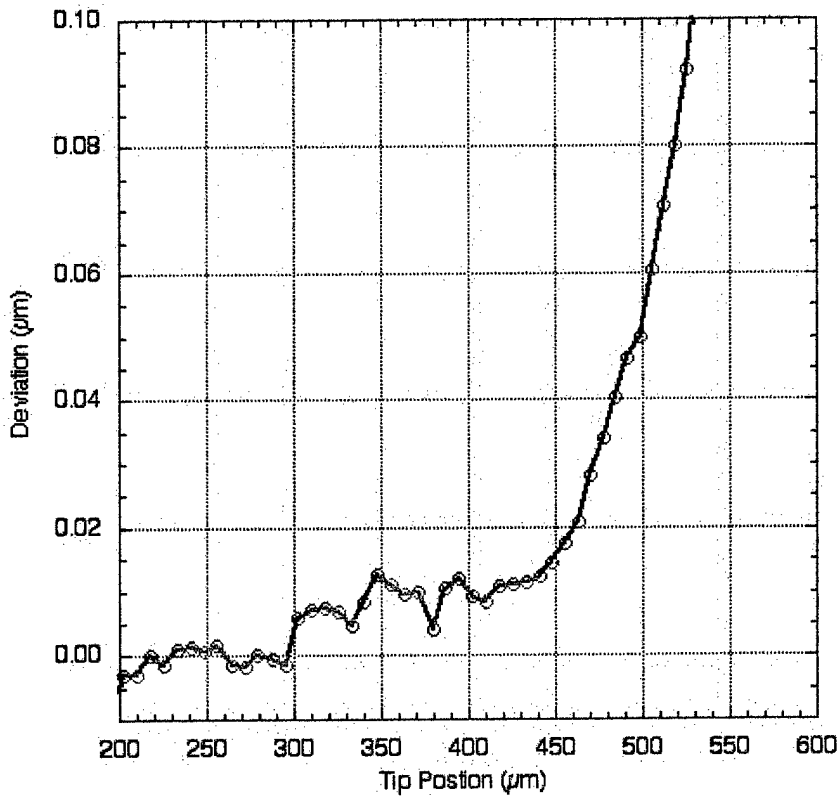

Figure AII-46. Deformation profile of the crack front in the vicinity of 37.5 MPa√m overload in the base fatigue loading of R=0.50 and 0.1667 Hz.

IN100-alloy, R=0.50, freq=0.1667 Hz, baseline K_{max}=30.0 MPa√m, overload Kmax=45.0 MPa√m (1.375 times the baseline stress intensity)

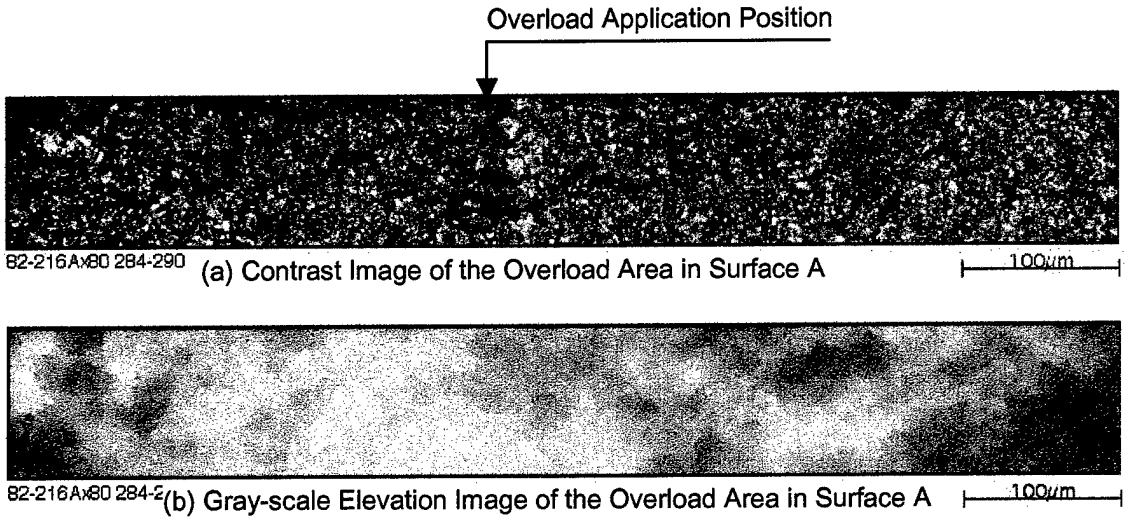

Figure AII-47. Contrast and gray-scale elevation images of single 45.0 MPa√m overload in R=0.50 and freq=0.1667 Hz baseline fatigue region.

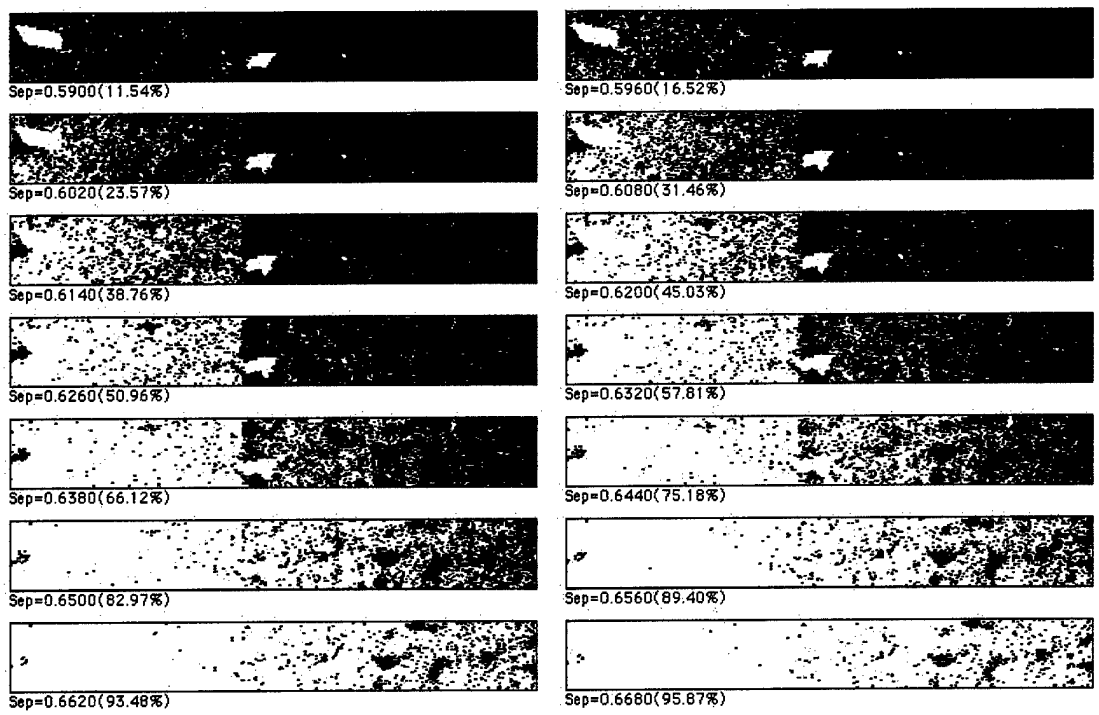

Figure AII-48. Fractured area projection plots (FAPPs) indicating the progression of the crack front.

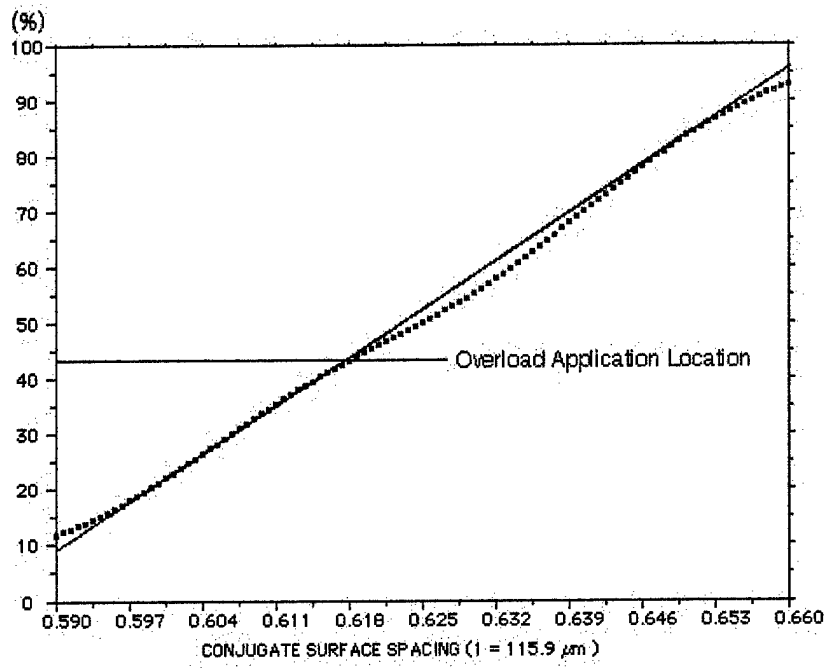

Figure AII-49. Increase in fractured area with increased spacing of the conjugate topographs.

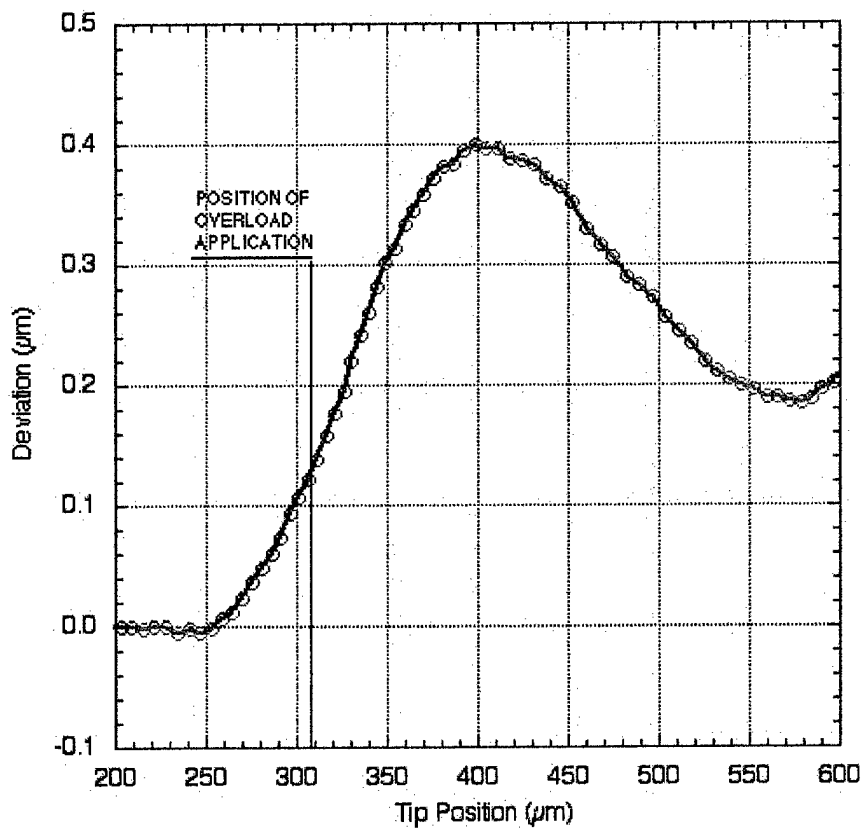

Figure AII-50. Deformation profiles of the crack front in the vicinity of 45.0 MPa√m overload in the baseline fatigue loading of R=0.50 and 0.1667 Hz.

IN100-alloy, R=0.50, freq=0.1667 Hz, baseline K_{max}=30.0 MPa√m, overload Kmax=52.5 MPa√m (1.75 times the baseline stress intensity)

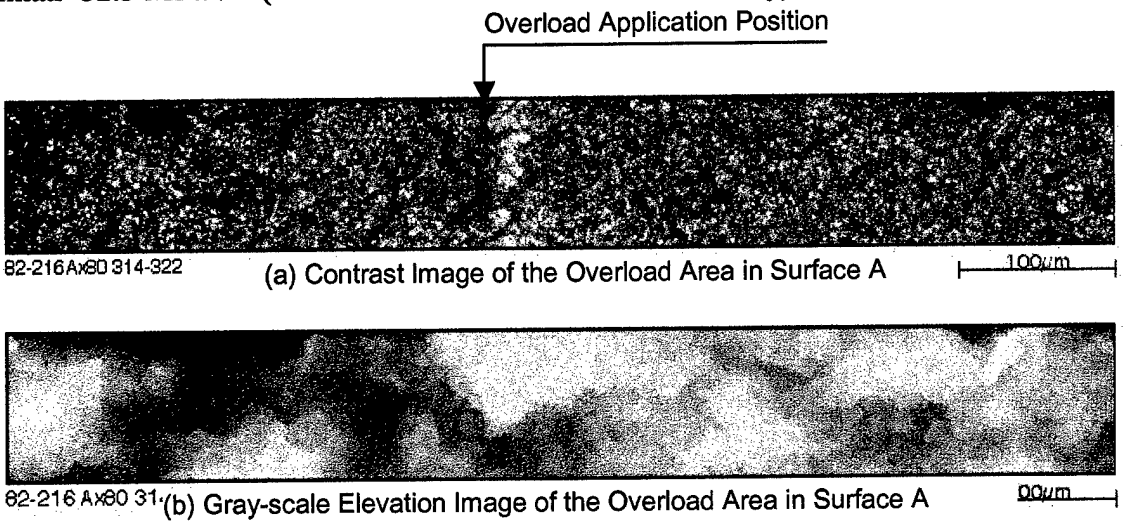

Figure AII-51. Contrast and gray-scale elevation images of single 52.5 MPa√m overload in R=0.50 and freq=0.1667 Hz baseline fatigue region.

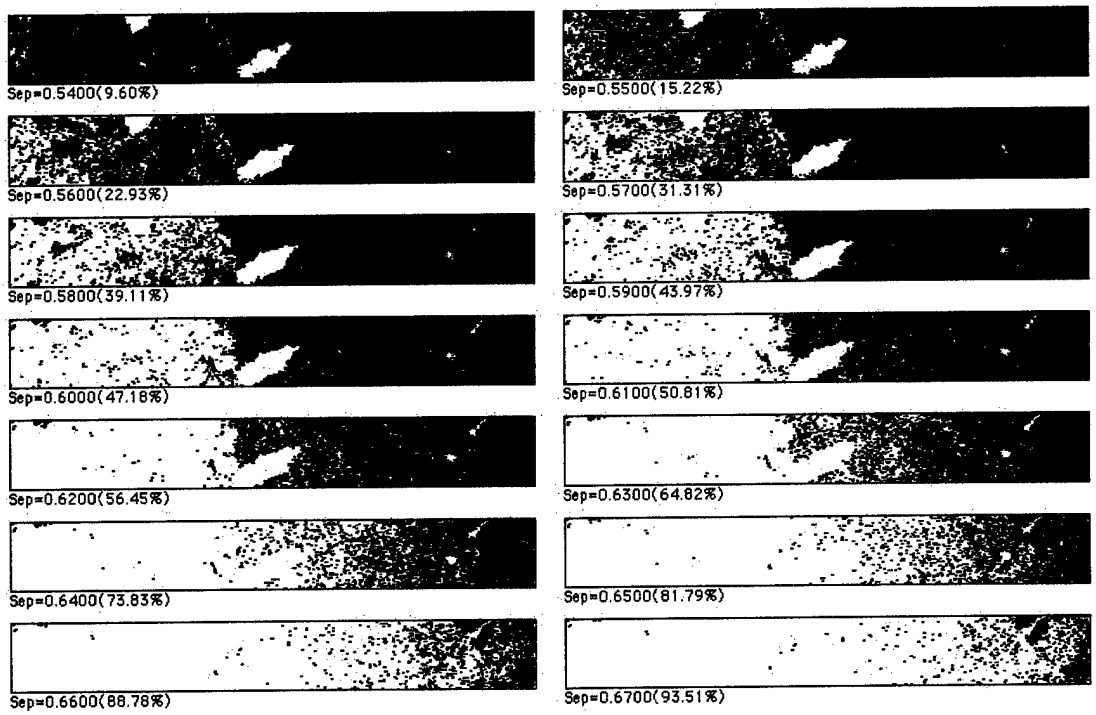

Figure AII 52. Fractured area projection plots (FAPPs) indicating the progression of the crack front.

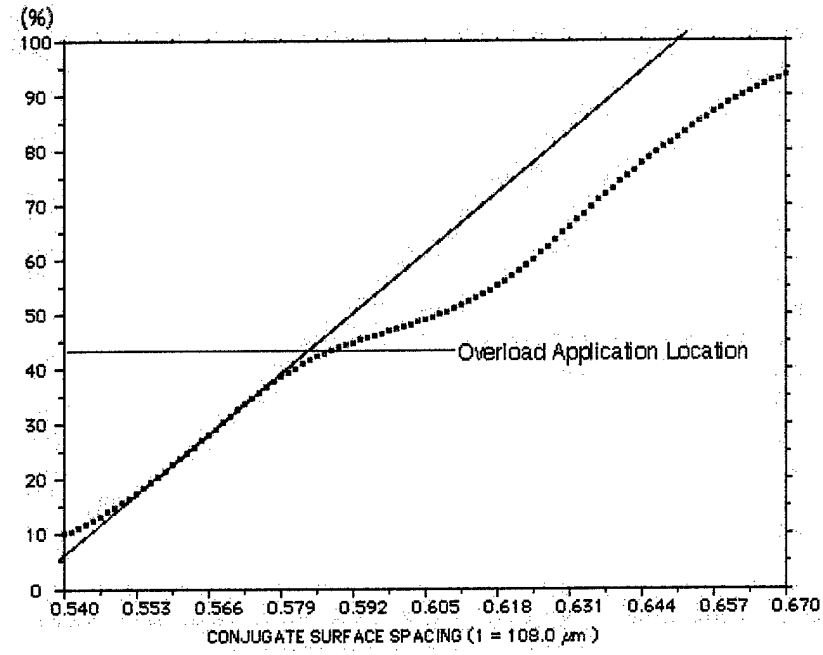

Figure AII 53. Increase in fractured area with increased spacing of the conjugate topographs.

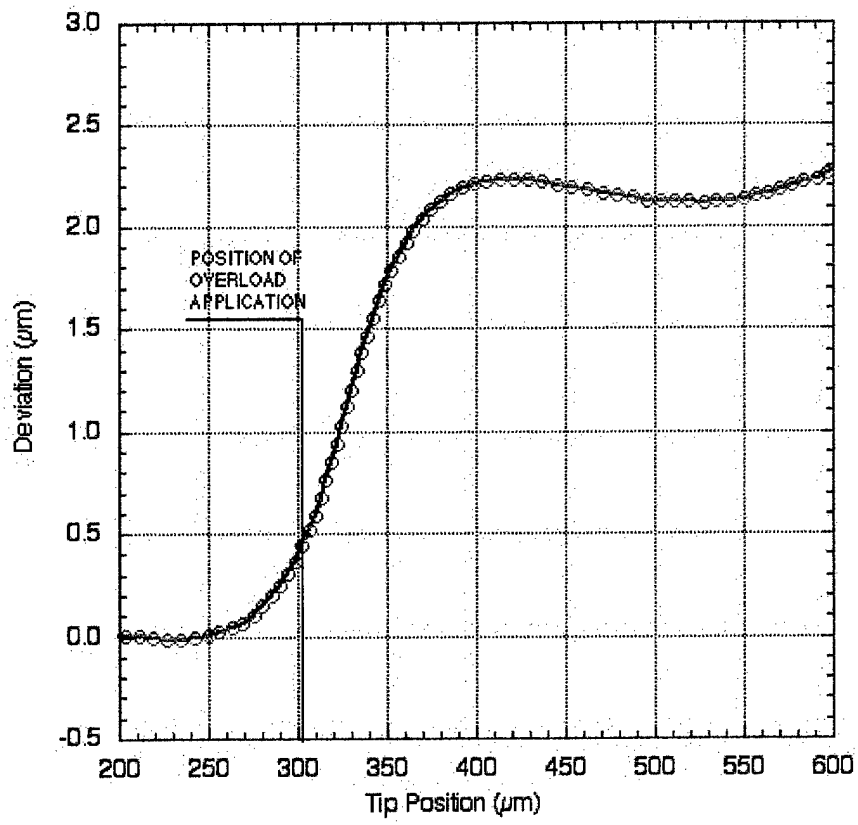

Figure AII 54. Deformation profiles of the crack front in the vicinity of 52.5 MPa√m overload in the baseline fatigue loading of R=0.50 and 0.1667 Hz.

Appendix III: FRACTOGRAPHIC EXAMINATION OF HIGH-CYCLE FATIGUE SPECIMENS

SUMMARY

An advanced analysis technique [Ref. AIII-1,2] was applied to fracture surfaces of high-cycle-fatigue specimens to determine if the stress ratio (R) could be deduced from the topography. The fracture surface topographies of titanium alloy specimens tested under high frequency cyclic loads at various stress ratios were characterized using confocal-optics scanning laser microscopy, and a fast Fourier transform analysis was applied to the data. The average elevation power spectrum density (EPSD) distribution curve was calculated as a function of crack position and ΔK. The surface roughness parameter, $(\text{EPSD})^{1/2}$, defined a crack initiation region, a relatively smooth region, and a final failure region. However, trends between roughness, ΔK, and R were ambiguous and require further analysis and interpretation.

SPECIMENS

Dr. Theodore Nicholas of the Air Force Research Laboratory provided four Ti-6Al-4V round-bar specimens from a series tested at different R-values by Morrissey, et al [Ref. AIII-3]. Specimen dimensions and test conditions are summarized in table AIII-1. Test procedures and material characteristics are described in detail in the Morrissey paper [Ref. AIII 3].

TABLE AIII-1. SPECIMEN GEOMETRY AND FATIGUE LOADING CONDITIONS

Specimen No.	Geometry	Diameter (mm)	Maximum Stress (MPa)	Stress Ratio
1	Dogbone with Button Head	3.8	880	0.75
2	Dogbone with Button Head	3.8	620	0.50
3	Dogbone with Button Head	3.8	700	0.10
4	Hourglass	5.5	525	-1.0

TOPOGRAPHY CHARACTERIZATION

Figure AIII-1 shows the crack initiation sites were close to the exterior surface and the cracks maintained a thumbnail-shaped front as they propagated from the initiation area to the specimen interior. We selected for examination a series of small areas (140.3 μm in the crack growth direction by 186.0 μm in the orthogonal direction) along a line from the crack initiation area to the interior of the specimen in the crack growth direction. We

characterized the topographies of these areas using a confocal-optics scanning laser microscope.

Figure AIII-2 shows examples of contrast and elevation images constructed from digital data files at three locations on the specimen tested at R = 0.1. The number of data points in each area was 600 (in the crack growth direction) by 800 (in the orthogonal direction), resulting in a data spacing of 0.233μm in both directions.

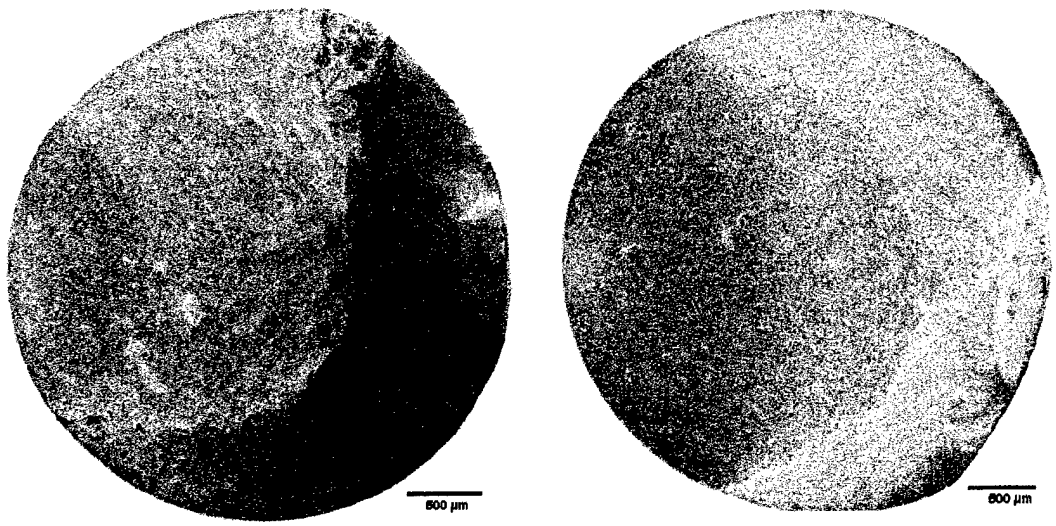

Figure AIII-1 Macro SEM photographs of four tensile fatigue specimens.

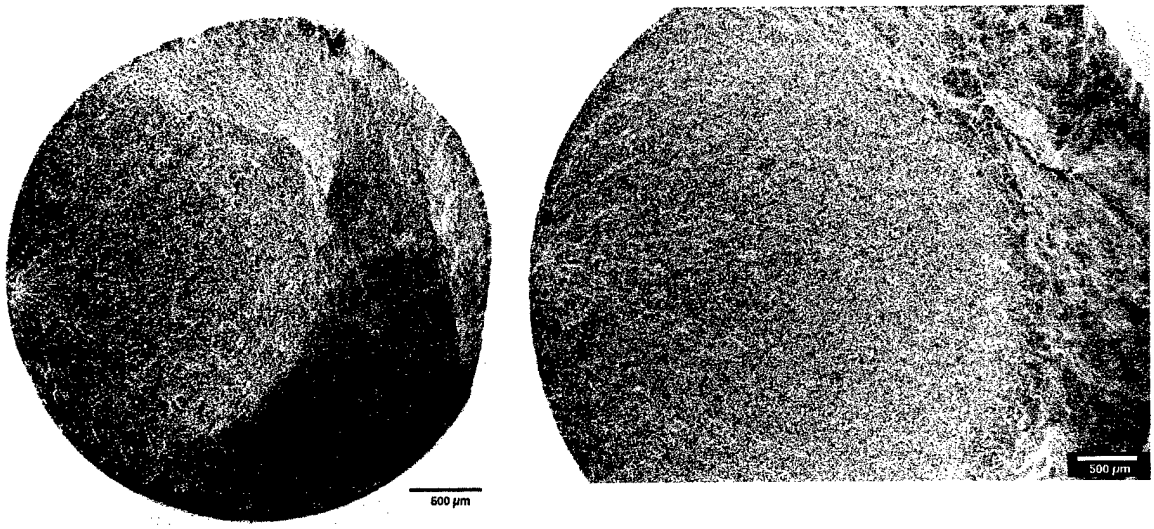

Figure AIII-1. Macro SEM photographs of four tensile fatigue specimens. (Concluded).

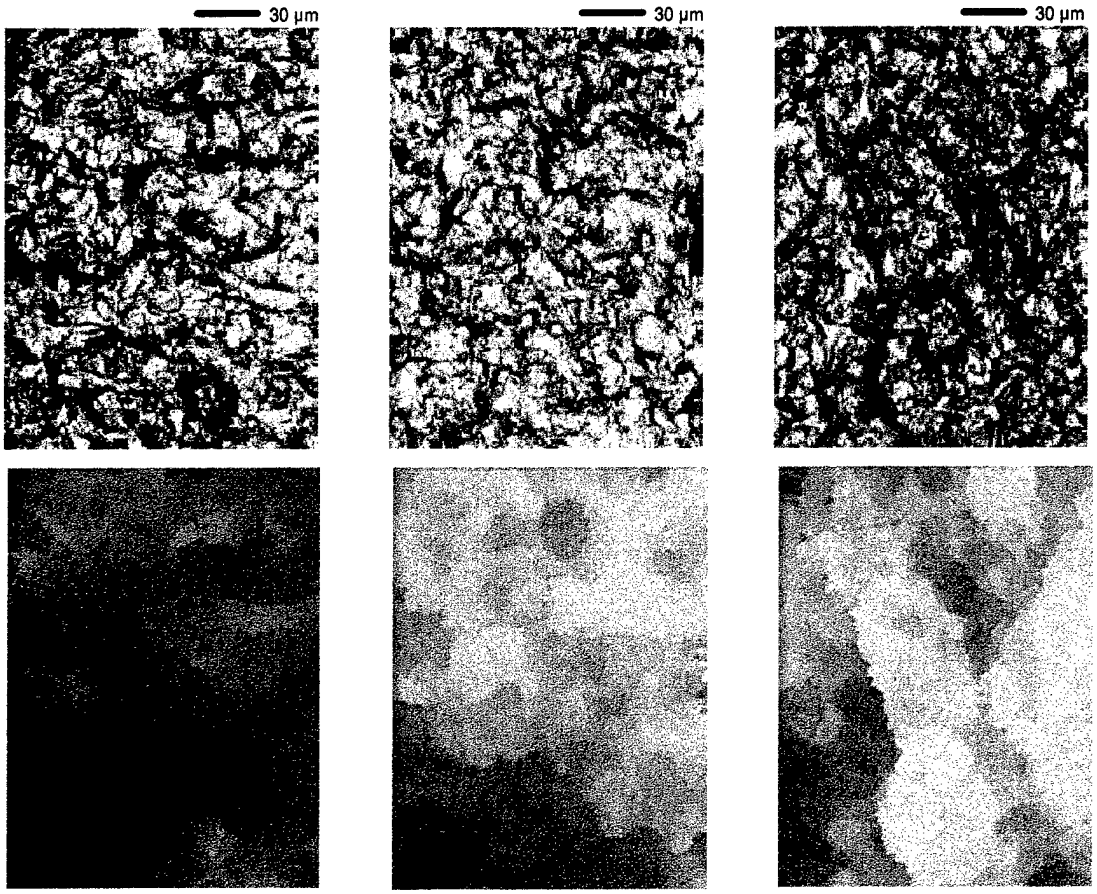

Figure AIII-2. Examples of contrast and gray-scale elevation images at different locations from the exterior surface of the specimen. In the elevation images white areas are high in elevation and dark areas low. (Test condition R=0.1)

FAST FOURIER ANALYSIS

A fast Fourier transform was applied to each line of topographic data (600 data points) in the crack propagation direction, and the elevation power spectrum density distribution was calculated. To eliminate local microstructural contributions to the topographies, and thereby emphasize the topography resulting from the deformation that occurred at the crack tip, the average value of the elevation power spectrum density was computed wavelength-by-wavelength over the 800 lines.

Figure AIII-3 shows the result for the specimen tested under the condition of R = 0.1. The curves are parallel and displaced from each other in the vertical direction. Furthermore, the curves are in general convex between wavelengths of from 0.5 to 10 microns with the convexity centered at a wavelength of about 2µm. The convexity could result from topography modification due to impingement of the conjugate surfaces during cyclic loading. The EPSD curves of the other three specimens showed a similar bowing,

although the degree of bowing differed slightly for different R-values. Based on these observations, we chose the EPSD at the 2μm wavelength to represent the surface topography.

The EPSD value at the 2μm wavelength was recorded for each curve of each specimen, and $(EPSD)^{1/2}$ values were plotted as a function of position on the fracture surface. (We took the square root of the EPSD value as the measure of surface roughness, based on correlations observed in previous work [Ref. AIII-4].

The results are summarized in Figure AIII-4. The curves define three regions: (1) a rough, irregular region near the exterior surface of the specimen (crack initiation area), (2) a linear smoother region in the middle, and (3) a second rough region toward the final rupture of the specimen. Furthermore, the curves differentiate the fracture surfaces produced under different loading conditions. We sought physical confirmation of this behavior through microscopic examination of the fracture surfaces.

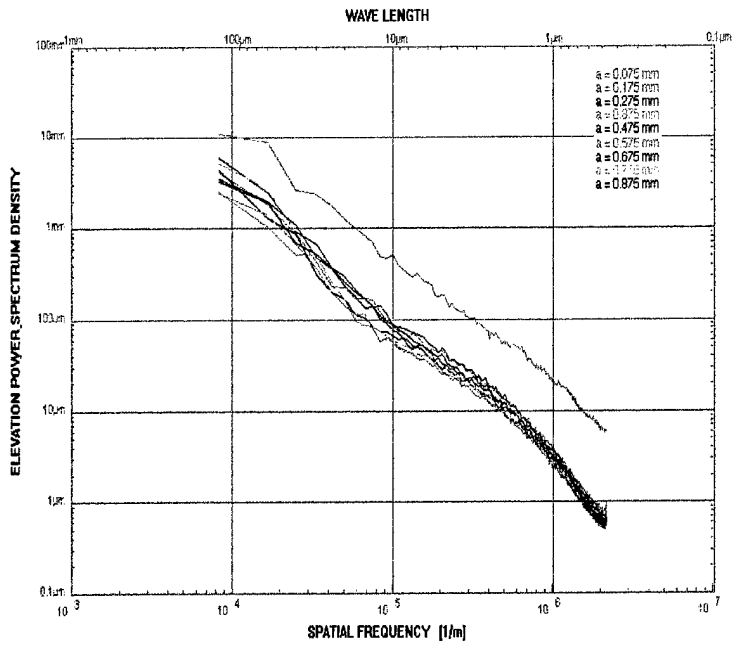

Figure AIII-3. EPSD curves for the first nine areas from the exterior surface for R=0.10 test.

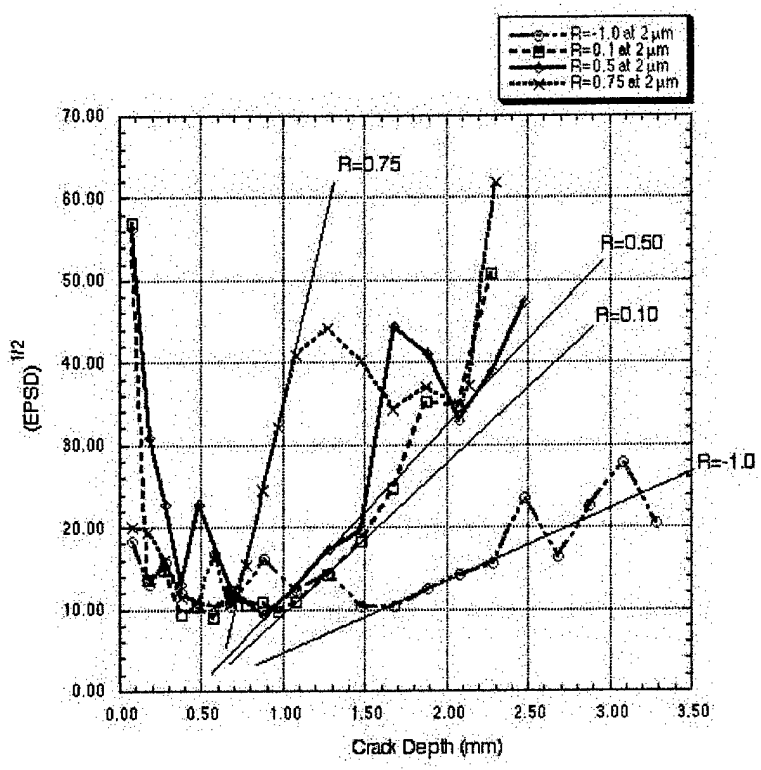

Figure AIII-4. $(EPSD)^{1/2}$ as a function of crack depth for specimens tested at different R-values.

FRACTURE SURFACE OBSERVATIONS

Examination of the fracture surfaces of the four specimens produced under different R-values led to common physically based reasons for the three different regions of the $(EPSD)^{1/2}$ versus crack depth curves. The first irregular region resulted from microcrack nucleation at sites above and below the eventual macrocrack plane. As these microcracks grew, they merged with one another to form a macrocrack on a nominal, more well-defined failure surface. In Region II the macrocrack extended under cyclic loading, producing a relatively smooth fracture surface on which fatigue striations could be observed.

The failure surface became rougher as the crack front approached the specimen boundaries. The irregular Region III may result from a change in fracture mode, in which microcracking or void formation occurred ahead of the crack front.

STRESS INTENSITY CONSIDERATIONS

Because the maximum applied stress level differed from specimen to specimen, as shown in Table AIII-1 the stress intensity associated with the same crack depth differs from specimen to specimen. Thus, we converted the data in Figure AIII-4 to stress intensity. The stress intensity factor (K) and stress intensity range (ΔK) were computed using the K-formula developed by Forman and Shivakumar [Ref. AIII-5]. The $(EPSD)^{1/2}$ values

plotted against ΔK are shown in Figure AIII-5. The slope distinguishes three regions, as described above.

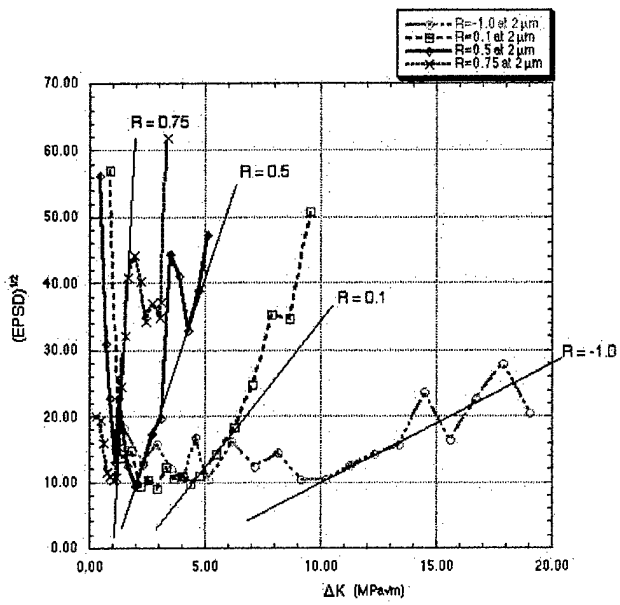

Figure AIII-5. $(EPSD)^{1/2}$ as a function of stress intensity range (ΔK) for specimens tested at different R-values.

Figure AIII-5 shows several interesting characteristics. First, a common lower bound in $(EPSD)^{1/2}$ exists for the loading conditions examined. The generality of this observation is not clear, and the level of the roughness, an $(EPSD)^{1/2}$ value of 10, has no intrinsic basis at the moment. Moreover, the observation, that at shorter crack lengths EPSD remains constant as ΔK increases at shorter crack lengths, requires explanation.

Second, two competing surface roughness influences are suggested. At smaller ΔK, crack closure may flatten the surface; at larger ΔK, the high stress intensity may overcome closure and produce higher roughness. The transition in roughness likely depends on stress ratio R. Figure AIII-6 shows the relationship between R and the value of ΔK where surface roughness starts to increase, and Figure AIII-7 shows the slope of the increase as a function of ΔK. The crack closure effect dominates below a stress ratio of 0.5 to .075, whereas the stress intensity effect prevails above 0.75.

Over a short portion of the fracture surface the roughness increases linearly with stress intensity. It is tempting to focus on this small, well-behaved area and say it is reflective of how R-values influence the surface roughness. If so, the variation of roughness (as characterized by $(EPSD)^{1/2}$ with ΔK, depends on R in a rational way, as shown in Figure III-6. However, a rougher surface with increasing R goes against intuition.

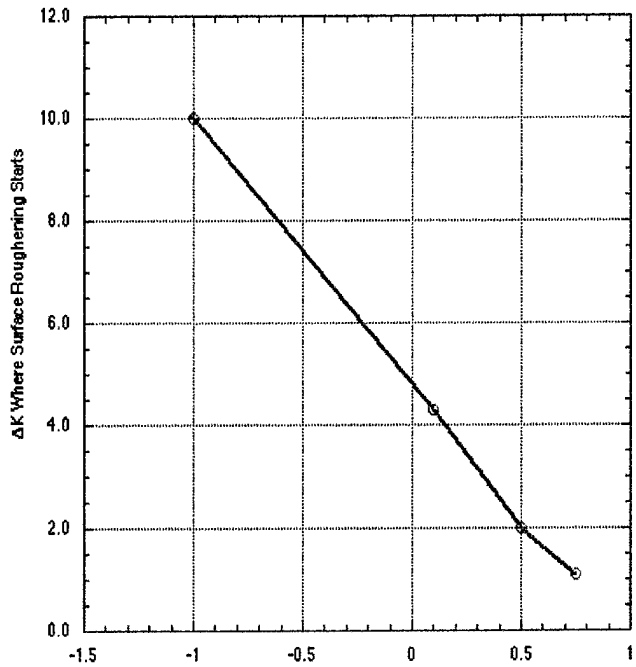

Figure AIII-6. Stress intensity range (ΔK) at which the $(EPSD)^{1/2}$ value started to increase linearly for different stress ratios.

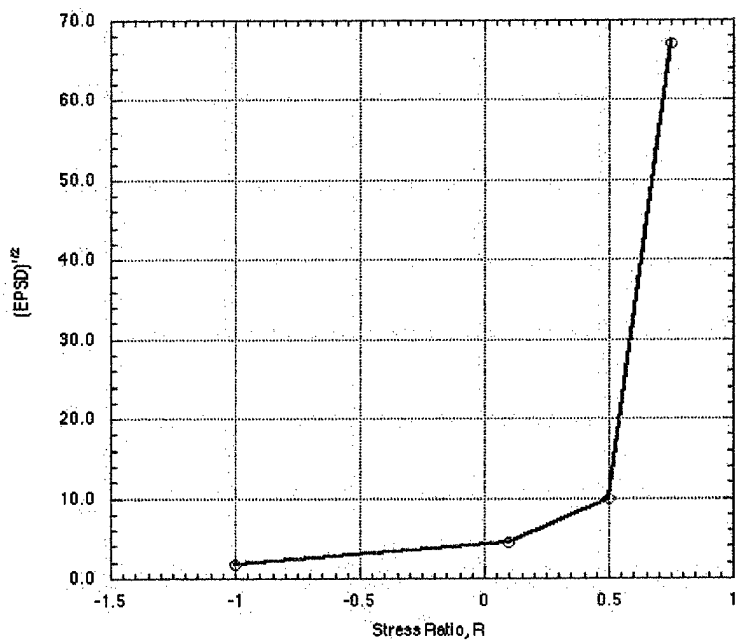

Figure AIII-7. Slope of the curves of $(EPSD)^{1/2}$ versus δK as a function of R.

CONCLUSIONS

Trends between roughness and stress intensity were identified, but a unified and logical explanation for the overall behavior is lacking. Additional measurements, alternative analyses, and new perspectives are required to extract information on the effects of R on fracture surface topography.

APPENDICES REFERENCES

AIII-1 T. Kobayashi, D.A. Shockey, C. G. Schmidt and R. W. Klopp, "Assessment of Fatigue Load Spectrum from Fracture Surface Topography," Int. J. Fatigue, **19**, Supp. No. 1, pp. S237-S244 (1997).

AIII-2 T. Kobayashi and D.A. Shockey, "The Relationship Between Fracture Surface Roughness and Fatigue Load Parameters," Int. J. Fatigue, **23**, pp. S135-S142 (2001).

AIII-3 R.J. Morrissey, D.L. McDowell, and T. Nicholas, "Frequency and Stress Ratio Effects in High Cycle Fatigue of Ti-6Al-4V," Int. J. Fatigue, **21**, pp. 679-685 (1999).

AIII-4 D.A. Shockey, T. Kobayashi, N. Saito, J-M Aubry, and A. Grünbaum, "Fractographic Analysis of High-Cycle Fatigue in Aircraft Engines," Final Technical Report to the Air Force Office of Scientific Research on Contract F49620-98-C-0041 (January 2000).

AIII-5 F.G. Forman and V. Shivakumar, "Growth Behavior of Surface Cracks in the Circumferential Plane of Solid and Hollow Cylinders," Fracture Mechanics, **17**, ASTM STP 905, pp. 59-74 (1986).